Internal injection of electrons into a plasma wake-field on a plasma cathode at FLASHForward

Dissertation

zur Erlangung des Doktorgrades

an der Fakultät für Mathematik, Informatik und Naturwissenschaften

der University of Hamburg

im Fachbereich

Physik

vorgelegt von

Bridget Jean Sheeran

Hamburg

2023

Gutachter/innen der Dissertation:	Dr. Jens Osterhoff Prof. Dr. Brian Foster
Zusammensetzung der Prüfungskommission:	Prof. Daniela Pfannkuche Dr. Jens Osterhoff Prof. Dr. Brian Foster Dr. Andreas R. Maier Prof. Gudrid Moortgat-Pick
Vorsitzende/r der Prüfungskommission:	Prof. Daniela Pfannkuche
Datum der Disputation:	03.03.2023
Vorsitzender des Fach-Promotionsausschusses PHYSIK:	Prof. Dr. Günter H. W. Sigl
Leiter des Fachbereichs PHYSIK:	Prof. Dr. Wolfgang J. Parak
Dekan der Fakultät MIN:	Prof. Dr.-Ing. Norbert Ritter

Declaration on oath

I hereby declare in lieu of oath that I have written this dissertation myself and that I have not used any auxiliary materials or sources other than those indicated.

Mannheim, July 16, 2023

Bridget Jean Sheeran

Abstract

The expanding footprint of conventional accelerators in recent years has motivated a similar expansion of research into novel accelerator technologies. Plasma-based accelerators offer the potential of a compact accelerator with gradients exceeding the $\mathrm{GV\,m^{-1}}$ mark and to therefore an increased availability of high-energy charged-particle beams. However, a significant amount of research and development is still required in order to bring the technology into a state with the high degree of reliability required from modern accelerators. Once such aspect is the production, trapping and acceleration of a witness bunch within these intense fields, which this thesis aims to address. While many techniques exist and are in various states of development, this thesis centres on just one. Here the steps required to carry out the first stable demonstration of Laser Triggered Density Down-ramp injection are outlined. These steps include a feasibility study exploring the experimental parameter space and the set-up of the experiment, followed by the experimental results demonstrating the stability and control offered by the methods used.

Zusammenfassung

Der wachsende Platzbedarf konventioneller Beschleuniger hat in den letzten Jahren zu einer Ausweitung der Forschung an neuartigen Beschleunigertechnologien geführt. Plasmabasierte Beschleuniger bieten das Potenzial eines kompakten Beschleunigers mit Gradienten, die die $\mathrm{GV\,m^{-1}}$-Marke überschreiten, und zur Erweiterung der Verfügbarkeit hochenergetischer Strahlen geladener Teilchen. Es sind jedoch noch erhebliche Forschungs- und Entwicklungsarbeiten erforderlich, um die Technologie in ein betriebsbereites System zu überführen. Ein solcher Aspekt ist die Erzeugung, das Einfangen und die Beschleunigung eines Teilchenpakets in diesen intensiven Feldern, mit dem sich diese Arbeit befasst. Während viele Techniken existieren, die sich in verschiedenen Entwicklungsstadien befinden, konzentriert sich diese Arbeit auf eine einzige. In dieser Arbeit werden die erforderlichen Schritte zur Durchführung der ersten stabilen Demonstration der laserausgelösten Density-Down-Ramp Injektion beschrieben. Diese Schritte umfassen eine Machbarkeitsstudie, in der der Raum der Versuchsparameter und der Versuchsaufbau untersucht werden, gefolgt von den Versuchsergebnissen, die die Stabilität und die Kontrolle durch die verwendeten Methoden belegen.

Contents

1 Introduction

1.1 Accelerators as a means of discovery

Particle accelerators have established themselves as a key tool in the never-ending pursuit of researchers to understand the universe in which we find ourselves. While our current model of particle physics does a remarkably good job of explaining many of our observations and has so far passed many of the tests thrown at it, there are many questions which are yet to be answered. Several Beyond the Standard Model (BSM) theories exist to explain these questions, however experimental signatures of their validity have, so far, not materialised [1]. Instead, much focus lies in precisely probing the Standard Model at its fringes, the areas where its predictions and reality differ just enough to find evidence of physics which it cannot explain.

The most recent example of this is the g-2 Muon experiment at Fermilab [2], where the magnetic moment of the muon was measured. A value, which has been seen to differ slightly from the value predicted from theory [3]. The magnetic moment of the muon is given by

$$\vec{\mu}_\ell = g_\ell \left(\frac{q}{2m_\ell} \right) \vec{s} \quad \text{where } g_\ell = 2\left(1 + a_\ell\right), \tag{1.1}$$

where $\ell = (e, \mu)$, q is the charge of the lepton, m_ℓ the lepton mass. In this experiment, the

anomalous magnetic moment of the muon, a_μ, was measured to a high degree of precision. A 4.2σ deviation from the predicted value was found, hinting at the physics which may lie beyond the Standard Model. Other experiments, such as the LHCb experiment at the Large Hadron Collider (LHC) at CERN, seek to study the asymmetries between matter and anti-matter. This asymmetry is also absent from the model, but is clear to the casual observer as our universe appears to be made entirely out of matter.

Probing the fundamentals of the universe is not the only role accelerators have. When undergoing acceleration, charged particles produce synchrotron radiation. For an electron with energy $\mathcal{E}$ in a circular accelerator with bending radius ρ, the power produce scales according to [4],

$$P_{\mathrm{SR}} = \frac{e^2}{6\pi\epsilon_0 m_e^4 c^7}\frac{\mathcal{E}^4}{\rho^2}. \tag{1.2}$$

This scaling provides a limiting factor to the construction of high-energy circular accelerators with low-mass particles. As the energy increases, the particle may enter a regime in which it loses more energy to synchrotron radiation than is feasible for the particle to regain on each pass of the accelerating structures.

Nevertheless, this light output at circular electron accelerators rapidly increased the development of the field of Photon Science, which utilises this light in order to study the nature of matter [5] [6]. Applications include crystallography to determine the 3D structure of proteins [7] and absorption spectroscopy to study the chemistry of a sample [8]. This field has developed from its earlier days of parasitic operation at synchrotrons, to the construction of insertion devices such as wigglers and undulators which are arrays of magnets designed to induce the production of synchrotron light from a passing electron beam [9]. Today many facilities operate their accelerators for the exclusive production of synchrotron light. One such example is the PETRA[1] storage ring at DESY which formerly operated as an electron-positron collider, before being used as a pre-accelerator for HERA[2] as PETRA-II. After HERA operations ceased, it was converted into PETRA-III [10], a dedicated X-ray light source with 23 beam-lines available for its users.

The latest generation of these light sources are Free Electron Lasers (FELs), which produce brilliant light that is orders of magnitude brighter than the previous generation of light

[1] Positron-Elektron Tandem Ring Anlage
[2] Hadron Elektron Ring Anlage

sources [11] and provides shorter wavelengths than is possible for any conventional laser to produce. These machines are used to probe the structure of matter and have lead to many advances in fields such as medicine and chemistry. Many of these light sources have been used by researchers to study the structure, behaviour and response of the SARS-Cov-2 virus in order to bring about the end of the coronavirus pandemic [12]. A summary of research at CERN in 2020 has been collected [13] and updates from DESY were published [14].

1.2 Development of accelerator technology

All these experiments, whether collider or photon based require high-energy particle beams, thereby necessitating the use of accelerator technology to produce such high-energy beams. The earliest accelerators were cathode-ray tubes (CRT) developed in the 19th century, a technology which is still in use for medical and security applications today. Since then iterations and improvements have seen the technology continuously refined into the state of the art superconducting RF cavities used today. Some highlights from over a century of accelerator technology development can be seen in Table 1.1.

1.2.1 The push to higher and higher energies

Behind many of the advancements listed in Table 1.1, was a desire to reacher higher energies. This was motivated by either exploring new realms of physics in colliders, or to produce synchrotron light at shorter wavelengths. A feat which may be done by building a longer accelerator, by increasing the gradient at which the particles are accelerated or – more commonly – a combination of the two.

Currently FEL technology is only available at the scale of national laboratories, far beyond the reach of any university-scale laboratory both in terms of cost and space. Any researcher wishing to carry out experiments at an FEL must either base themselves at a national laboratory, or be prepared to travel to such a facility. Furthermore beam-time allocation at these FEL facilities is often in high demand and usually limited [30]. It is therefore crucial to continuously explore new methods and techniques which will be used to construct the next generation of accelerators. Gradients in the latest generation of X-Band RF accelerators are limited to about $100\,\mathrm{MV\,m^{-1}}$ [27]. Increasing this gradient by an order of magnitude or more would be a major milestone to reducing the cost and footprint of FELs and therefore increas-

1890s	Discovery of cathode rays and CRTs invented
1920s	Development of principles behind betatron acceleration by Wideröe [15]
1932	Cockcroft and Wolton design a novel accelerator to split lithium with 400 keV protons [16] (1951 Nobel Prize)
1932	Lawrence produces 1.25 keV protons using a cyclotron and splits the atom [17] (1939 Nobel Prize)
1940	First working betatron built by Kerst produces 2.3 MeV electrons [18]
1944	E. McMillan [19] and V. Veksler [20] independently discover the principle of phase stability, inventing the synchrotron
1952	First proton synchrotron, the 3 GeV Cosmotron, built at Brookhaven National lab [21]
1970s	The Tevatron at Fermilab opens up the TeV energy frontier with superconducting magnets [22]
1974	First super conducting RF cavity demonstrated [23]
1975	First accelerator built using superconducting RF cavities [24]
1992	Hadron Elektron Ring-Anlage (HERA) enters operation with 27.5 GeV electrons and 820 GeV protons [25]
2000	Niobium-based TESLA cavities developed with gradients of $\geq 15\,\mathrm{MV\,m^{-1}}$ [26]
2008	First beam operation in the Large Hadron Collider at CERN, the largest circular accelerator ever built with a design centre of mass energy of 13 TeV
2008	CLIC cavities demonstrating performance at $\geq 100\,\mathrm{MV\,m^{-1}}$ [27]

Table 1.1: Selected highlights from the development of accelerator technology from the 1890s until the modern day. Pre 1960s timeline adapted from [28]. Development of superconducting RF cavities adapted from [29]

ing their availability [31] to laboratories and universities with fewer resources.

1.3 Plasma-based accelerators

Plasma-based acceleration, first proposed in 1979 by Tajima and Dawson [32], replaces the RF cavity with a plasma. A plasma is a gas which is comprised of electrons and charged ions and is free from the breakdown effects are one limiting factor in the performance of cavity-based accelerators [33], while supporting fields that easily exceed the $\mathrm{GV\,m^{-1}}$ mark. The original paper proposes a linear plasma wave driven by an intense laser pulse which was extended in 1985 to include a charged particle beam as the driver [34]. In both cases the intense fields of the driver act upon the plasma electrons to drive the plasma wave [35]. Since then the field has developed from the linear wave model into a regime which is referred to as the bubble or blowout regime [36]. In this regime, the driving beam acts upon the plasma electrons to expel all the electrons in its path while the heavier ions remain (relatively) static. With the electric field of the ions is no longer shielded by the plasma electrons, the fields pull them

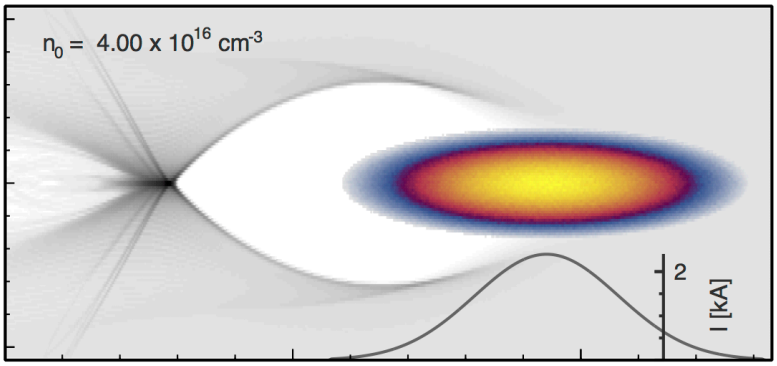

Figure 1.1: An illustration of a simulation of a plasma wake-field driven by an electron beam (right). The plasma electron density is depicted in grey. The high current electron beam expels electrons from the central axis. The heavier ions remain (relatively) static and their unshielded electrostatic fields divert the trajectories of the electrons back towards the central axis. This produces a cavity or bubble behind the driver.

back towards the central axis which results in a cavity devoid of electrons behind the driver beam. A simulation of the wake-field driven by a kA electron beam in shown in Figure 1.1

Research in plasma-based acceleration is typically classified according to the type of driver used. The laser driven scheme is referred to as *Laser Wake-Field Acceleration* (LWFA) and beam driven scheme is known as *Plasma Wake-Field Acceleration* (PWFA). In this work, the focus of attention will be on the latter scheme.

1.3.1 Development of PWFA

As with the development of conventional accelerators, the development of PWFA has continued since its inception in the 1980s. Several milestones from this process are highlighted in Table 1.2. The strong accelerating fields have been well demonstrated by a number of sources and most recently characterised by the authors of [37].

PWFAs are being actively studied at a number of laboratories around the world. The focus of this work will be on the FLASHForward[3] experiment based at DESY in Hamburg Germany, which is centred around a 1.25 GeV high-quality beam as its driver [38]. Other projects include FACET[4]-I and II at the Stanford linear accelerator (SLAC) in California [39] [40]. FACET-I used a 23 GeV 3 nC driver with goals including the demonstration of positron ac-

[3]Future ORientated wake-field Accelerator Research and Development at FLASH
[4]Facility for Advanced Accelerator Experimental Tests

1979-1985	Theory of plasma wake-field acceleration developed [32][34]
1988	First observation of wake-fields in a plasma [42]
2005	Demonstration of multi-GeV energy gain of electrons in a PWFA [43]
2007	Energy doubling observed of electrons from the 42 GeV SLAC electron beam [44]
2014	Highly-efficient acceleration of electrons with gradients of up to 5 GeV m^{-1} reported and a transfer efficiency of 18% [45]
2018	The AWAKE experiment [46] at CERN reports the first demonstration of electron acceleration in a self-modulated wake-field driven by a 400 GeV proton beam [47]
2018	First beam-plasma interactions at FLASHForward
2019	Publication from FACET-I demonstrates plasma photocathode injection for the first time [48]
2019-20	First published results from FLASHForward including energy dechirping [49], beam-based wake-field sampling [37] and energy-spread preservation of a witness-beam [50]

Table 1.2: Selected highlights from the development of PWFA from the 1980s to the present day

celeration [41] and witness-beam injection and acceleration. The next generation, FACET-II, is currently being commissioned with experimental runs beginning in due course.

1.3.2 Injection in plasma-based accelerators

While the high gradients provided by plasma accelerators have been well demonstrated, the utilisation of these fields remains a challenge to researchers. Injection is the term used to describe the process of positioning a secondary or witness bunch in the cavity behind the driver, so that it may be accelerated by the accelerating gradients. In PWFA, the technique used is typically one of the following:

- Ionisation injection, which uses the fields of either the driver [51] or the wake-field [52] itself to ionise additional electrons in the blowout, which are then immediately trapped and accelerated
- Plasma-photocathode injection [53], in which an additional laser ionises electrons directly within the blowout
- Density-down-ramp injection [54] also known as plasma-cathode injection [55], in which density gradients in the plasma change the trajectories of the electrons such that they are subsequently trapped and accelerated
- External injection, in which an additional electron bunch is extracted from an accelerator and inserted behind the driver prior to the plasma.

The choice of method typically depends on the desired properties of the witness-beam or the exclusion of methods based on feasibility studies in simulations. For example, the beam current may be too low for injection techniques such as ionisation injection [56].

This work centres around the injection of a witness-beam on a density down-ramp which has been ionised by a laser. In the literature this may be referred to as Laser-Triggered Density-Down-ramp Injection (LT-DDI), Plasma Torch, or Plasma-Cathode Injection. This method has been shown in simulation to be capable of producing high-quality beams [52] and could be used to improve upon the quality of beams in order to increase the light yield at an FEL.

1.4 Outline of the thesis

This thesis presents the development of a plasma cathode at FLASHForward and is structured into five main chapters. This chapter, the introduction, attempts to centre this work in the wider context of the field of plasma accelerators and accelerators technology. Chapter 2 introduces the mathematical background behind the physics which will be discussed in this work. Chapter 3 introduces the internal-injection experiment at FLASHForward, including the FLASHForward facility and presents the set up specific to the internal injection experiment. Chapter 4 uses simulations to establish the working parameter space needed for a successful internal-injection experiment. The results from an experimental run in November 2019 are then presented in Chapter 5, showcasing the first stable demonstration of down-ramp injection observed in PWFA.

2

Theoretical background

This chapter outlines the fundamental physical principles upon which this work is based. Starting in Section 2.1 from the Maxwell equations, the principles behind electromagnetic waves will be explored. Next, in Section 2.2, the principles behind the exploitation of electromagnetic waves in the form of laser light are explored. Section 2.3 then describes the physics of plasmas before Section 2.4 details how laser pulses can be used to form a plasma according to ionisation models. The expressions used to describe the evolution of a charged particle beam are discussed in Section 2.5. Section 2.6 describes how the theory behind the production of a GeV centimetre-scale particle accelerator. Finally Section 2.7 then discusses the processes used to harness the capabilities of a plasma accelerator by precisely injecting an electron bunch where it can become trapped and accelerated.

2.1 Maxwell's Equations

Since electromagnetism forms the backbone of laser physics and the acceleration of a charged particle beam, the starting point for this work is the Maxwell Equations (Eqs. 2.1-2.4) .

$$\boldsymbol{\nabla} \cdot \vec{E} = \frac{1}{\epsilon_0}\rho \tag{2.1}$$

$$\boldsymbol{\nabla} \cdot \vec{B} = 0 \tag{2.2}$$

$$\boldsymbol{\nabla} \times \vec{E} = -\frac{\partial \vec{B}}{\partial t} \tag{2.3}$$

$$\boldsymbol{\nabla} \times \vec{B} = \mu_0 \left(j + \epsilon_0 \frac{\partial \vec{E}}{\partial t} \right), \tag{2.4}$$

where $\vec{E}$ and $\vec{B}$ represent the electric and magnetic fields, ρ and j represent the charge and current densities. ϵ_0 and μ_0 are the constants of vacuum permittivity and vacuum permeability respectively.

In a vacuum ($\rho = 0, j = 0$) these equations reduce to the following forms

$$\boldsymbol{\nabla} \cdot \vec{E} = 0, \tag{2.5}$$

$$\boldsymbol{\nabla} \cdot \vec{B} = 0, \tag{2.6}$$

$$\boldsymbol{\nabla} \times \vec{E} = -\frac{\partial \vec{B}}{\partial t}, \tag{2.7}$$

$$\boldsymbol{\nabla} \times \vec{B} = \mu_0 \epsilon_0 \frac{\partial \vec{E}}{\partial t}. \tag{2.8}$$

Starting by taking the curl of Faraday's law (Eq. 2.7) and using the identity

$$\boldsymbol{\nabla} \times \boldsymbol{\nabla} \times \vec{A} = \boldsymbol{\nabla}\left(\boldsymbol{\nabla} \cdot \vec{A}\right) - \nabla^2 A$$

$$\boldsymbol{\nabla} \times \boldsymbol{\nabla} \times \vec{E} = -\frac{\partial \boldsymbol{\nabla} \times B}{\partial t} \tag{2.9}$$

$$\boldsymbol{\nabla}\left(\boldsymbol{\nabla} \cdot \vec{E}\right) - \nabla^2 E = -\frac{\partial}{\partial t}\left(\mu_0 \epsilon_0 \frac{\partial \vec{E}}{\partial t}\right), \tag{2.10}$$

Since according to Equation 2.5, $\boldsymbol{\nabla} \cdot \vec{E} = 0$, a wave equation for the electric field is obtained

$$\nabla^2 E - \frac{1}{c^2}\frac{\partial^2 E}{\partial t^2} = 0, \tag{2.11}$$

where $c = 1/\sqrt{\mu_0 \epsilon_0} = 299792458$ m s^{-1} is the speed of light in vacuum. When the same steps are applied to Ampere's Law (Eq. 2.8) and Equation 2.7 is used for the curl of the electric field, a complimentary wave equation for the magnetic field is retrieved:

$$\nabla^2 B - \frac{1}{c^2}\frac{\partial^2 B}{\partial t^2} = 0. \tag{2.12}$$

Equations 2.11 and 2.12 are wave equations which describe how light will behave and propagate in a vacuum. In media such as air or glass, the propagation velocity c is modified by the permittivity and permeability constants of the medium, ϵ_n and μ_n respectively. Further modifications will occur when j and ρ are not identically zero . This will result in a modified speed of light which is given by

$$c = \frac{1}{\sqrt{\epsilon_n \epsilon_0 \mu_n \mu_0}}. \tag{2.13}$$

A trial solution for these equations takes the form of:

$$E = E_0 e^{i(\omega t \pm k\vec{z})} \qquad B = B_0 e^{i(\omega t \pm k\vec{z})}, \tag{2.14}$$

where E_0 and B_0 are normalisation constants, ω and k are the angular frequency and the wave number respectively. These can be inserted into Equation 2.11 or Equation 2.12 to yield the relationship between these properties and the speed of light,

$$c = \frac{\omega}{k}. \tag{2.15}$$

The coupling of the electric and magnetic fields can also be seen using either Equation 2.7 or Equation 2.8 to yield,

$$\vec{B} = \frac{k}{\omega}\vec{z} \times \vec{E}. \tag{2.16}$$

2.2 Laser Physics

The laser (Light Amplification by Stimulated Emission of Radiation) has become a ubiquitous part of modern technology [57]. Therefore it is important to understand the underlying mechanisms behind the production of these pulses.

The three fundamental mechanisms of photon interaction with the electronic states of the atom were initially described by Einstein in 1917 and are known as absorption, spontaneous emission and stimulated emission [58]. In absorption (Fig. 2.1a), a photon with energy $E = \hbar\nu$, excites an electron from its ground state $E = E_0$ to a higher energy state $E = E_1$, where $\Delta E = E_1 - E_0 = \hbar\nu$. In spontaneous emission the electron transitions from the higher energy state E_1 to the lower state E_0, emitting a photon with energy $\Delta E = E_1 - E_2 = \hbar\nu$ in the process. The third mechanism, stimulated emission (Fig. 2.1c), is similar to spontaneous emission, except that the decay is induced by the presence of a second photon interacting with the atom, emitting a photon with identical phase and propagation direction.

The emission of a significant number of photons requires the rate of stimulated emission to be greater than that of absorption. Hence the number of electrons in the upper state N_1 must be greater than the number in the ground state N_0. This state, where $N_1 > N_0$, is known as population inversion and is typically not obtainable without the input of energy into the system or pumping. However, it can be shown that an overall population inversion is not obtainable in the two-state system shown in Figure 2.1 [59]. Rather, a system with three or more states is required for lasing. Examples of three-level systems include the Ruby laser, while four levels are common in dye lasers or doped crystals such as Titanium-Sapphire [60]. While population inversion may be achieved in a system with three or more states, it is more efficient (requiring a lower population of the upper energy levels) in a four-level system [61]. A diagram of a (a) three- and (b) a four-level system may be seen in Figure 2.2.

Once population inversion is achieved in a laser medium, the produced radiation must be amplified. Lasing typically begins with the spontaneous emission of a photon, which will stimulate the emission of further photons from other nearby atoms. A combination of mirrors and optics can be carefully placed around the lasing medium in order to continuously reflect photons through the medium in order to form a resonant cavity which will amplify the radiation produced.

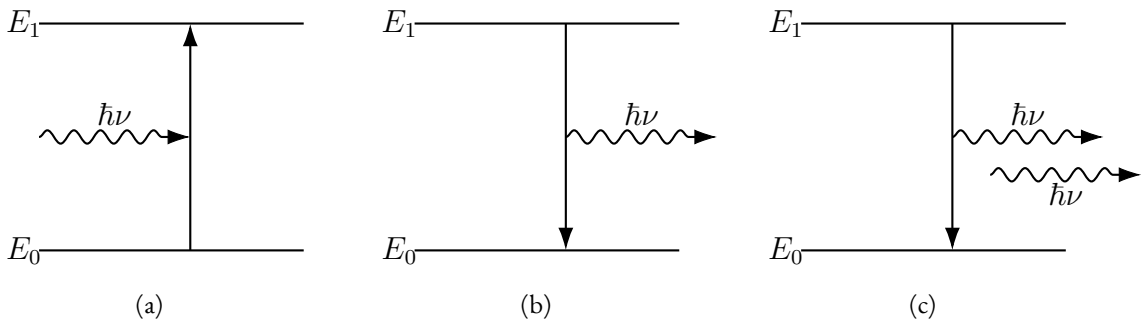

Figure 2.1: Diagrammatic representation of (a) absorption, (b) spontaneous emission and (c) stimulated emission by an atomic electron

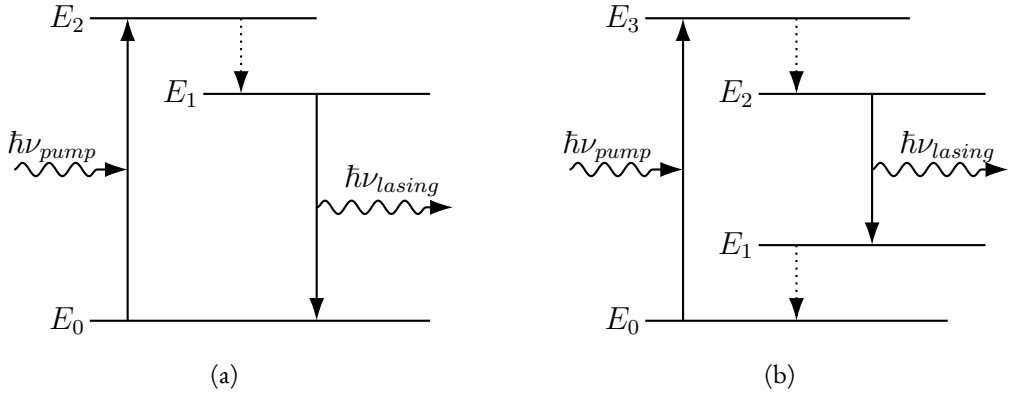

Figure 2.2: Diagrammatic representation of (a) a three-level laser system (3L) and (b) a four-level laser system (4L). Each system is pumped from its ground state E_0 to the upmost energy state (3L:$E2$, 4L: E_3) by a secondary laser with frequency λ_{pump}. This state then decays to a lower-energy state (3L: E_1 4L: E_2) from which it lases at λ_{lasing} to a lower-energy state. In a 3L system this is the ground-state whereas in a 4L system this is another energy state E_1 which then decays to the ground-state.

2.2.1 Physics of pulsed laser systems

In certain gain media such as titanium-doped sapphire crystals (Ti:Sapphire), the gain spectrum is sufficiently broad that many lasing wavelengths or modes will be supported by the cavity. This, with the invention of techniques such as modelocking [62] enables the cavity to produce a short femto-second laser pulse instead of a continuous output within a very narrow bandwidth. The width of the pulse in the frequency domain or its *bandwidth* will hence produce a pulse of corresponding length in the time domain. The amplification of these pulses is then typically carried out using Chirped Pulse Amplification (CPA) [63] in an amplification chain.

The process of CPA and the recompression of the pulse modifies the spectral phase of the laser pulse in order to increase or stretch, and later decrease or compress, its duration in the time domain. The optimisation of the spectral phase is crucial to achieving a short, intense laser pulse and therefore the mathematics is explored here.

Starting in the time domain, the electric field of a laser pulse is given by,

$$E(t) = |E(t)| \exp\left[i\left(\psi(t) - \omega_L t\right)\right] + c.c, \tag{2.17}$$

where $E(t)$ represents the pulse shape as a function of time, $\psi(t)$ is the phase as a function of time, ω_L is the carrier frequency and $c.c$ is the complex conjugate [64]. Due to the nature of ultra-short pulses, it is also essential and often useful to consider them in the spectral domain. This is achieved by means of a Fourier transform between the temporal and spectral domains (Equation 2.18),

$$E(t) = \frac{1}{2\pi}\int_0^\infty E(\omega)e^{-i\omega t}\mathrm{d}\omega; \quad \tilde{E}(\omega) = \int_{-\infty}^\infty E(t)e^{-i\omega t}\mathrm{d}t, \tag{2.18}$$

hence, in the spectral domain the equation for the electric field takes the form of:

$$E(\omega) = |E(\omega)| \exp\left[i\psi_\omega(\omega)\right], \tag{2.19}$$

where $|E(\omega)|$ is the magnitude of the electric field and $\psi(\omega)$ is the spectral phase. This

term can be expanded as a Taylor series around the central frequency ω_L in Equation 2.20,

$$\psi(\omega) = \psi_0^{(0)} + \psi_0^{(1)}(\omega - \omega_L) + \frac{\psi_0^{(2)}}{2!}(\omega - \omega_L)^2 + \frac{\psi_0^{(3)}}{3!}(\omega - \omega_L)^3 + \ldots, \tag{2.20}$$

where $\psi_0^{(n)} = \mathrm{d}^n\psi/\mathrm{d}\omega^n$. The spectral phase determines the relative position in time of the frequencies contained within the pulse. To achieve the shortest possible pulse, all frequencies must arrive at the same time. If they do not, the resulting effect is known as chirp [65].

2.2.2 Gaussian beam optics

Starting with either equation 2.12 or 2.11, it is possible to separate the spatial and temporal terms of a trial equation in order to derive the Helmholtz equation for the spatial electromagnetic field, which is given by,

$$(\nabla^2 + k^2)\vec{E}(x, y, z) = 0. \tag{2.21}$$

It is then assumed that the electric field varies significantly faster along its propagation direction [61]. This is known as the paraxial approximation, in which the electric field $\vec{E}(x, y, z)$ is separated into a rapidly varying axial component given by e^{ikz} and a slower varying component transverse to the propagation axis of $\psi(\vec{r})$, where cylindrical coordinates are now used for the plane transverse to the propagation axis. Inserting this solution $E = \psi(\vec{r})e^{ikz}$ into Equation 2.21 yields the following,

$$\frac{1}{r}\frac{\partial}{\partial r}\left(r\frac{\partial\psi}{\partial r}\right) - 2ik\frac{\partial\psi}{\partial z} = 0. \tag{2.22}$$

A solution to this equation is given by Equation 2.23, which describes the fundamental mode of a Gaussian laser beam

$$\vec{E}(r, z) = E_0\frac{w_0}{w(z)}\exp\left\{\left(-\frac{r^2}{w(z)^2}\right)\right\}\exp\left\{\left(-i\left(kz + k\frac{r^2}{2R(z)} - \phi(z)\right)\right)\right\}, \tag{2.23}$$

where r is the radial distance from the central axis, z is the axial distance from the beam's focus, E_0 is the amplitude of the field at the origin, $w(z)$ is the radial distance at which the field

amplitude is e^{-1} of its axial value, also known as the spot size, w_0 represents the value at the beam waist $w(z=0)$, k is the wave number which is defined as $k = 2\pi/\lambda$ for wavelength λ, $R(z)$ is the radius of curvature of the wave-front and $\phi(z)$ is the Gouy phase, which accounts for the phase transformation as the beam propagates through its beam waist.

The properties $w(z)$ and w_0 are closely related to an additional property known as the Rayleigh length. This length defines the rate at which the beam diverges from its focal point. This is given by

$$z_r = \frac{\pi\omega_0^2}{\lambda}. \tag{2.24}$$

Then, as the beam propagates along the z axis, the spot size $\omega(z)$ will increase according to

$$\omega(z) = \omega_0\sqrt{1 + \frac{z^2}{z_r^2}}. \tag{2.25}$$

2.2.2.1 Beam-size and intensity of a gaussian laser pulse

For a beam which is collimated or at focus, such that $\frac{w_0}{w(z)} = 1$, the observable intensity pattern in vacuum, I, of the field is given by Equation 2.26 [61],

$$I = \frac{c\epsilon_0}{2}\vec{E}\vec{E}^*, \tag{2.26}$$

where $\vec{E}^*$ is the complex conjugate of the electric field [61], which leads to the intensity profile,

$$I(r,z) = I_0 \exp\left\{\left(-2\frac{r^2}{w(z)^2}\right)\right\}, \tag{2.27}$$

where I_0 is the axial intensity or peak intensity. In the case of a pulsed laser, an additional term is required to describe the temporal envelope of the pulse,

$$I(r,z,t) = I_0 \exp\left\{\left(-2\frac{r^2}{w(z)^2}\right)\right\} \exp\left\{\left(-\frac{t^2}{2\sigma_t^2}\right)\right\}, \tag{2.28}$$

where σ_t is the RMS pulse length. The pulse length and spot size of such a laser pulse are often described in terms of the Full Width at Half Maximum (FWHM) which can be converted to

$w(z)$ and σ_t with the following,

$$w(z) = \frac{FWHM}{\sqrt{2\ln 2}} = 0.849\, FWHM. \tag{2.29}$$

$$\sigma_t = \frac{FWHM}{2\sqrt{2\ln 2}} = 0.425\, FWHM. \tag{2.30}$$

In order to determine the energy of the pulse, Equation 2.28 is integrated to form

$$\begin{aligned} \mathcal{E} = I_0 \int_{-\infty}^{\infty} \exp\left\{\left(-2\frac{r^2}{w(z)^2}\right)\right\} r dr\, d\theta \int_{-\infty}^{\infty} \exp\left\{\left(-\frac{t^2}{2\sigma_t^2}\right)\right\} dt \\ = I_0 \frac{\pi^{\frac{3}{2}}}{\sqrt{2}} \sigma_t w_0^2. \end{aligned} \tag{2.31}$$

Thus the expected peak intensity of a Gaussian laser pulse with energy $\mathcal{E}$ is given by Equation 2.32

$$I_0 = \frac{\sqrt{2}}{\pi^{\frac{3}{2}} \sigma_t w_0^2} \mathcal{E}. \tag{2.32}$$

The peak intensity of a laser may be directly measured and therefore is often used to validate simulations and estimate the physics which will take place in the focal region.

2.2.3 Fourier Optics

While it is useful to mathematically model a pure Gaussian laser pulse in its starting plane or near-field, the modelling of the propagation of such a pulse through optical components and to its focal plane requires a more in-depth description. Additionally, while the exact focal spot radius and shape is known for a Gaussian beam, this is more complicated for beams whose profiles do not follow that of an idealised Gaussian.

Starting with the formula for Fraunhofer diffraction of a given spatial electric-field profile defined by $E(x, y, z = 0)$ to that at another position in space $E(u, v, z)$ is given by Equation 2.33 [66],

$$E(u,v) = \frac{e^{ikz}}{i\lambda z}\exp\left(\frac{ik}{2z}(u^2+v^2)\right)\int_\infty^\infty\int_\infty^\infty\left\{E(x,y)\exp\left(\frac{ik}{2z}(x^2+y^2)\right)\right\} exp\left(-i\frac{2\pi}{\lambda z}(xu+vy)\right)\mathrm{d}x\mathrm{d}y, \quad (2.33)$$

where λ is the wavelength of the field. Simplifying to one transverse dimension (x, u), it may be shown that Equation 2.33 is a Fourier transform in Equation 2.34,

$$E(u) = \frac{e^{ikz}}{i\lambda z}\exp\left(\frac{ik}{2z}u^2\right)\int_\infty^\infty\left\{E(x)\exp\left(\frac{ik}{2z}x^2\right)\right\} exp\left(-i\frac{2\pi}{\lambda z}xu\right)dx. \quad (2.34)$$

When a field profile such as $E(x, y, z = 0)$ passes through a focusing optic such as a lens with focal length f, it can be shown that behind the lens its field is described by Equation 2.35. Mathematically this is almost identical to the 'defocusing' Z_2^0 Zernike polynomial, which will be shown later,

$$E_l = E_0\exp\left(-\frac{ik}{2f}(x^2+y^2)\right), \quad (2.35)$$

or in one dimension by, [66]

$$E_l = E_0\exp\left(-\frac{ik}{2f}x^2\right). \quad (2.36)$$

Using these terms with either of Equations 2.34 or 2.33, and propagating to the far field with $z = f$, the phase factor of the lens will exactly cancel the quadratic phase factor, leaving an exact Fourier transform in Equations 2.38 & 2.37 between the near-field of the x & y plane to the far-field of the u & v plane,

$$E(u,v) = \frac{e^{ikz}}{i\lambda f}\exp\left(\frac{ik}{2f}(u^2+v^2)\right)\int_\infty^\infty\int_\infty^\infty E(x,y)\exp\left\{\left(-i\frac{2\pi}{\lambda f}(xu+vy)\right)\right\}\mathrm{d}x\mathrm{d}y, \quad (2.37)$$

$$E(u) = \frac{e^{ikz}}{i\lambda f}\exp\left(\frac{ik}{2f}u^2\right)\int_\infty^\infty E(x)\exp\left\{\left(-i\frac{2\pi}{\lambda f}xu\right)\right\}dx. \quad (2.38)$$

These equations may be solved analytically for simple forms of $E(x, y)$ such as a pure Gaus-

sian shape, or numerically for more complicated forms, including those of real-world laser systems [67]

2.2.4 Aberrations and Zernike Polynomials

Typically the electric field produced by a typical laser system will not be mathematically perfect Gaussian beam such as those described in Equation 2.23. These deviations or aberrations usually are in the form of distortions of the spatial phase of the laser pulse which manifest in the deviation of the spatial intensity from its idealised form. In a laser system with a large number of aberrations, the final focal-spot intensity will be significantly reduced from its theoretical maximum value. This phase $\mathrm{X}(r)$ modifies the electric field of the laser pulse according to

$$E'(r) = E_0 e^{ik\mathrm{X}(r)}. \tag{2.39}$$

The aberrations may be described using a series of polynomials known as the Zernike Polynomials [68]. The first twenty-one polynomials are shown in Figure 2.3. The Zernike polynomials are a series of polynomials that are orthogonal on the unit circle and, crucially, allow any arbitrary aberration of laser phase to be decomposed into a sum over the series.

$$\mathrm{X}(r) = \sum_{n,m} C_{n,m} Z_{n,m}, \tag{2.40}$$

where $C_{n,m}$ is a normalisation constant and $Z_{n,m}$ is the Zernike polynomial with the indices n and m. The most interesting of these polynomials are those in the third row which are listed in Table 2.1. Taking the form of the Z_2^0 polynomial, it is possible to write its effect on an electric field U_0 as,

$$E'(r) = E_0 \exp\Big(ikC_2^0\sqrt{3}\big(2r^2 - 1\big)\Big). \tag{2.41}$$

It can be shown that this is mathematically identical to that of a lens with an effective focal-length of

$$\frac{1}{f} = -2C_2^0\sqrt{3}, \tag{2.42}$$

this will be explored later in Appendix A to derive the shift in focal spot position produced by a given value of C_2^0.

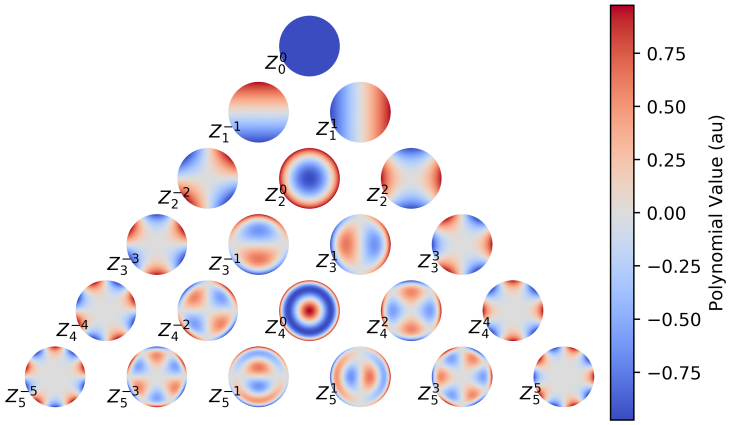

Figure 2.3: The first twenty-one Zernike Polynomials

	Z_j	name
Z_2^{-2}	$\sqrt{6}r^2 \sin 2\theta$	Oblique Astigmatism
Z_2^0	$\sqrt{3}\left(2r^2 - 1\right)$	Defocus
Z_2^2	$\sqrt{6}r^2 \cos 2\theta$	Vertical Astigmatism

Table 2.1: The mathematical forms of the oblique astigmatism, defocus and vertical astigmatism Zernike Polynomials.

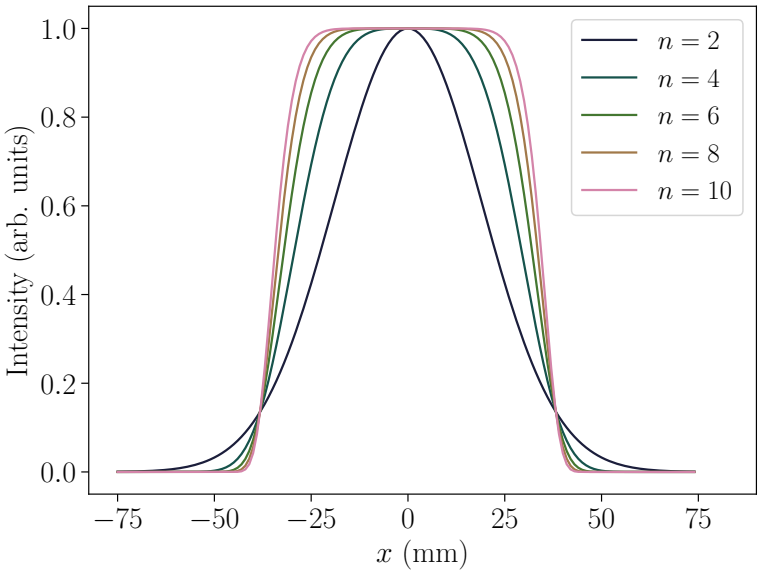

Figure 2.4: A super-Gaussian spatial profile, as defined in Equation 2.43, plotted with values of n between 2 and 10

2.2.5 Super-Gaussian beam profile

In many lasers the spatial profile of the beam is Gaussian profile, but rather super-Gaussian, described by Equation 2.43 and is plotted in Figure 2.4.

$$I(r,z) = I_0 \exp\left\{-2\left(\frac{r}{w(z)}\right)^n\right\}., \text{where } n \geq 2, \tag{2.43}$$

where for $n = 2$, the standard Gaussian profile is retrieved, while larger values of n result in profiles with a distinct flat top and steep ramps.

This profile occurs as a result of the laser amplification chain. In order to extract the maximum amount of energy, the gain medium is typically saturated. This leads to gain saturation in the central region with additional amplification at larger values of r [69].

2.3 Physics of plasmas

A plasma is a gas in which some or all of the electrons are not bound to the ions in the form of atoms and are freely moving in a quasi-neutral medium. By definition, a plasma exhibits collective effects which we will be exploiting to accelerate electrons [70]. It is therefore necessary to explore some of the fundamental aspects of plasma physics to understand the processes which take place in such a medium.

2.3.1 Quasi-neutrality of plasmas

Despite being comprised of charged particles, plasmas are referred to as quasi-neutral. This is due to their ability to shield or screen out the electric field of a test particle.

First we consider a plasma formed of heavy immobile ions which are singly ionised such that $n_i = n_0$ where n_i is the density of the ions and n_0 is the nominal plasma density. To determine the distance over which the fields are screened, we need to determine the electrostatic potential $\phi(x)$. For the electrons, we start by assuming a Boltzmann distribution for the partition function $f(x, v)$ of the form,

$$f(x,v) = A\exp\left\{-\frac{1}{k_B T_e}\left(\frac{m_e v^2}{2} + e\phi(x)\right)\right\}, \tag{2.44}$$

where k_B is Boltzmann's constant, T_e is the temperature of the electron gas, m_e is the electron mass, v is the velocity, e is the elementary charge and A is a normalisation constant [70]. To determine the electron density, Equation 2.44 is integrated over v to form Equation 2.45,

$$n_e(x) = n_0\exp\left\{\frac{e\phi(x)}{k_B T_e}\right\}. \tag{2.45}$$

The electrostatic potential may then be determined using the Poisson equation, (Eq.2.46),

$$\nabla^2\phi = -\frac{1}{\epsilon_0}\rho, \tag{2.46}$$

where ϵ_0 is the vacuum permittivity and ρ is the charge density. ρ may also be expressed in terms of the electron and ion densities, n_e and n_i (Eq. 2.47) and the electrostatic potential (Eq. 2.48),

$$\rho(x) = e(n_i - n_e(x)) = en_0 \left(1 - \exp\left\{\frac{e\phi(x)}{k_B T_e}\right\}\right) \tag{2.47}$$

$$\rho(x) = -\frac{n_0 e^2}{k_B T_e}\phi(x), \tag{2.48}$$

where Equation 2.45 has been used for the electron density along with the Taylor expansion for $e^y \approx 1 + y$ for the exponential term, assuming small values of $e\phi(x)/k_B T_e$. Inserting Equation 2.48 into Equation 2.46 yields a differential equation for the electrostatic potential,

$$\frac{\mathrm{d}^2\phi}{\mathrm{d}x^2} = \frac{e^2 n_0}{\epsilon_0 k_B T_e}\phi(x), \tag{2.49}$$

which has the solution,

$$\phi(x) = \phi_0 \exp\left\{-\frac{x}{\lambda_D}\right\}, \tag{2.50}$$

where λ_D is known as the Debye length and defines the distance over which the electric fields are screened out by the electrons in the plasma, which is defined by Equation 2.51 [70],

$$\lambda_D = \sqrt{\frac{\epsilon_0 k_B T_e}{e^2 n_0}}, \tag{2.51}$$

for a single electron plasma species. For multiple species of charge q_i, density n_i and temperature T_i, this becomes a sum over each component of the plasma

$$\lambda_D = \sqrt{\epsilon_0 k_B \sum_{i=0}^{N} \frac{T_i}{q_i^2 n_i}}. \tag{2.52}$$

From this length, a sphere enclosing the volume over which charge is shielded may be defined. For such collective effects to occur, this sphere must contain many plasma particles such that

$$N_D = \frac{4}{3}\pi\lambda_D^3 n_e \gg 1. \tag{2.53}$$

While there are many different definitions of a plasma, a very common one is an ionised gas in which Equation 2.53 is satisfied.

2.3.2 Plasma Oscillation

The collective behaviour of a plasma also means that it can support many types of oscillations. In this work, the interest lies predominately in the Langmuir oscillation [70]. To derive the characteristic frequency of these oscillations, we consider an an arbitrary displacement of the plasma electrons δ_x, which yields a charge density of $\rho = ne\delta_x$. The electric field generated as a result is

$$E = -\frac{-ne\delta_x}{\epsilon_0}, \tag{2.54}$$

which from $m\ddot{\delta_x} = -eE$ yields the equation of motion,

$$m_e \frac{\mathrm{d}^2\delta_x}{\mathrm{d}t^2} = -\frac{ne^2\delta_x}{\epsilon_0}. \tag{2.55}$$

This can be then rearranged into the equation for a simple harmonic oscillator

$$\frac{\mathrm{d}^2\delta_x}{\mathrm{d}t^2} = -\frac{ne^2}{m_e\epsilon_0}\delta_x, \tag{2.56}$$

which has a characteristic frequency of

$$\omega_p = \sqrt{\frac{ne^2}{m_e\epsilon_0}}. \tag{2.57}$$

2.4 Ionisation

In the focus of an intense laser pulse, the electric field can exceed the atomic fields which bind electrons to their parent atoms. These intense fields modify the potential of the atom which allow the electron to escape. The most relevant mechanisms for this work are Tunnelling Ionisation (TI) and Barrier Suppression Ionisation (BSI).

The mechanism behind TI and BSI is largely the same for both processes and relies on the interaction between the electric field and the atomic potential well. This is illustrated in Figure 2.5b, in which the electric field (red) modifies the original potential shown in Figure 2.5a. On one side, the barrier is sufficiently suppressed that in a strong field the electron may no longer be bound (solid line) or low enough that its tunnelling probability is substantially

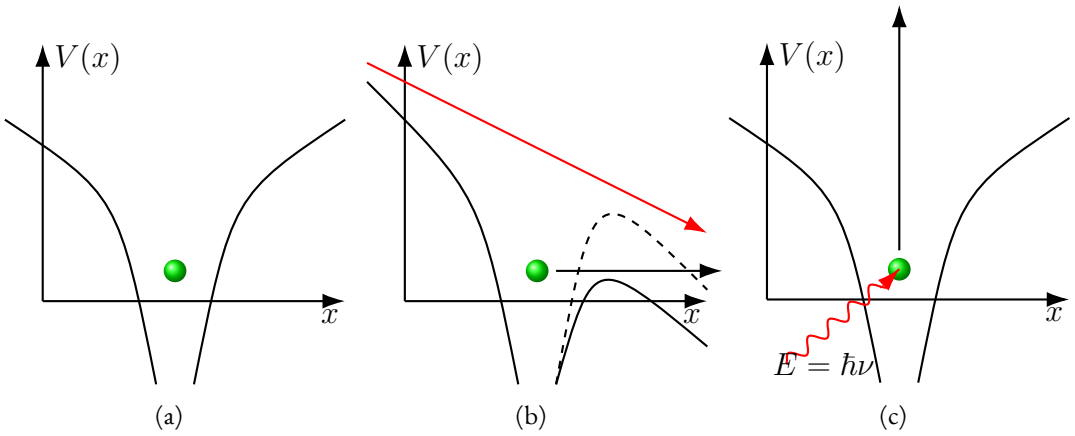

Figure 2.5: A sketch of the the ionisation processes considered in this work. (a) an electron bound in the potential field of an atom. (b) the same atom, now with an electric field which suppresses the potential well, a regime in which tunnelling ionisation is now possible. (c) a third possibility in which a photon directly interacts with the electron ionising it.

increased (dashed line).

Other mechanisms of note involve the interaction of the photons of the electric field directly with the bound electrons. If a single photon has sufficient energy, ie $\hbar\nu > E_b$ where E_b is the energy required to overcome the barrier, it may ionise the atom directly. For lower energy photons, the electron may absorb several photons at the same time in Multi-Photon Ionisation (MPI) [71].

The dominant ionisation process is typically determined by the Keldysh parameter [72].

$$\gamma_K = \sqrt{\frac{E_B}{2U_p}}, \tag{2.58}$$

where E_B is the binding energy of the atomic electron and $U_p \sim E^2/\omega_L$ is the pondermotive energy of a laser field E with frequency ω_L. This parameter also describes the ratio between the time taken for an electron to tunnel through the barrier and the period of the electric field [73]. As $\gamma_K \to 0$, the electric-field period is significantly longer than the tunnelling time, leading to the domination of tunnelling ionisation, with MPI becoming increasingly dominant as $\gamma_K \to \infty$. Some ionisation energies relevant for this work are tabulated in Table 2.2.

Species	Ionization energy (eV)
He-I	24.59
He-II	54.42
Ar-I	15.76
Ar-II	27.63
Ar-III	40.74

Table 2.2: Table of ionisation energies in electron volts.

Earlier theories mostly considered the ionisation potential of a single hydrogen atom [74] in the TI regime. This was later extended by Ammosov, Delone and Krainov for more complex atomic cases [75]. Since then many efforts have been made to extend the theory into the BSI regime [76].

In atomic units the ionisation rate is given as a function of the electric field E by,

$$w_{ADK}(E) = \frac{C_l^2}{2^{|m|}|m|!}\frac{(2l+1)(l+|m|)!}{2(l-|m|)!}\frac{1}{\kappa^{\frac{2Z_i}{\kappa}-1}}\left(\frac{2\kappa^3}{E}\right)^{\frac{2Z_i}{\kappa}-1}\exp\left(-\frac{2\kappa^3}{3E}\right), \quad (2.59)$$

where l & m are the quantum numbers of the valence electron, C_l is a dimensionless constant determined by the atomic wave function. $\kappa = \sqrt{E_B}$, where E_B is the ionisation energy of the electron in atomic units, Z_i is the ionisation level of the atom and E is the electric field in atomic units [76]. The ionisation rate described by 2.59 is used to determine the plasma density by solving the following differential equation

$$\frac{\mathrm{d}n}{\mathrm{d}t} = w_{Ion}(1-n), \quad (2.60)$$

where $n = n_e/n_0$ is the ionisation ratio of a single ionisation species, where $n = 1$ corresponds to full ionisation and $n = 0$ is neutral. Solving equation 2.60 for $n(t)$ yields,

$$n(t') = 1 - \exp\left(-\int_{-\infty}^{t'} w_{Ion}(t)\mathrm{d}t\right). \quad (2.61)$$

2.5 Physics of charged particle beams

The plasma oscillations in a wake-field accelerator are driven by either a laser pulse or a charged particle beam in order to accelerate a secondary or witness-beam. Therefore this section discusses the physics of these beams and their evolution in an accelerator. The mathematical description of these beams is carried out in a similar fashion to a laser pulse, but often the two have diverging descriptions.

2.5.1 Single particle dynamics

The dynamics of a single particle in an accelerator may be described in terms of just six properties. These are

- x - position
- y - position
- s - longitudinal position
- x' - divergence in x where $x' = \frac{p_x}{p_z}$
- y' - divergence in y where $y' = \frac{p_y}{p_z}$
- δ - relative energy or momentum where $\delta = \frac{p_z}{<p_z>}$

where x and y are the two dimensions transverse to the propagation axis z and $p_{x,y,z}$ denotes the particle's momentum in each direction. A particle in an accelerator is usally contained within a group of other particles or a 'bunch'. Therefore an individual particle's properties are often compared against those of an average or reference particle. These terms will be denoted by angular brackets $<>$. The transmission of such a particle is defined by the transfer matrix of an accelerator component or subsection.

$$U(z) = \mathbf{M}U_0, \tag{2.62}$$

where U represents the vector $(x, x', y, y', s, \delta)$ and $\mathbf{M}$ is the 6D transfer matrix between s_0

and $s(z)$,

$$\mathbf{M} = \begin{pmatrix} R_{11} & R_{12} & R_{13} & R_{14} & R_{15} & R_{16} \\ R_{21} & R_{22} & R_{23} & R_{24} & R_{25} & R_{26} \\ R_{31} & R_{32} & R_{33} & R_{34} & R_{35} & R_{36} \\ R_{41} & R_{42} & R_{43} & R_{44} & R_{45} & R_{46} \\ R_{51} & R_{52} & R_{53} & R_{54} & R_{55} & R_{56} \\ R_{61} & R_{62} & R_{63} & R_{64} & R_{65} & R_{66} \end{pmatrix}. \tag{2.63}$$

2.5.2 Multi-particle beam dynamics

In most cases, rather than being interested in the dynamics of a single particle traversing the accelerator, we are interested in those of a beam which is comprised of many such particles. Here, the collective properties of the beam are of higher interest than those of any one particle. These collective properties are typically quantified in terms of the mean and variance of the position and divergence, x and x'. The transverse position and divergence will ordinarily be distributed as a Gaussian around zero in both dimensions. Calculated for the whole beam, the so called trace space of the beam will resemble an ellipse as shown in Figure 2.6. When the beam is not being accelerated in the forward, s, direction, the area of the ellipse will typically be conserved as the beam traverses the accelerator. This quantity is known as the geometric emittance, ϵ_x, which is expressed in terms of the Twiss or Courant-Snyder parameters.

$$\epsilon = \gamma\langle x^2\rangle + 2\alpha\langle x\rangle\langle x'\rangle + \beta\langle x'^2\rangle, \tag{2.64}$$

where $\langle x\rangle$ and $\langle x'\rangle$ are the mean position and divergence of the beam and α, β and γ are the three Twiss parameters [77].As the geometric emittance will not be conserved when the beam experiences acceleration in the z direction, it is common to normalise the geometric emittance to a normalised emittance value according to

$$\epsilon^n_{x,rms} = \beta_z\gamma_r\epsilon_{x,rms}, \tag{2.65}$$

where $\beta_z = \frac{v}{c}$ and γ_r is the relativistic Lorentz factor. As the normalised emittance will be conserved throughout an aberration-free accelerator, it is often used as a merit function for the beam quality.

The beta function, $\beta(s)$, describes the beam envelope in the x direction and can be related

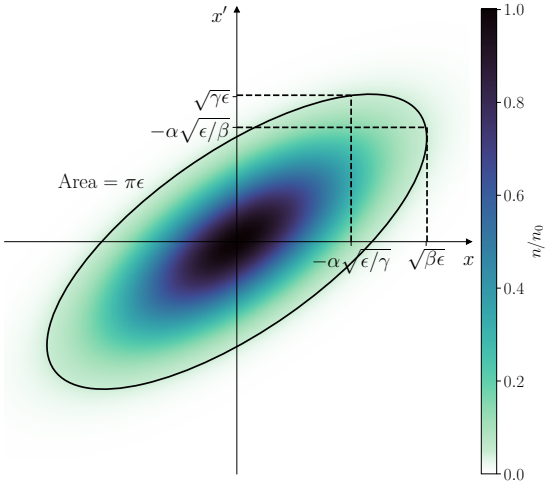

Figure 2.6: A sketch of the electron beam trace space in x and x', as well as the Twiss parameters

to the RMS bunch size according to

$$\sigma_{x,rms} = \sqrt{\beta(s)\epsilon_{x,rms}}, \tag{2.66}$$

where $\epsilon_{x,rms}$ is the geometric emittance. In an accelerator with a focusing strength of $k(s)$, the beta function will evolve according to

$$\beta''(s) + 2k(s)\beta(s) - \frac{2}{\beta(s)} = 0. \tag{2.67}$$

In the absence of any focusing forces $k(s)$ i.e, in a vacuum, the beta function evolves parabolically from its waist at s_0 according to

$$\beta(s) = \beta_0 + \frac{(s - s_0)^2}{\beta_0}, \tag{2.68}$$

from which the RMS beam size may be determined as a function of s.

2.6 Plasma wake-field acceleration.

The plasma accelerator, first proposed utilising a laser pulse in 1979 [32], is centred around the interaction of an intense beam packet with a plasma to produce intense fields, known as wake-fields, which can be used to accelerate a secondary beam. This was later extended to include

a beam based driver [34] [78]. The theory behind plasma wake-field acceleration (PWFA) is generally subdivided into two regimes. The first of these is the *linear regime* where the beam density is much smaller than the plasma density $n_b \ll n_e$. The second regime is consequently known as the *non-linear regime*, where much larger density perturbations occur as the beam density is equivalent to or greater than the plasma density.

2.6.1 Linear perturbation theory

When a low-density electron beam is incident into the plasma, the plasma will respond collectively according to the continuity equation as presented in [79],

$$\frac{\partial n_e}{\partial t} + \nabla \cdot (n_e \vec{v}_e) = 0, \tag{2.69}$$

while the electrons themselves will obey the equation of motion, under the assumption that the motion is non-relativistic such that $\vec{p}_e = m_e \vec{v}_e$,

$$\frac{\partial \vec{p}_e}{\partial t} = -e\left(\vec{E} + \vec{v}_e \times \vec{B}\right), \tag{2.70}$$

where n_e is the plasma density, v_e is the fluid velocity of the electrons and $\vec{E}$ & $\vec{B}$ are the electric and magnetic fields, respectively. These equations may be linearised by assuming a small perturbation in the plasma density on top of a constant plasma density n_0, i.e $n_e = n_0 + \delta n$ and that the velocities and their derivatives are small and so that second-order terms may be neglected, yielding

$$\frac{\partial \delta n}{\partial t} + n_0 \boldsymbol{\nabla} \cdot \vec{v}_e = 0, \tag{2.71}$$

the equation of motion then becomes

$$\frac{\partial \vec{v}_e}{\partial t} = -\frac{e\vec{E}}{m_e}. \tag{2.72}$$

By partially differentiating Equation 2.71 w.r.t time and inserting Equation 2.72, we arrive at

$$\frac{\partial^2 \delta n}{\partial t^2} - \frac{n_0 e}{m} \boldsymbol{\nabla} \cdot \vec{E} = 0. \tag{2.73}$$

The divergence of the electric field may then be obtained from Gauss's law, where we now

insert the beam density n_b into the total charge density

$$\boldsymbol{\nabla} \cdot \vec{E} = -\frac{e}{\epsilon_0} \left(\delta n + n_b \right). \tag{2.74}$$

Inserting this into Equation 2.73 yields the equation for a driven harmonic oscillator with a frequency of $\omega_p = \sqrt{ne^2/m_e\epsilon_0}$

$$\frac{\partial^2 \delta n}{\partial t^2} + \omega_p^2 \delta n = -\omega_p^2 n_b. \tag{2.75}$$

In many cases it is useful to work in a co-moving frame $\tau = z - ct$ which yields

$$\frac{\partial^2 \delta n}{\partial \tau^2} + k_p^2 \delta n = -k_p^2 n_b, \tag{2.76}$$

where $k_p = \omega_p/c$ is the characteristic wave number of the plasma. Equation 2.76 has an analytical solution which is found using Green's functions

$$\delta n(z, \mathbf{r}) = -k_p \int_z^\infty n_b \left(z', \mathbf{r} \right) \sin \left(k_p \left(z - z' \right) \right) dz' \tag{2.77}$$

Equation 2.77 is an analytical solution which describes the density perturbation of a linear wake-field. This solution is only valid in the case of small changes in the plasma density.

2.6.2 Non-linear wake-field regime

As the beam density increases beyond n_0, the wake-field behaviour will depart from the linear regime. Typically this regime has no general analytical solution and must therefore be modelled using numerical simulations. In this regime, the plasma electrons are expelled from the central axis, resulting in a central cavity with no plasma electrons. These electrons then return to the axis at a position known as the apex as a result of the electrostatic forces exerted by the ions which remain in the cavity. This cavity is known as the bubble or the blowout and the highly non-linear regime is therefore often referred as the bubble or blowout regime. Discussions of this regime including estimation of the radius of the blowout can be found in [80]. The magnitudes of the electric fields within this regime are typical given as a fraction of

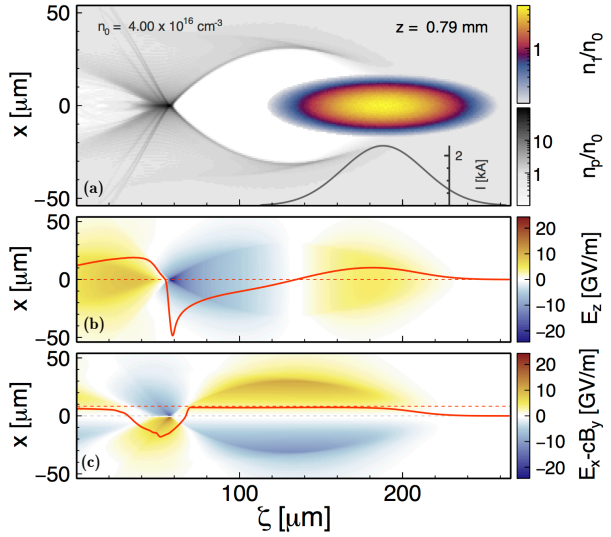

Figure 2.7: A snapshot from a simulation of a plasma wake-field accelerator

the so-called wave breaking field

$$E_z = \sqrt{\frac{m_e c^2 n_0}{\epsilon_0}}, \tag{2.78}$$

, or $E_z[\,\mathrm{V/m}] \approx 96\sqrt{n_0\,[\,\mathrm{cm}^{-3}]}$. A snapshot from a simulation is shown in Figure 2.7. Here (a) depicts the plasma and beam densities, (b) the accelerating fields and (c) the focusing fields.

2.7 Injection of beams into a plasma wake-field accelerator

One the most challenging aspects of plasma accelerator research is the optimal generation of a bunch to harness the accelerating fields which arise behind the driver. In order for this secondary or witness bunch to be accelerated by the wake-field, it must be precisely placed within the field such that it becomes confined by the boundaries of the field, or trapped. In a wake-field accelerator, the injection techniques used generally fall into two categories, known as external injection and internal injection. In external injection, a witness-beam is present behind the driver prior to its entry into the plasma. This beam may be sourced either from a separate accelerator, or from the same accelerator as the driver.

The later technique, internal injection, as its name suggests, sources the electrons which form a witness bunch from the plasma source. The exact origin of these electrons is dependent upon the method selected. In ionisation injection methods, they are ionised by intense electric fields induced by the wake-field [81] or the driver beam [82] or a laser pulse [53] to name but a few. For the purposes of this work, the focus of attention will be on a further method, density down-ramp injection.

2.7.1 Density Down-ramp Injection

Density down-ramp injection is a method that relies on the rephasing of electrons, which formerly constituted the plasma wake, inside the bubble created behind the driver. The proposed method, first described by [83] and investigated further by [84], manipulates the phase velocity of the plasma wake, by way of changing the plasma density which will in turn modify the wavelength and frequency of the plasma oscillation, leading to the rephasing and trapping of electrons in the wake-field.

For an electron in a wake-field, the longitudinal phase position will be defined by $\chi = k_p(z - \beta_b ct)$, where β_b is the velocity of the electron beam [52]. Assuming a longitudinal density variation of $n(z)$, the differential of this expression leads to one which describes the evolution of the phase along the z axis of the form,

$$\begin{aligned} \frac{\partial \chi}{\partial z} &= \frac{\partial}{\partial z} k_p(z - c\beta_b t) \\ &= \frac{\chi}{k_p}\frac{\partial k_p}{\partial z} + k_p \frac{\partial}{\partial z}(z - \beta_b ct) \end{aligned} \tag{2.79}$$

The differential $\frac{\partial k_p}{\partial z}$ may be solved using the chain rule of differentiation to yield,

$$\frac{\partial k_p(n)}{\partial z} = \frac{\partial k_p}{\partial n(z)} \cdot \frac{\partial n(z)}{\partial z}, \tag{2.80}$$

where $\frac{\partial n(z)}{\partial z}$ is the partial differential of the density along the z axis, which in this case reduces to a total derivative as the density, n, only varies along the z axis. The value of $\frac{\partial k_p}{\partial n(z)}$ is then

found using $k_p = \omega_p/c$ and $\omega_p = \sqrt{ne^2/m_e\epsilon_0}$ to yield the final expression for $\frac{\partial\chi}{\partial z}$,

$$\frac{\partial\chi}{\partial z} = \frac{1}{2}\frac{\chi}{n}\frac{\mathrm{d}n}{\mathrm{d}z} + k_p\left(1 - \frac{\beta_b}{\beta_z}\right), \tag{2.81}$$

where β_z is the electron velocity as a fraction of c at position z and where $\frac{\partial}{\partial z}\beta_b ct$ is assumed to have the form of $\frac{\beta_b}{\beta_z}$.

Equation 2.81 describes the evolution of the electron phase as a function of z position. When an electron is moving along with the phase velocity β_{ph}, i.e $\beta_z = \beta_p h$, Equation 2.81 will be identically zero and can be rearranged to express the phase velocity as a a function of the plasma gradient,

$$\beta_{ph} = \beta_b\left(\frac{1}{2}\frac{\chi}{n}\frac{1}{k_p}\frac{\mathrm{d}n}{\mathrm{d}z} + 1\right)^{-1}. \tag{2.82}$$

It may be useful to express the plasma density, n, in Equation 2.82 as a ratio of a reference density n_0 This normalised density, $\tilde{n} = n(z)/n_0$, results in the expression taking the form,

$$\beta_{ph} = \beta_b\left(\frac{1}{2}\frac{\chi}{\tilde{n}^{\frac{3}{2}}}\frac{1}{k_p^0}\frac{\mathrm{d}\tilde{n}}{\mathrm{d}z} + 1\right)^{-1}, \tag{2.83}$$

where k_p in Equation 2.82 has been replaced by $k_p^0\tilde{n}^{\frac{1}{2}}$ and $\frac{\mathrm{d}n}{\mathrm{d}z}$ is expressed as $n_0\frac{\mathrm{d}\tilde{n}}{\mathrm{d}z}$. Equations 2.82& 2.83 describe how the phase velocity of the wake-field behaves on a density transition. In the case of a decreasing plasma density ($\frac{\mathrm{d}\tilde{n}}{\mathrm{d}z} < 0$), the phase velocity will be reduced at the rear of the wake-field where $\chi < 0$. Steeper gradients and increasingly negative values of χ enhance this effect.

During the derivation of Equation 2.82 an intermediate step is reached,

$$\frac{1}{2}\frac{\chi}{n}\frac{1}{k_p}\frac{\mathrm{d}n}{\mathrm{d}z} = -k_p\left(1 - \frac{\beta_b}{\beta_z}\right). \tag{2.84}$$

This may be inserted back into Equation 2.81 to yield an expression for the phase shift experienced by a plasma electron on a density gradient,

$$\frac{\partial\chi}{\partial z} = k_p\beta_b\left(\frac{1}{\beta_{ph}} - \frac{1}{\beta_z}\right). \tag{2.85}$$

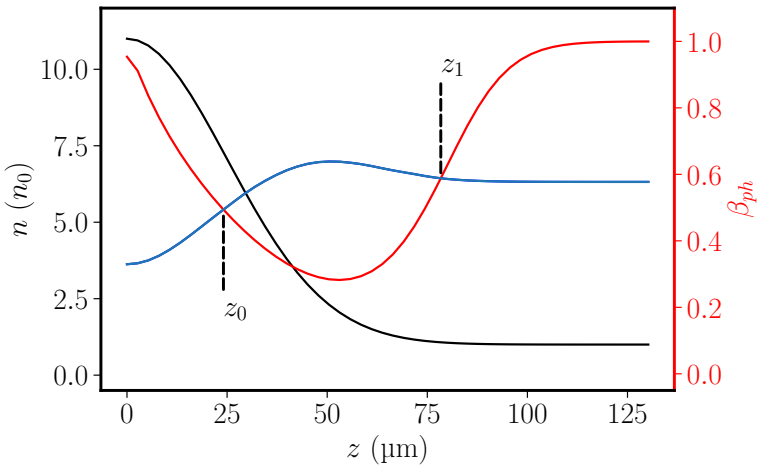

Figure 2.8: Schematic representation of the conditions necessary for density down-ramp injection. Here, the density ramp n_0 (black), phase velocity β_{ph} (red) and plasma electron velocity β_z (blue) are shown. The left-hand axis corresponds to the height of the density ramp, while the right hand axis defines the magnitude of the velocities (β_z & $\beta_p h$) The injection condition $\beta_z > \beta_{ph}$ is therefore satisfied between z_0 and z_1

This expression defines the injection condition for electrons on a density transition. In order for an electron to propagate forward and enter the accelerating phase of the wake-field , it must experience a positive phase shift i.e. $\frac{\partial \chi}{\partial z} > 0$. This condition is met when $\beta_z > \beta_{ph}$ [52]

This is illustrated in Figure 2.8 for an idealised Gaussian density ramp (black) which has a peak density which is a factor 10 times the base density n_0 of $4 \times 10^{16}\,\mathrm{cm}^{-3}$. The phase velocity (red) and the electron velocity at the rear of the wake-field (where $\chi = -2\pi$) (blue) are also plotted along the ramp. The phase velocities were calculated using Equation 2.83 and the plasma velocities determined from simulations and provided by the authors of [52]. On this down-ramp, the trapping condition is met after $24\,\mu\mathrm{m}$ (marked by z_0) and persists up until $78.4\,\mu\mathrm{m}$ (z_1). Between these two positions, the wake-field electrons will be moving faster than the wake, and may propagate forward into the accelerating region where they may be accelerated by the wake-field. These electrons will be trapped and not leave the accelerating region as long as their velocity remains higher than the phase of the wakefield $\beta_z > \beta_{ph}$.

2.7.2 Generation of density down-ramps at FLASHForward

Experimentally, there are two common methods of producing a density down-ramp. A hydrodynamic ramp may be created by the use of a gas cell or capillary fed by different gas pressures in order to create a density gradient across the whole target or a small region of it. This requires an intricately designed plasma target with multiple inlets as well as full hydrodynamic simulations to study the types of ramps which are achievable within the target. Alternatively, as is common in LWFA experiments, the plasma may be generated inside the plume of a gas jet [85] and an obstruction such as a knife edge is inserted into the plume to create a shock front inside the plume [86]. As will be discussed later, the gas load introduced by such as scheme will exceed the differential pumping system necessary for the windowless design of the FLASHForward experiment.

Laser Triggered Density Down-ramp Injection (LT-DDI) does not require the use of different gas pressures, complex target design or a gas jet. Instead it requires a plasma source that has multiple ionisation levels and/or an ignition method that will leave a certain portion of the gas un-ionized in order to form a density ramp.

One such method utilises a gas-filled target which is successively ionised by two laser pulses. The gas is formed from either a mixture of two or more gas species with distinct ionisation levels or a single species with multiple electrons available for ionisation at sufficiently distinct energies. The first laser propagates co-linearly along the electron beam axis and ignites a plasma along the length of the target. The intensity of this laser is set relatively low ($10^{13} - 10^{15}$ W cm^{-2}), such that only the first available electrons in the target are ionised, which is referred to as the background species. The second laser propagates transversely to the first and has a higher intensity at focus ($> 10^{15}$ W cm^{-2}) and is thus able to ionise substantially more electrons from the gas mixture. This secondary ionisation level is referred as the dopant species and the number of electrons available for ionisation is determined by the composition of the gas mixture. This secondary ionisation process creates a localised increase in the plasma density, which will hence forth be referred to as a "plasma-filament" . The exact target intensities of each laser pulse will depend on the energies required to ionise the valance electrons of the gas species in the mixture. A sketch of this method is shown in Figure 2.9.

This method has a number of advantages which include that the spatial dimensions of the plasma-filament are determined by the shape of the laser focus. The laser focus may be

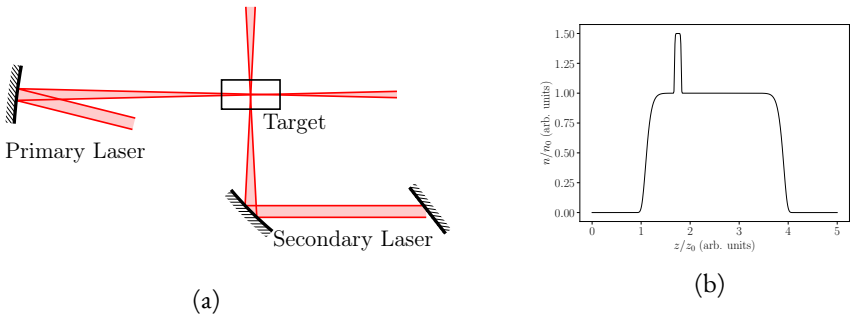

(a) (b)

Figure 2.9: Schematic of how one might achieve a down-ramp using a two-laser ignition method. (a) An example set up around a plasma target. (b) An example longitudinal axial density profile resulting from this scheme.

manipulated to produce plasmas of almost arbitrary shapes, which may be beneficial to the process of injection. The height of the ramp is determined by the mixing ratio between the dopant and background gas species.

3

The Internal-Injection Experiment at FLASHForward 'X-1'

This chapter describes the set-up of the internal-injection experiment at FLASHForward. The FLASHForward (Future ORiented Wakefield Accelerator Research and Development at FLASH) project was conceived to exploit the excellent quality of the electron beams provided by the FLASH accelerator. These electron beams ordinarily are capable of driving an FEL and therefore must be of a high quality and short bunch length [87]. These properties makes them well suited for use as a driver in plasma wake-field experiments. The aims of the internal injection experiment 'FLASHForward: X-1' are to inject and trap an electron bunch sourced from the plasma electrons which are already present in the plasma target.

Section 3.1 describes the FLASH accelerator from which the driver beams are sourced for the experiment. This accelerator feeds into the FLASHForward electron beam-line which is detailed in Section 3.2. The FLASHForward laser system and its transport to the interaction point are described in Section 3.3. Section 3.4 describes the target chamber where the interaction between the electron beam and plasma takes place, the diagnostics placed around the plasma chamber and the set-up specific to the internal injection experiment. Finally Section 3.5 describes the electron-beam diagnostics which are placed downstream of the plasma

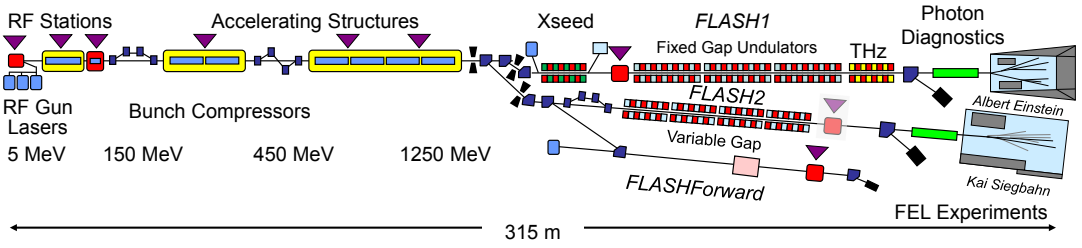

Figure 3.1: A schematic of the FLASH Facility including the LINAC and the three experimental beam-lines. Image from [91].

chamber and presents the parameters of the electron beams used in the experimental campaign as characterised by these diagnostics.

3.1 The FLASH Accelerator

FLASH (Free electron LASer in Hamburg) began its life as the Tesla Test Facility (TTF), a project designed to test the feasibility of super-conducting radio frequency (SRF) cavities for a future linear collider [88]. The FEL capabilities of the facility were understood from the beginning [89] and operation of the machine as an FEL user facility began in 2005. A schematic of the facility is shown in Figure 3.1.

The machine can roughly be divided into two major components. First is the accelerator itself including an RF gun and seven accelerating modules. Electron bunches of 0.1 nC–3 nC are accelerated from an RF gun up to 1250 MeV. The longitudinal phase space can be manipulated and compressed to a final bunch length between 50 and 5000 fs. As a result, beams with a peak current of up to 2.5 kA are available from FLASH. The second component consists of three experimental beam-lines [90]. FLASH1 and FLASH2 are FELs equipped with undulators and the third beam-line; FLASH3 currently feeds into FLASHForward, the dedicated PWFA research beam-line. Kicker magnets and dipole magnets are used to send the electron bunches into their designated beam-lines.

The FLASHForward electron beam-line starts at FLASH2 and transports the electron bunches to the Target Chamber. A sketch of the beam-line is shown in Figure 3.2. The beam-line starts with the FLF-EXTR (Extraction) section where a dipole magnet extracts the beam from FLASH2. The next section is the FLF-COMP (Compression) section, a dispersive section of the beam-line. This section together with the control over the phase space provided by the combination of RF cavities with multiple bunch compressors, means that a linear phase space may be produced before the beam enters the FLASHForward beam-line. Here, the longitudinal phase space may be manipulated using a "Scraper" device which is installed at the end of the section. The scraper consists of two blocks which may scrape the head and/or tail away from the beam. A wedge scraper is also present to separate a beam into two bunches, which may then be used for external acceleration experiments [92].

The next beam-line section is the FLF-MAFF (MAtching and Final Focus) which transports the beam to the target chamber. This section contains nine quadrupoles (five matching and four focusing) which are used to produce a tight focus in the target chamber, as well as matching the beam into the plasma.

A windowless transmission from the photocathode into the electron beam-line is achieved while preserving the high-quality FLASH vacuum $\mathcal{O}(10^{-9})$ mbar by means of a differential pumping system which is capable of reducing the pressure by seven orders of magnitude over 20 m. This is achieved through a series of narrow aperture beam pipes (between 10 and 20 mm) and differential pumping stations[1] [38].

[1] Each pumping station contains at least one turbo pump and backed by a scroll pump

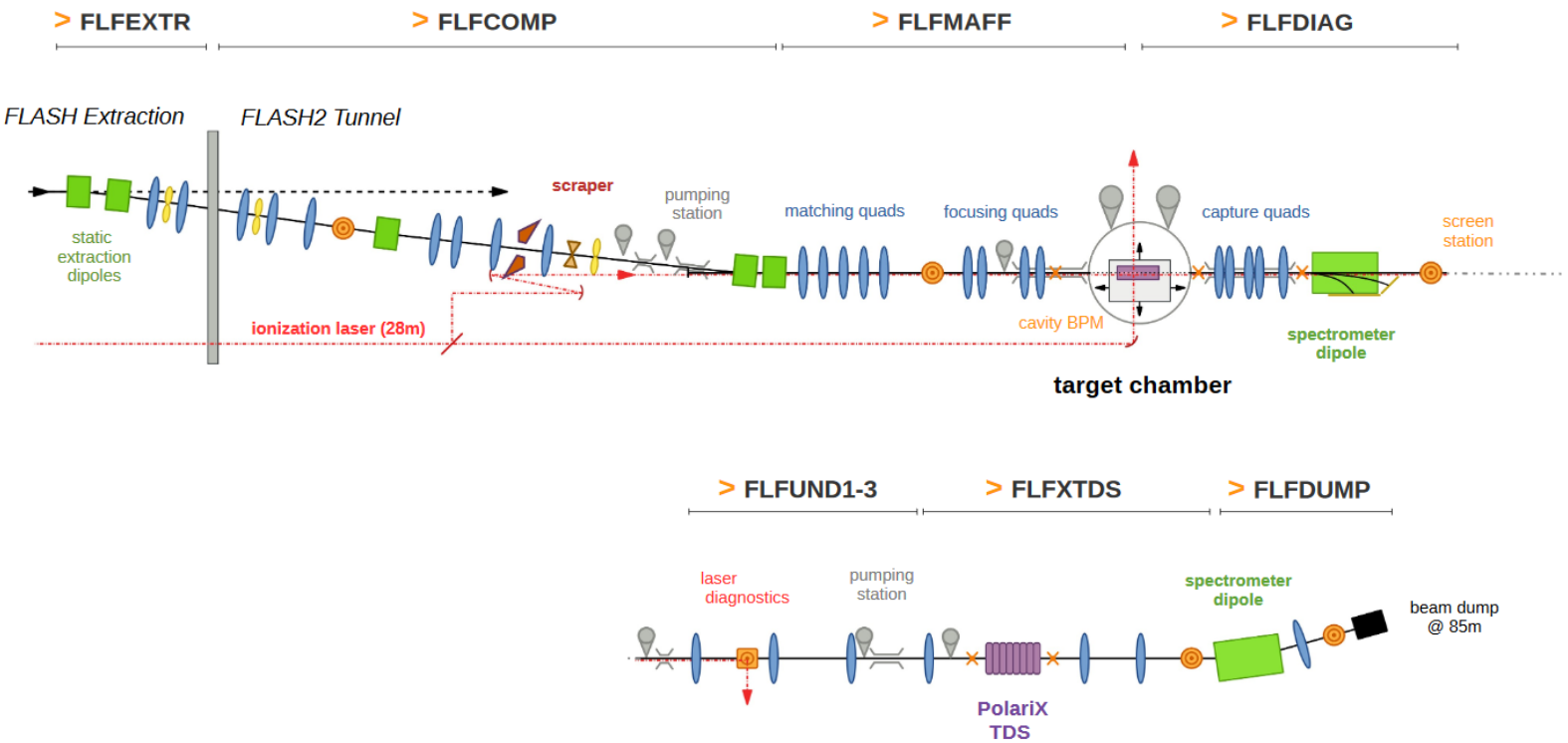

Figure 3.2: A schematic of the FLASHForward electron and laser beam-lines [93].

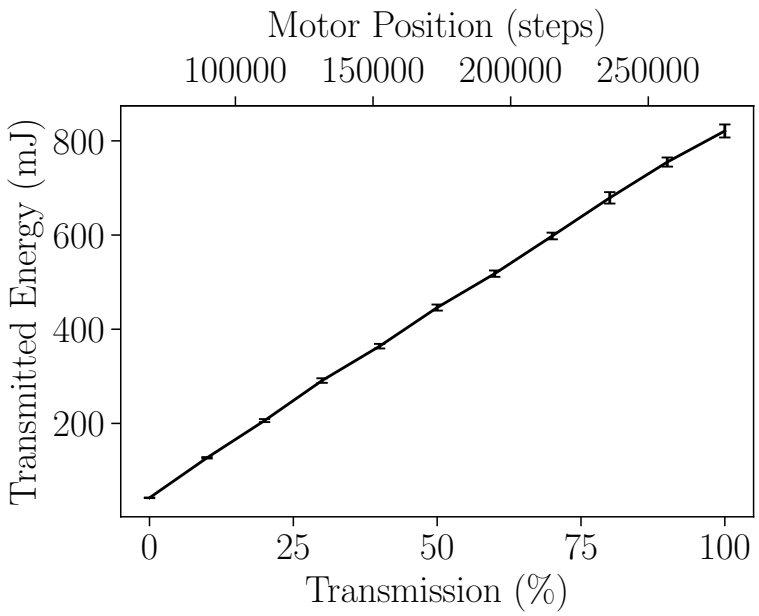

Figure 3.3: Characterisation of the laser attenuator showing the range of energies from 42 to 821 mJ. Data courtesy of M. Meisel

3.3 Laser system

The laser system at FLASHForward is a 10 Hz 25 TW Ti:Sapphire System produced by Amplitude Technologies. The system produces laser pulses with an energy of up to 800 mJ and compressed down to a pulse length of 25 fs.

The laser energy may be attenuated prior to compression with the use of a waveplate attenuator. This allows the output energy to be varied continuously between 42 to 821 mJ as plotted in Figure 3.3. A Dazzler (or an Acousto-Optic Programmable Dispersive Filter) device is also present in the amplification chain. The Dazzler allows the manipulation of the spectral phase of the laser to be optimised (Sec 2.2.1) in order to achieve optimum pulse compression. In a Dazzler device the laser pulse passes through a highly birefringent crystal. The crystal is pulsed with an acoustic wave in order to change the optical axis of propagation for the wavelengths which make up the laser pulse and optimise their relative position in the pulse [94].

3.3.1 Laser pulse transport

The transport of the laser pulse from the second-floor laser lab to the FLASHForward interaction point is achieved with a vacuum beam-line that connects the compressor to the electron beam-line. A sketch of the beam-line is shown in Figure 3.4. Multiple periscopes are used to transport the compressed pulse to the ground floor and finally to the $1.5\,\mathrm{m}$ height of the electron beam-line. A staggered approach is used to achieve this, with the first periscope (M2 and M3) transporting the laser pulse down to a height of $3\,\mathrm{m}$. A second chamber (M4-M6) then reduces the height to a further $2.5\,\mathrm{m}$ and more crucially brings it parallel to the electron beam-line.

After this $50\,\mathrm{m}$, a half-inch pick-off mirror is positioned in the path of the beam in order to split the pulse in two. The pick-off mirror is mounted on a motorised stage such that it may be driven in to produce a half-inch beam with partial transmission of the remainder of the non-reflected energy or completely driven out for full transmission. A CAD model of the pick-off mirror is shown in Figure 3.6. The transmission of the pick-off is estimated via simulations to be about $93.5\,\%$. In Figure 3.5, the effect of this mirror on the longitudinal intensity of the laser pulse is explored. A laser pulse with a pulse length of $50\,\mathrm{fs}$ and energy of $25\,\mathrm{mJ}$ was focused over a length of $18\,\mathrm{m}$. The intensity at focus was calculated using Fourier optics which will be outlined in Chapter 4. To simulate the pick-off mirror, a mask diameter of $6.35\,\mathrm{mm}$ was applied to the centre of the beam in its near-field order to set the intensity here to zero. The estimated maximum intensity in focus drops from $5.78 \times 10^{14}\,\mathrm{W\,cm^{-2}}$ in the case of full transmission to $5.14 \times 10^{14}\,\mathrm{W\,cm^{-2}}$, a decrease of $11.1\,\%$.

After the pick-off mirror (BS1 in Figure 3.4), the two beam-lines may be considered separate entities, referred to as the transverse and longitudinal beam-lines. The transmitted portion of the beam enters into a periscope where it is brought down to the height of the electron beam at $1.5\,\mathrm{m}$. After the periscope, it is focused by a pair of spherical mirrors and coupled into the electron beam-line. The spherical mirrors each have a focal length of $750\,\mathrm{mm}$ and are placed $1.56\,\mathrm{m}$ apart from eachother, resulting in a total effective focal length of $18\,\mathrm{m}$. The first mirror is mounted on a linear motor, allowing for adjustments to be made to the total focal length, ensuring the correct positioning of the focal plane. The three aforementioned periscopes are all 90° periscopes which rotate the polarisation of the laser. The laser pulse exits the compressor horizontally polarised and therefore the longitudinal pulse arrives at the

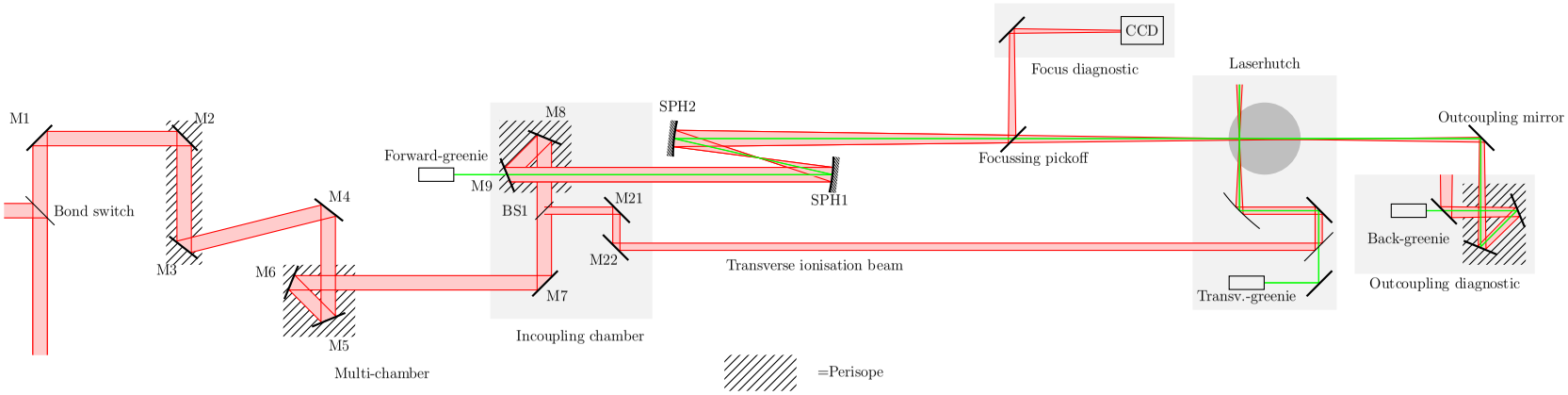

Figure 3.4: A sketch of the FLASHForward laser beam-line which transports the pulse from the laser lab to the target chamber. Figure by K. Põder

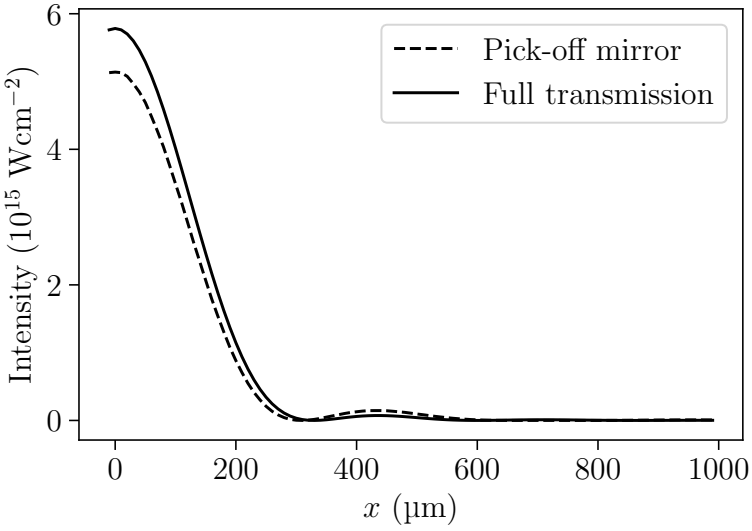

Figure 3.5: A simulation of the effect of the pick-off mirror on the transmitted beam at focus. The peak intensity in focus is decreased by 11 %, but the shape of the focus is not significantly impacted by the presence of the pick-off mirror.

plasma chamber with vertical polarisation.

The reflected pulse is transported in a second beam-line parallel to the electron beam-line. It arrives at the plasma chamber where it may be used for either transverse diagnostics and/or plasma shaping.

3.3.2 Longitudinal laser profile

The longitudinal laser was reflected from an OTR screen placed upstream of the capillary and imaged at the plane of the OTR screen[2]. The profile is plotted in Figure 3.7, where a number of features are present in addition to the central laser spot. The use of two spherical mirrors at an offset from one another will introduce some intrinsic astigmatism alongside other aberrations to spatial phase profile of the beam [95]. However the intensity and transverse profile of this focus was not assumed to be a critical factor as ionisation of argon was achieved with relative ease.

[2]The full set-up at the plasma chamber will be discussed in Section 3.4

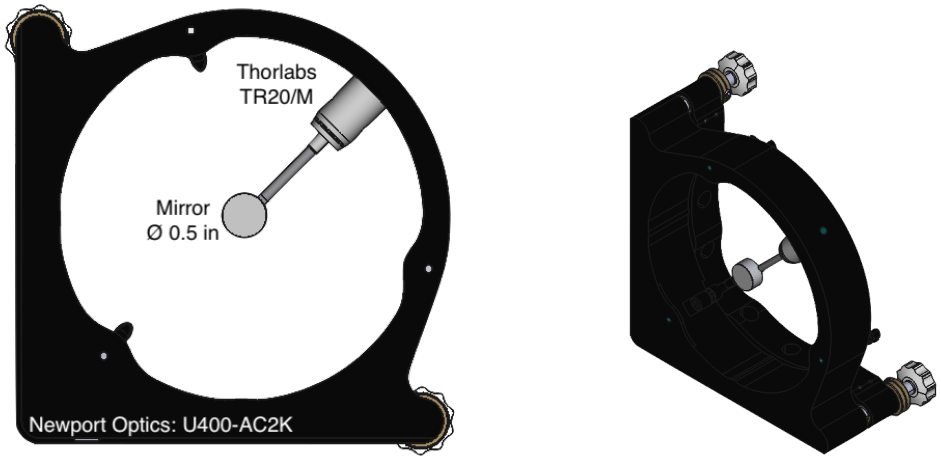

Figure 3.6: A model of the pick-off mirror used to generate the transverse laser pulse. In subfigure (a) labels have been added to selected components for clarity

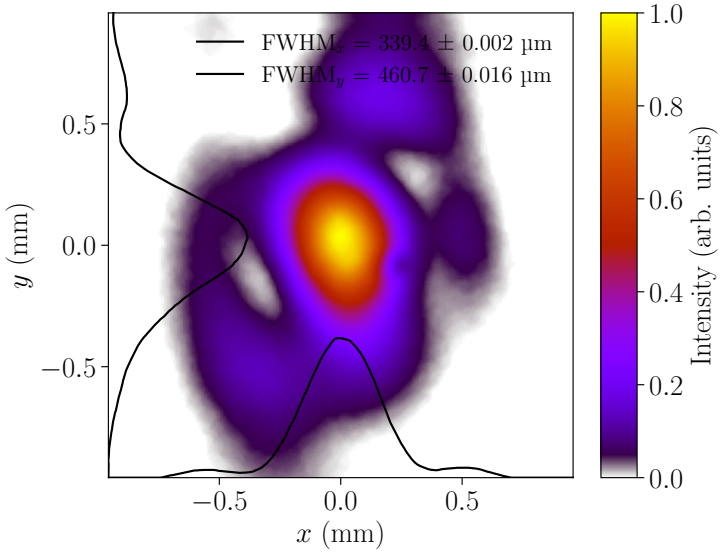

Figure 3.7: The longitudinal laser focus as imaged on the Upsteam OTR camera. The has been normalised to the peak of the signal.

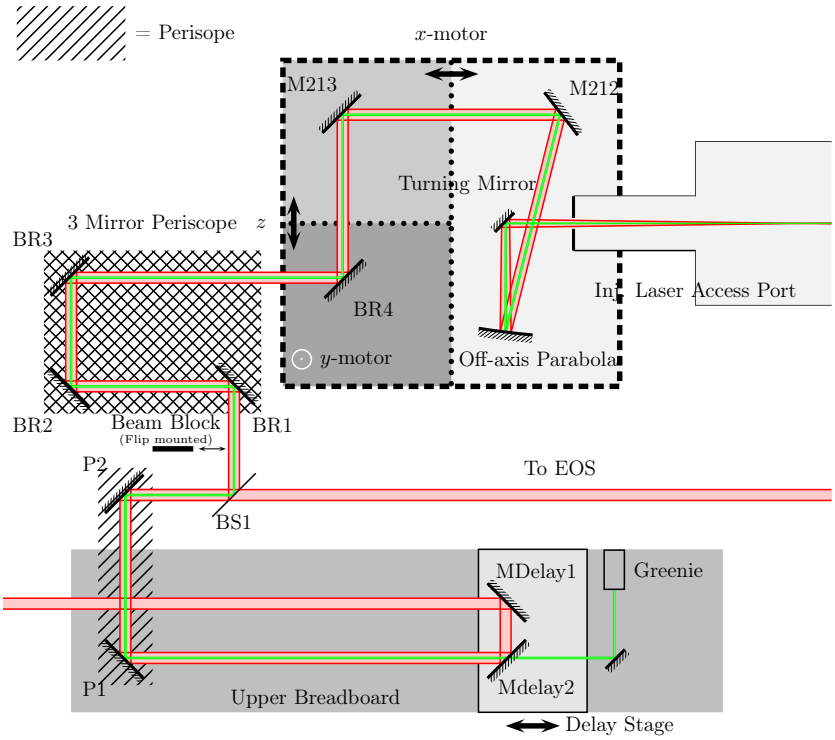

Figure 3.8: A schematic drawing of the optical set up around the plasma chamber. The green laser was used for visual alignment of the system, while the beam block could be inserted into the path of the laser to prevent transmission of the laser into the plasma chamber.

3.3.3 Transverse focusing

The transverse laser was focused by a gold coated, 2-inch diameter, 15° off-axis parabola (OAP), with an effective focal length (EFL) of 646 mm or f/51[3]. A sketch of the setup is shown in Figure 3.8. The pulse exits the laser beam-line at a height of 2 m. A delay stage (MDelay1 & MDelay2) is placed directly behind the exit of the beam-line in order to control the relative time of arrival between the two beams. Following the delay stage, the beam enters another periscope which reduces its height down to 20 cm above a breadboard of height 1.2 m. Here a 90:10 beamsplitter (BS1) further separates the pulse into the Injection and EOS arms.

[3]Edmund Optics Part No. 35-599

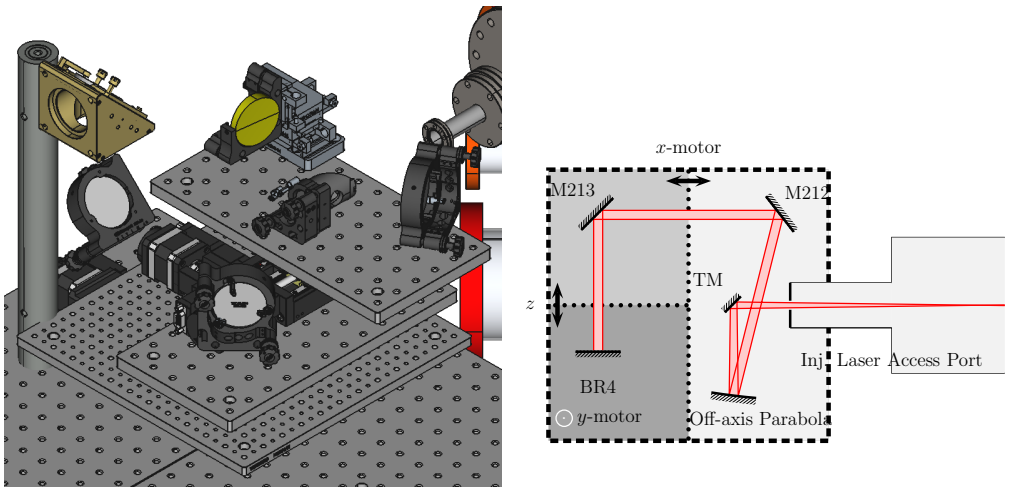

(a) (b)

Figure 3.9: Design of the transverse-focusing assembly (a) 3D view, (b) Schematic View.

The injection arm begins with a 3-Mirror-Periscope (3MP), which transports the beam onto the Transverse Focusing Assembly (TFA). A detailed view of the TFA is shown in Figure 3.9. The 3MP elevates the beam above the TFA which is mounted on an elevation stage. The motors are configured such that the linear motion occurs along the axis of optical propagation, allowing the free movement of the focus in all three spatial dimensions without significantly altering the alignment onto the OAP. The alignment onto the OAP could be adjusted using the M213 and M212 mirrors, while the OAP and the turning mirror (TM) were used to steer the exiting beam onto the correct axis.

Due to the placement of the TFA outside of the plasma chamber, thereby requiring the transmission of the pulse through a window into the chamber, it was necessary to minimise the effects of non-linear phases shift of the pulse due to the transmission of a laser pulse through a medium such as glass or even air. The extent of these effects is quantified in the B Integral, which is given by Equation 3.1,

$$B = \int_0^d I \cdot n_2 \mathrm{d}z, \tag{3.1}$$

where d is the thickness of the medium along the propagation axis of the laser pulse z, I is the intensity of the laser and n_2 is the non-linear refractive index of the medium. The B integral therefore scales with the intensity of the pulse and the thickness of the medium. Thus, in or-

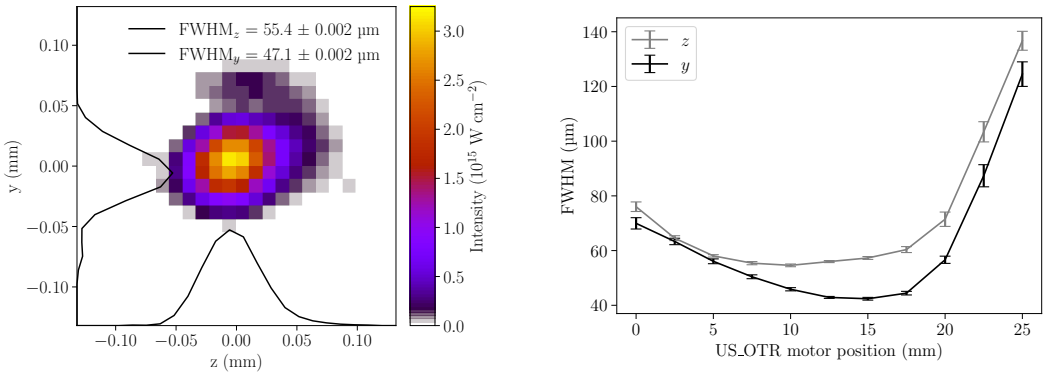

(a) (b)

Figure 3.10: (a) The transverse laser focus as imaged on the upstream OTR camera. The image shown is a single shot representative of the focal-spot at a stage position of 10 mm. The intensity is calculated for a laser pulse of 5 mJ and pulse length of 35 fs. (b) The FWHM spot size as a function of the position of the US_OTR camera along the laser propagation axis. Each point represents a series of 10 images taken at each stage position.

der to avoid such effects, both the laser intensity of the laser at the window and the thickness of the window itself should be minimised. The former is possible by placing the the window as close to the OAP as possible along its focal plane. In this case an additional 1-inch diameter turning mirror (TM) was placed after the OAP. The window thickness was minimised by reducing the original CF130 flange down to CF16 with a series of additional piping components, allowing the use of a 1.5 mm-thick fused-silica window. A further reduction in B integral is in other cases feasible by selecting a medium with a lower value of n_2, such as calcium fluoride with a value of 0.43×10^{-13} esu compared to fused silica's 0.85×10^{-13} esu [96]. However the material strength in withstanding vacuum forces will not be the same across all materials, thus requiring increased window thickness for structurally weaker media. In this case, the increased strength of fused silica allows for a thinner window than would be achievable with glasses of lower n_2 [97]. These mitigation strategies were all used to keep the B Integral below an estimated value of 2, which while higher than the ideal value of 1 or lower, should be sufficient.

The focal-spot produced by this set up is plotted in Figure 3.10a. The intensity has been calculated using the raw spot profile and Equation 4.1. The FWHM spot size of the focal-spot over a range of 25 mm is plotted in Figure 3.10b. The FWHM reached a minimum of (54.9 ± 1.4) µm in z and (52.2 ± 1.1) µm in y at a stage position of 10 mm. To characterise the spot, ten images were taken at each stage position and a Gaussian profile fitted to each im-

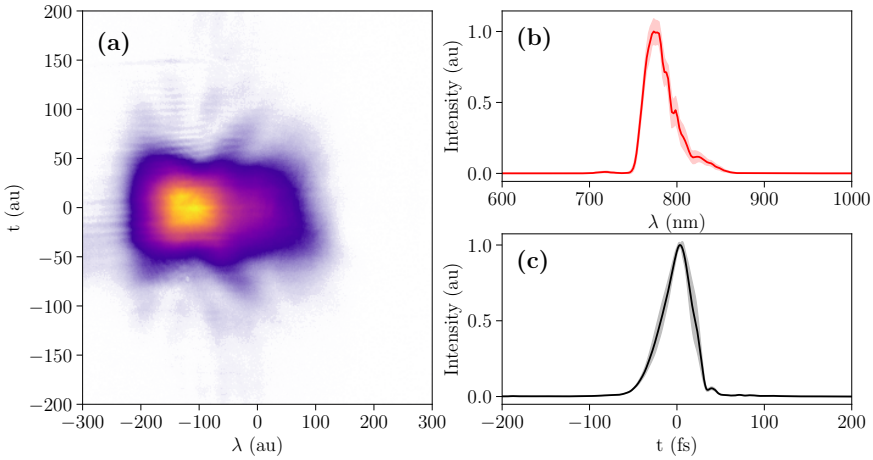

Figure 3.11: Temporal profiling of the transverse laser as measured after the BS1 beamsplitter. (a) A reprensentative raw FROG trace, (b) The mean spectral intensity and (c) The mean temporal profile. The shaded regions in subplots (a) and (b) represent the standard error on the mean.

age. The FWHM values of these Gaussian profiles are plotted in Figure 3.10b, where the plotted point represents the mean FWHM and the error bar corresponds to the standard deviation, however the resolution of the imaging system at $11\,\mu\mathrm{m/pixel}$ limits the conclusions which can be drawn from this dataset and limit the full characterisation of the focal-spot. The non uniform profile of the focus is evident, but the origin of these non-uniformities is difficult to investigate with such a low resolution compared to the size of the spot. The resolution also impeded the further optimisation of the spot. Focal-spot optimisation is a stepwise process and the low resolution made any possible improvements in the spot difficult to discern. A dedicated high-resolution transverse laser-focus diagnostic was not implemented at the time of the experiment. The positioning jitter of the spot was $(4.035 \pm 0.003)\,\mu\mathrm{m}$ in the y direction and $(3.393 \pm 0.001)\,\mu\mathrm{m}$ in the z direction as seen in Figure 3.12. The ratio of the peak intensities between the measured beam profile and its simulated counterpart was 2:3.

The temporal profile of the transverse laser was measured using the GRENOUILLE (Grating-eliminated no-nonsense observation of ultrafast incident laser light e-fields) device [98] placed downstream of the BS1 beam-splitter, which was removed for the purposes of this measurement. The pulse could be compressed to a minimum value of $(35 \pm 5)\,\mathrm{fs}$ as seen in the trace plotted in Figure 3.11. A full comparison between the focal-spot in Figure 3.10 and the simulated spot from Chapter 4 can be found in Appendix C.

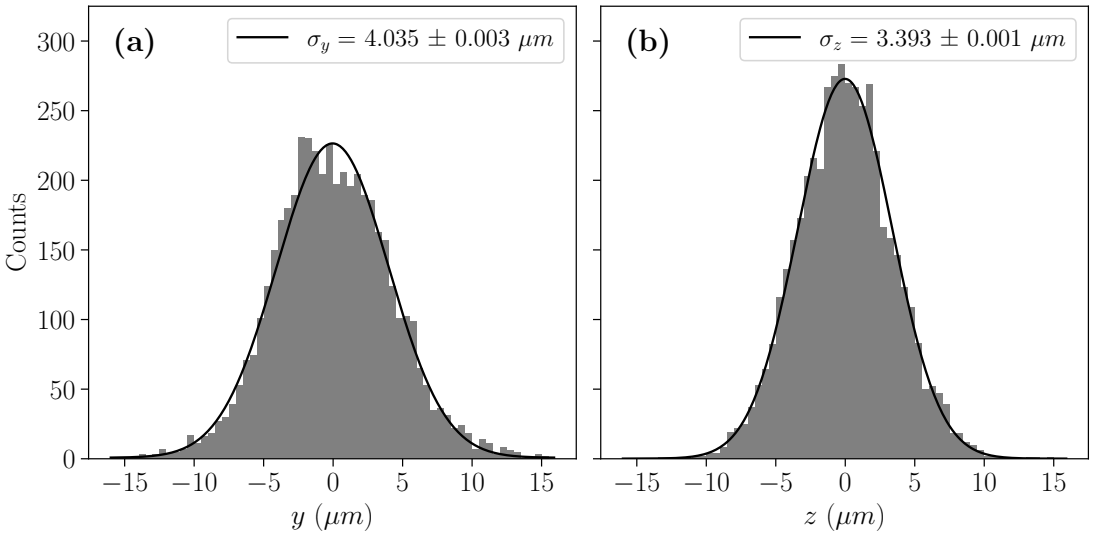

Figure 3.12: Histograms demonstrating the positional jitter of the transverse laser in the y (a) and z (b) planes. The histograms were fitted with Gaussian functions.

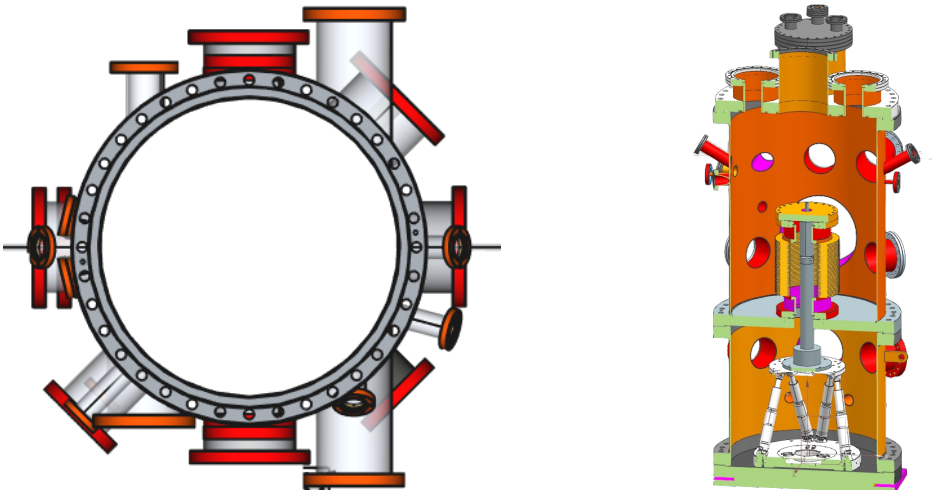

(a) (b)

Figure 3.13: (a) Top and (b) side sliced view of the target chamber

3.4 FLASHForward Target Chamber

Central to the FLASHForward project is the Target Chamber. The chamber was designed to allow for a high degree of flexibility in the experimental program. Top and central slices of the target chamber are shown in Figure 3.13 (a) and (b), respectively. The chamber has multiple viewports (nine at the height of the electron beam and three overhead) which allow access for imaging diagnostics and laser beams.

In order to preserve the high quality and prevent contaminants from entering the $\mathcal{O}(10^{-9})$ mbar FLASH vacuum system, no motorised parts were permitted to be installed in the target chamber. Therefore, in order to provide the necessary motion for the plasma source (Sec. 3.4.1) a hexapod was placed in a secondary chamber, separated by a bellow from the main chamber. A rotary feedthrough ensures that the full 6D movement of the hexapod is applied correctly and consistently to the plasma source.

3.4.1 Plasma source

The plasma source at FLASHForward is contained within the Target Chamber. The differentially pumped chamber allows the plasma to be sourced from either a low-pressure gas-filled chamber ($\mathcal{O}(10^{-2})$ mbar) or a capillary target. These may either be filled with argon, helium,

or a mixture of the two. For safety reasons, operation with other gas species such as Hydrogen was not implemented at the time of writing.

These gases may be mixed in a backing chamber placed outside the target chamber. A series of pipes then connects the backing volume to a target placed inside the chamber. The target typically consists of two sapphire plates with machined channels sandwiched together inside a holder fabricated from PEEK[4] to form a capillary. The capillaries and targets are designed specifically for each experimental run (6 months - 1 year). An example target and the holder are shown in Figure ??. The plasma itself may be ignited either through the passage of a high-voltage discharge current through the capillary known as "Discharge Ionisation" and / or the passage of a high-intensity laser through the capillary known as "Laser Ionisation". In discharge ionisation, it is difficult to selectively ionise gas species such that the dopant species is available for later ionisation by a transverse laser for LT-DDI schemes. Therefore laser ionisation will form the primary focus of this work.

The set up in and around the plasma chamber is shown in Figure 3.14. Two breadboards were placed on either side of the plasma chamber, one between the tunnel wall and the plasma chamber and one on the side closer to FLASH2. These diagnostic stations are referred to as the 'Wall Side' and 'FLASH2 side'. The plasma target is a sapphire capillary which is mounted on a base plate inside the plasma chamber.

3.4.2 Plasma target and base plate

The plasma target used in this experiment is shown in Figure 3.15. The target consists of a holder for two capillaries with lengths of $50\,\mathrm{mm}$ and $195\,\mathrm{mm}$. The capillaries consist of two $4\,\mathrm{mm}$-thick sapphire plates with a laser-machined channel that are sandwiched together to form a $1.5\,\mathrm{mm}$-diameter central channel. Two $0.3\,\mathrm{mm}$-diameter holes are located $20\,\mathrm{mm}$ downstream of the entrance in order to provide windowless access for the transverse laser pulse. Also present on the base-plate are diagnostics including two Optical Transition Radiation (OTR) screens, the Electro-Optical Sampling (EOS) mirrors and a Gallium Phosphide crystal. The OTR screens were used to image the electron beam and longitudinal laser, while the EOS system was designed to allow for the precise measurements of the time of arrival of

[4] Polyether ether ketone

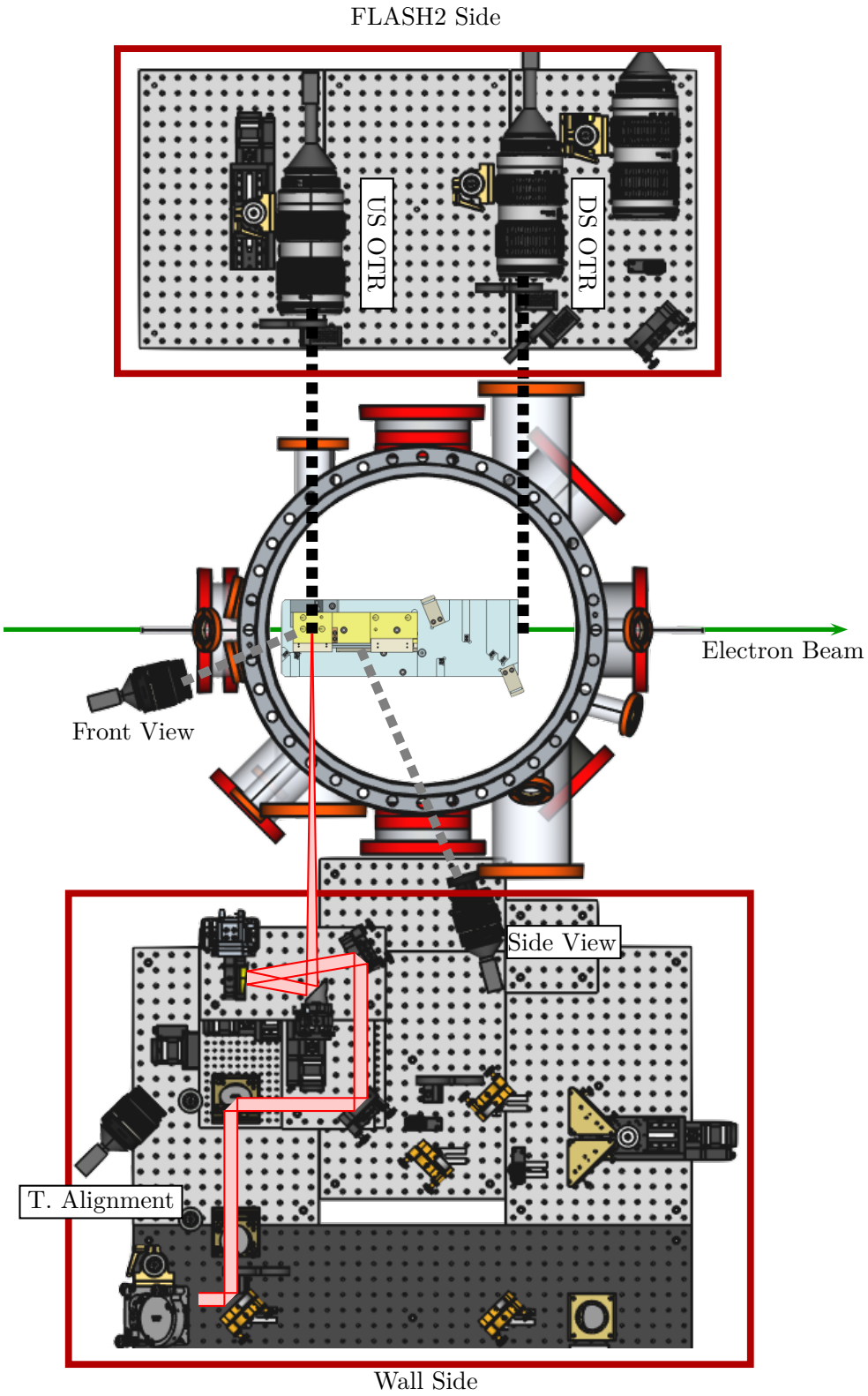

Figure 3.14: The plasma chamber including all diagnostics

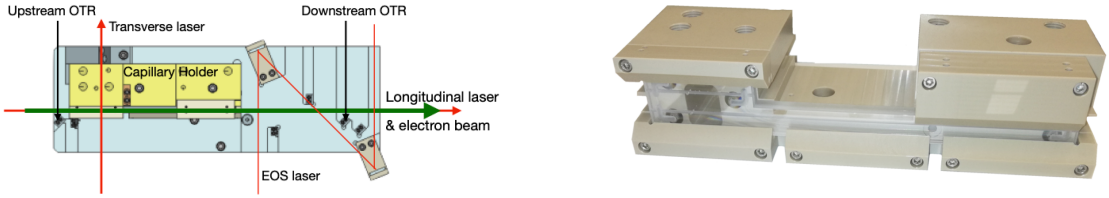

(a) (b)

Figure 3.15: (a)The plasma base plate. The paths of the electron beam (green arrow) and longitudinal laser (red arrow) as well as the transverse laser (red arrow) are indicated. (b) The capillary holder is constructed out of PEEK. The sapphire plates (transparent) containing the capillaries are also visible. The upper capillary is 50 mm in length and the lower capillary is 195 mm long.

the electron beam [99] [5].

The base-plate was mounted to the hexapod in the lower plasma chamber via the rotational feed through. The lower chamber formed a separate vacuum system from the high-quality machine vacuum and is connected to the main chamber with bellows. To prevent collision with the walls of the chamber and damage to the bellows, the hexapod could be moved though a range of up to $\pm$ 25 mm linearly and rotated up to an angle of 5°. The range of motion was sufficient, that the hexapod and base plate could be completely removed from the path of both lasers and the electron beam.

3.4.3 Diagnostic cameras

The experiments at the plasma chamber were monitored with a series of cameras placed around the chamber. A list of the cameras and their purposes relevant to this work is tabulated in Table 3.1. The two OTR screens were imaged with the upstream (US) and downstream (DS) OTR cameras, which were also used to characterise the two laser-pulse profiles and overlap them with the electron beam. Transmission of the longitudinal laser through the capillary was verified using the relative intensity of the laser on the End-Of-Beam (EOB) camera. This was also aided by the Front-View camera which imaged the front-facing electrode of the capillary to ensure maximum coupling of the laser into the capillary. The arrangement of these diagnostics (excluding the Top-View and EOB) is shown in Figure 3.14.

[5] At the time of the experimental study the EOS system had not been fully commissioned, so it will not feature substantially in this work.

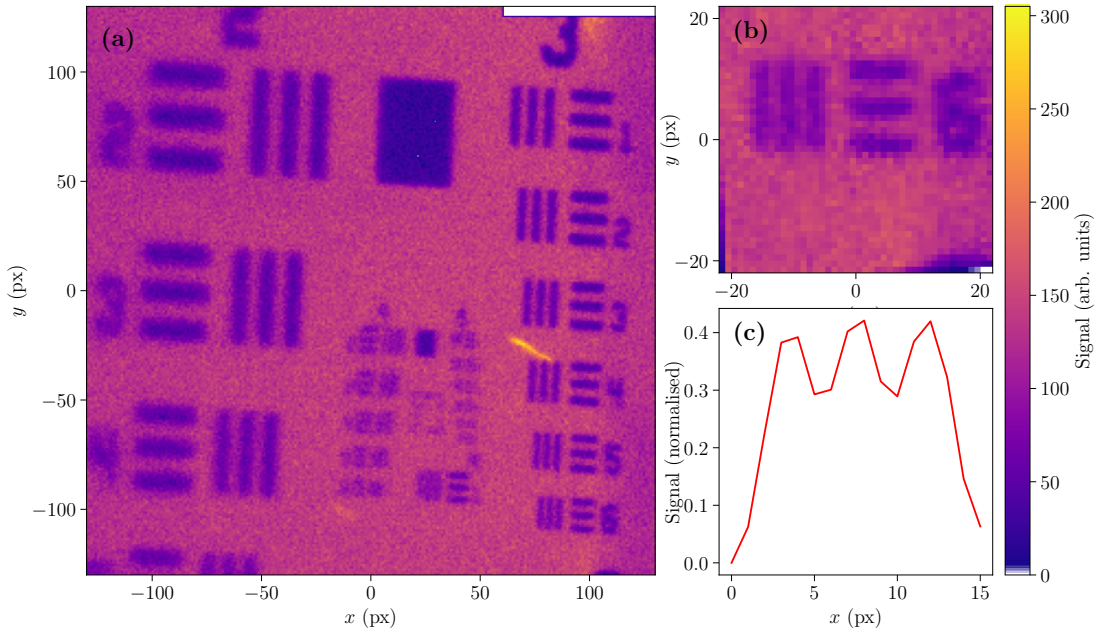

Figure 3.16: Calibration of the upstream OTR screen station with a US Airforce target (a) the raw image data, (b) the data containing the 6th element in group 3 where each line is exactly 35.08 μm thick [100]. (c) The integrated signal across the vertical lines in (b). The total signal area is 16 pixels wide, yielding a resolution of 10.96 μm/pixel

The upstream OTR screen (US_OTR) was offset inside its holder as shown in Figure 3.17. This was intentional for the purposes of laser alignment. The offset screen left a gap large enough for the longitudinal laser and electron beam to pass through the holder and be reflected from the downstream screen. Additionally, the transverse laser could also be transmitted through the gap and be imaged at the same time as the longitudinal laser and/or the electron beam. The screen was imaged with a Basler ac A1300-22gm CCD camera and Canon EF 100-400mm objective. The spatial calibration of the screen was carried out by imaging a USAF (United States Air Force) resolution test target, visible in Figure 3.17. The image of the target and the subsequent calibration of the imaging system is detailed in Figure 3.16 yielding a final calibration of 10.96 μm/pixel.

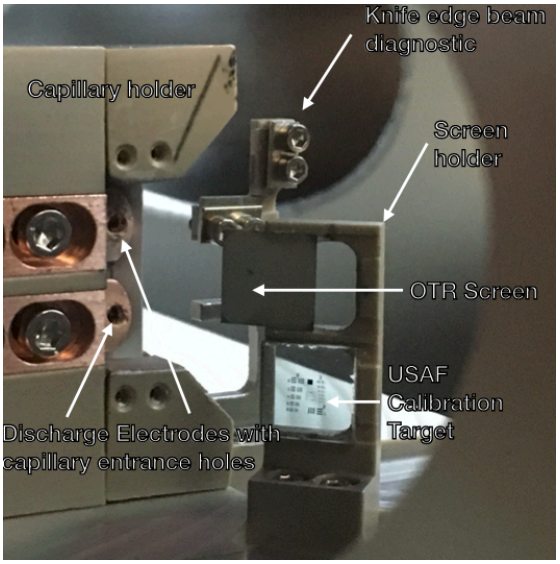

Figure 3.17: The upstream OTR screen (grey-centre) positioned offset in the holder (PEAK, light brown). The calibration screen below shows the centre or ordinary position in the holder

Camera Name	Type	function
US OTR	Basler ac A1300-22gm	Three-beam spatial overlap Laser-spot characterisation
DS OTR	Basler ac A1300-22gm	Beam Overlap Laser-spot characterisation
Top View	Basler ac A640-120gm	Laser to E-beam Timing Ionisation monitoring
Side View	Basler ac A2040-25gm NIR	Plasma Observation Laser alignment
Front View End of Beam	Basler ac A640-120gm	Laser alignment through capillary Laser transmission
Transverse Alignment	Basler ac A1300-22gm	Alignment of transverse laser

Table 3.1: List of diagnostic cameras and their functions relevant to this work.

3.4.4 Transverse plasma

The intensity profile described in the previous section (Sec. 3.3.3) was used to calculate the expected ionisation ratios for the the gas mixture in the capillary. The ratio of the density between helium and argon was limited to 2-1 to avoid saturating the differential pumping system while having sufficient background species to form a plasma. Therefore the maximum possible filament height was four times the background plasma density, n_0. This was based on the assumption that the longitudinal laser is of sufficiently low intensity that it is only able to ionise the first level of argon, while the second and third levels plus the first level of helium were solely ionised by the transverse laser. Due to the low camera resolution, the data from Figure 3.10a was interpolated by a factor of 20 prior to calculating the plasma density in order to increase the number of data points. As will be shown later, this was necessary for input into Particle-in-Cell simulations of the plasma. The interpolated images for both the laser focus and the resulting plasma profile are seen in Figure 3.18.

The ionisation of the transverse laser was monitored and studied with the top-view camera while the chamber was pressurised to $\sim 0.02\ \mathrm{mbar}$ with either pure argon, in order to ionise with both lasers, or helium. Light from the recombination of plasma electrons is emitted from the plasma and well imaged by the camera as shown for the argon plasma in Figure 3.19, for laser attenuator settings between 10 and 60 %. The signal was observed to move upstream (to the LHS of the frame) and dim significantly over the course of the scan as the laser energy increased. The former observation indicates the laser pulse may be experiencing self focusing in the window of the plasma chamber [101], which shifts the focus of the laser upstream. The latter finding indicates the onset of non-linear phase shifts, such as self-phase modulation [102] as the pulse passes through the window or the stretching of the laser pulse due to dispersion which alter the temporal profile of the laser, often resulting in an increased pulse length, a decreased on-target intensity and therefore reduced ionising capability.

3.5 Post-plasma beam-line and electron spectrometer

The post-target-chamber beam-line consists of the FLF-DIAG (Diagnostic) and FLF-UND (Undulator) sections[6]. The DIAG section is dominated by the electron spectrometer, whereas

[6]The original plans for the FLASHForward experiment included a subsequent phase in which undulators would be installed to explore and demonstrate the lasing properties of plasma-accelerated electron beams

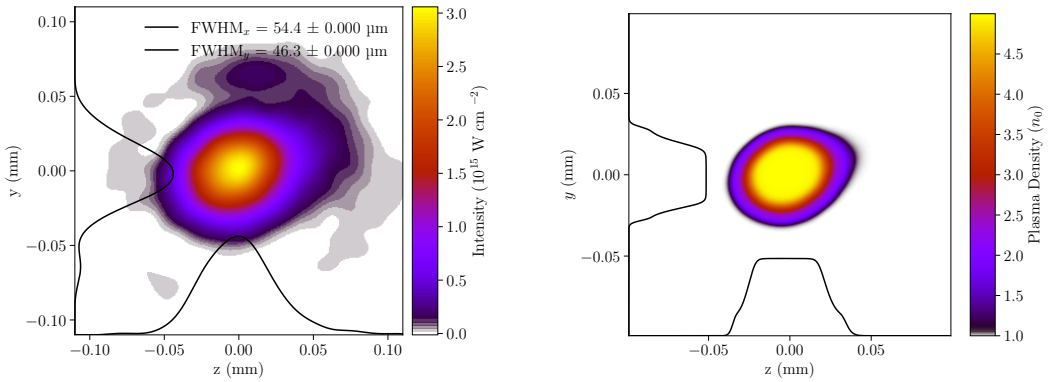

Figure 3.18: (a) The interpolated laser focus using the data from Figure 3.10a and interpolating it by a factor of 20 to increase the number of data points for the density calculation. (b) The resulting plasma profile as calculated using the ADK formula

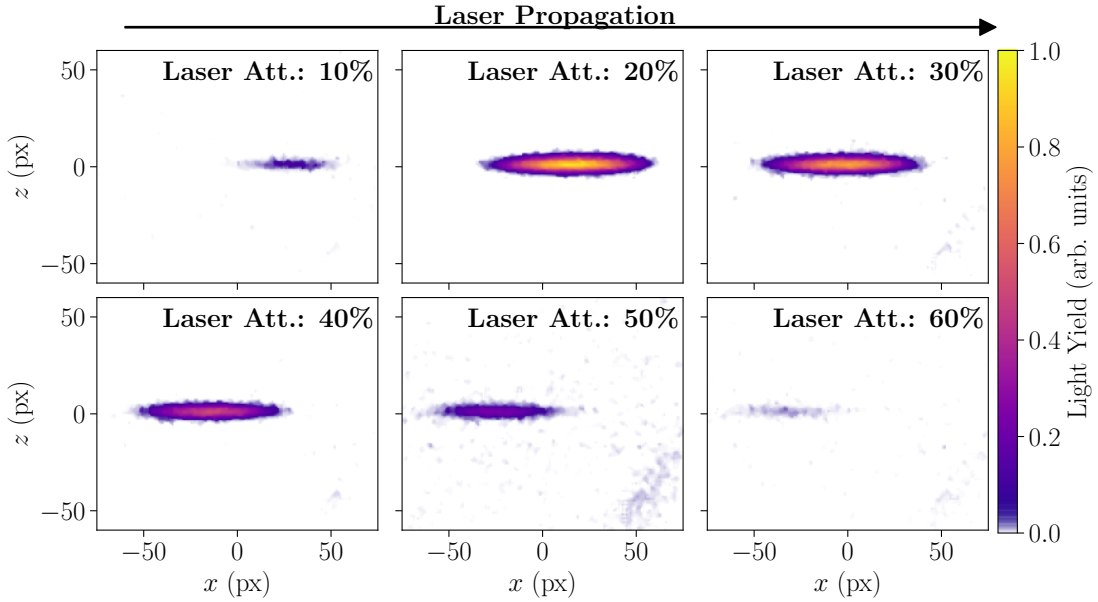

Figure 3.19: The transverse plasma as seen on the top view camera for a range of laser energies. The calibration factor at the image plane was not measured and therefore the axes have not been scaled.

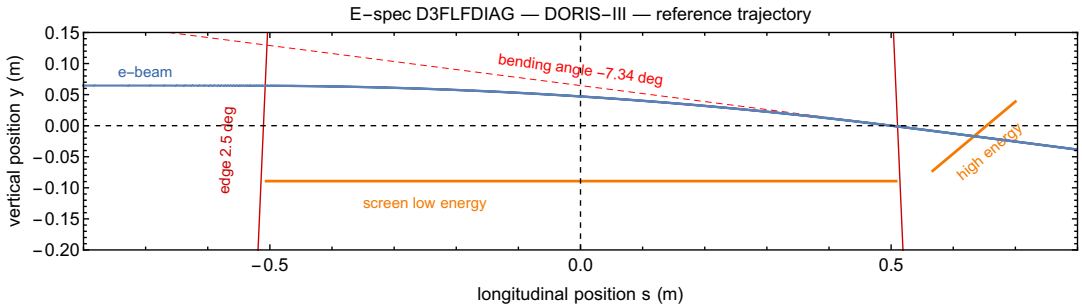

Figure 3.20: Trajectory of electron beams inside the electron spectrometer magnet. The nominal path of the electron beam in shown in blue. The spectrometer includes two positions for diagnostic screens. A low energy screen is placed at the bottom of the chamber, while high-energy electrons are imaged on the high energy screen, placed at 45 degrees. Figure courtesy of S. Wesch

the UND section is used to transport the beam into the FLF-XTDS section. As its name may suggest, this section consists of an X-Band Transverse Deflecting Structure ("PolariX-TDS") [103]. The X-TDS permits the longitudinal phase space of electron beams in FLASH-Forward to be fully characterised. Witness beams with energies up to 2.5 GeV may be transported and characterised by the post-plasma beam-line.

Immediately downstream of the target chamber, five XQA (X-FEL Quadrupole Type A) magnets capture and focus the beam(s) onto the spectrometer screens. The electron spectrometer ("Espec") is constructed around a DORIS-III dipole magnet which was originally used at the DORIS accelerator on the DESY Campus. This consists of the 1 m long dipole magnet itself and a specially designed chamber, enclosed within the magnet that supports the installation of LANEX screens to diagnose the beams. The arrangement of these screens is shown in Figure 3.20. The high-energy beams are captured by the "high energy" screen, while low-energy witness beams and/or depleted drivers may be diagnosed on the 1 m-long "low-energy" screen. The screens are imaged by a series of cameras, whos positioning, imaging properties and number may be customised to suit the requirements of each individual experiment.

3.5.1 Electron beam parameters

The electron beam was characterised at the X-TDS; the reconstructed longitudinal current profile is shown in Figure 3.21. The (789.0 ± 4.1) pC beam was compressed to an RMS bunch length of 186.8 fs, resulting in a peak current of 2.11 kA and an energy of 1116 MeV.

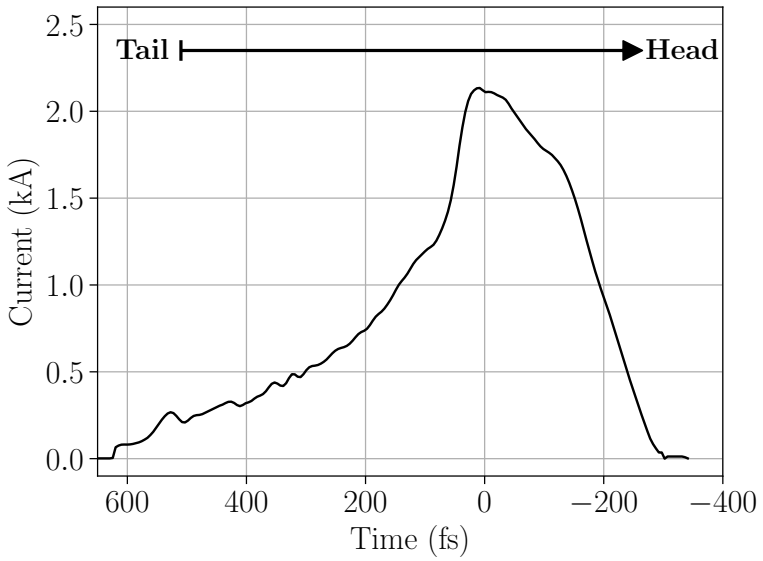

Figure 3.21: The longitudinal current profile of the driving electron beam as reconstructed by the X-TDS

The normalised emittances were 14.04 ± 1.00 and $5.32 \pm 0.03\,\mu\mathrm{m}$ in the x and y planes respectively. Further transverse beam focusing properties were determined using the centroid jitter of the beams on the BPMs upstream and downstream of the plasma chamber [104]. The beam was focused to a spot size of $19.6\,\mu\mathrm{m} \times 17.1\,\mu\mathrm{m}$ in x and y respectively at its waist and $24.5\,\mu\mathrm{m} \times 17.1\,\mu\mathrm{m}$ at the entrance of the capillary. The beta functions were determined to be 60 and 120 mm. The position jitter at the location of the transverse hole in the capillary was estimated to be $\pm 1.01\,\mu\mathrm{m}$ in x and $\pm 1.43\,\mu\mathrm{m}$ in y.

The interaction of this beam with a plasma was investigated using a series of simulations. In these simulations, the beam was incident into a 50 mm long plasma profile. The density of this plasma was increased incrementally between 0.5 and $3.0 \times 10^{16}\,\mathrm{cm}^{-3}$. The minimum energy, E_{min} of the driver was calculated for each density using a threshold method, which was then subtracted from the initial energy $E_0 = (1116 \pm 5)\,\mathrm{MeV}$ to yield the energy loss ΔE. The same analysis was then applied to the drive beam as measured on the ESPEC during the experiment. Experimentally the energy loss was determined to be $(139.1 \pm 12.0)\,\mathrm{MeV}$. In Figure 3.22, the simulated energy loss is plotted as a function of density. The data was interpolated and then used to calculate the density which would result in the experimental value. From this energy loss, the plasma density was determined to be $1.42^{+0.37}_{-0.29} \times 10^{16}$ cm^{-3} averaged over a flat-top plasma which was assumed, in these simulations to be 50 mm

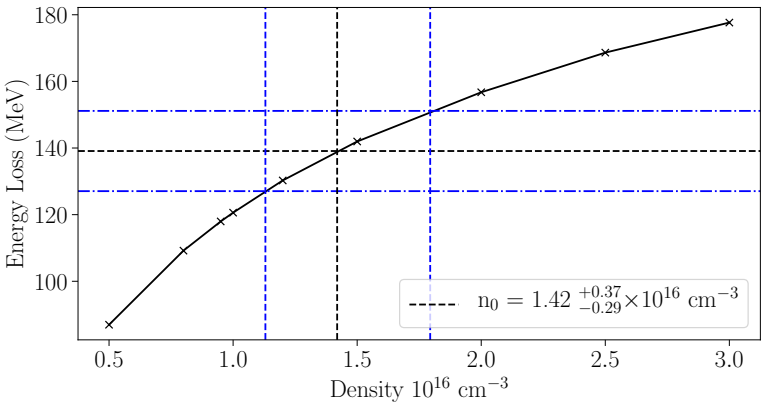

Figure 3.22: The plasma density evaluation using driver energy loss with a comparison between the experimentally determined value of the energy loss at (139.1 ± 12.0) MeV and a set of PIC simulations in which the density was scanned between 0.5 and 3.0×10^{16} cm^{-3}. The black dotted lines indicate the nominal value of energy loss and the corresponding plasma density while the blue dotted lines indicate the error of $\pm$ 12 MeV on the value of the experimental energy loss and the corresponding errors on the plasma density

long. The errors on this density value were calculated by determining the plasma density that would result in an energy loss of 127 and 151 MeV, yielding densities of 1.13×10^{16} and 1.79×10^{16} cm^{-3}. Alternative methods for direct plasma-density measurement, such as longitudinal interferometry or spectrometry [105] were considered, but ultimately determined to be unsuitable due to the relatively low plasma density and the inability to operate with hydrogen at the time of the experimental run.

4

Simulations of density down-ramp injection at FLASHForward

This chapter studies the feasibility of internal injection at FLASHForward based on the laser-triggered density-down-ramp scheme introduced in Section 4.1. Simulations were carried out using the OSIRIS PIC code and based around experimentally feasible plasma densities and shapes as well as the beam parameters of the FLASH electron beam; these are detailed in Section 4.2. The first investigations are centred around the effect of the secondary-laser (Injection laser from here on) spot size. Following on from these studies the effects of the gas mixture selection and the effect of miss-alignments on the system are investigated.

This chapter first introduces the methods used to simulate injection and then explores the parameter space available at FLASHForward and draws conclusions about which range is likely to prove the most conducive to demonstrating injection in the experimental run. Further discussion of the physics of of density-down-ramp injection can be found in [106] and [52] and have been summarised in Section 2.7.1.

4.1 Simulation of density down-ramp injection

To study the feasibility of density-down-ramp injection at FLASHForward, simulations were performed using particle-in-cell (PIC) simulations to model the highly non-linear physics described in Section 2.6.

4.1.1 Pre-PIC Simulation Procedure

The methods detailed in Section 2.4 are fully implemented by modern PIC codes. However, to accurately model the physics of a laser-pulse, the time step used must be small enough to resolve the laser wavelength, dramatically increasing the computational time required for such simulations. The physics of laser propagation and ionisation is well understood and can be simulated without requiring high-performance computing (HPC) infrastructure and therefore were simulated prior to the PIC simulations. The use of HPC is typically required when simulating effects which are difficult to describe analytically, such as the interaction of an extremely intense laser pulse (intensities exceeding 10^{18} W cm^{-2}) with a plasma in LWFA. However in this work, a laser is only used for the ionisation of the plasma, which takes place at significantly lower intensities (10^{15} W cm^{-2}) and models of vacuum propagation were therefore assumed to be sufficient for the purposes of these studies. This section details these models of laser propagation and ionisation of multiple gas species.

4.1.2 Laser propagation

The first step was the modelling of the physics of laser propagation. In the simulation, the properties of the laser pulse were first initialised in the near-field domain, including the beam radius, pulse length and the total beam energy. The initial idealised profile may then be modified to include the effects of features such as an aperture, to reduce the size of the profile or to replicate a non-flat wavefront. A number of different spatial modes of the laser could be modelled including the aforementioned Gaussian or super-Gaussian profiles.

Once the electric field was initialised and initial modifications carried out, the field may then be propagated into the far-field of a lens or an off-axis parabola using numerical Fourier optics. This solves the Fresnel integral (Eq. 2.33) using an angular spectrum algorithm [67]. A

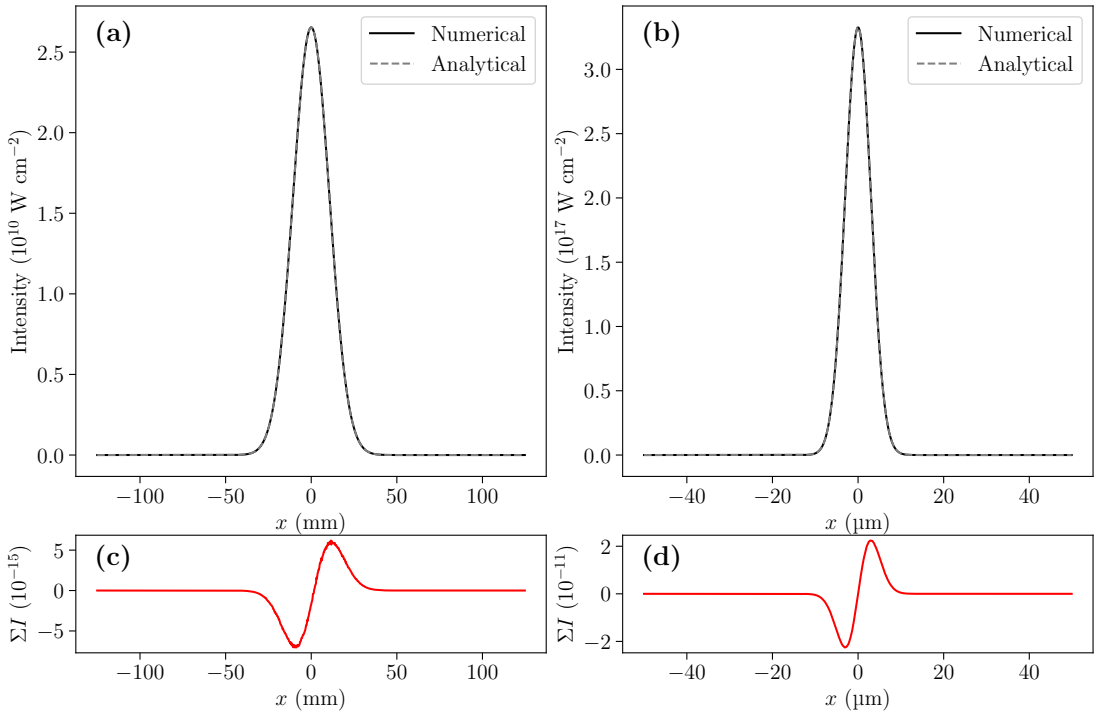

Figure 4.1: Benchmarking of the propagation algorithm and intensity calculation in both the near-field (a) & (c) and the far-field (b) & (d) of a 500 mm focusing optic. See text for details

full-numerical solver has the advantage that the focal region may be studied in more detailed than allowed for in other models. This includes the scanning of the focus through the focal region, which may be simulated by simply adjusting the far-field z position to before and after focus. These methods yield a numerical representation of the electric field, $E_{\text{num}}(x, y)$. The numerical intensity, of this field may be determined by squaring this value $I^{\text{num}}(x, y) \simeq |E^{\text{num}}(x, y)|^2$ which is then normalised in Equation 4.1,

$$I(x, y) = \frac{I^{\text{num}}(x, y)}{\sum_{x,y} I^{\text{num}}(x, y)} \frac{\mathcal{E}}{\sigma_t \sqrt{2\pi} \delta_x^2}, \tag{4.1}$$

where $\mathcal{E}$ is the laser pulse energy in joules, σ_t is the RMS pulse length of the laser pulse in the intensity domain and δ_x is the size of the grid.

In Figures 4.1 and 4.2, these methods are benchmarked against the analytical expressions for the propagation of a Gaussian laser-pulse with a wavelength of $800\,\text{nm}$, a FWHM diameter of $25\,\text{mm}$, a laser energy of $5\,\text{mJ}$ and a FWHM pulse length of $25\,\text{fs}$. The values for the size and pulse length are given for the intensity distribution, thus resulting in a σ_t of $10.625\,\text{fs}$ and a w_0 of $21.225\,\text{mm}$ when using the definitions discussed in Section 2.2.2.1. This laser was numerically propagated to the focus of $500\,\text{mm}$ focal-length lens. The beam waist in the focus of a Gaussian laser is given by

$$w_f = \frac{\lambda_0 f}{\pi w_0}, \tag{4.2}$$

which in this case yields a w_f of $6.0\,\mu\text{m}$. The central slice of the numerically calculated intensity profiles in the near and far-fields alongside the analytical expression Equation 2.27,

$$I(r, z) = I_0 \exp\left\{\left(-2\frac{r^2}{w(z)^2}\right)\right\}, \tag{4.3}$$

are plotted in subplots (a) and (b) of Figure 4.1 respectively. The analytical intensities have been calculated using the previously mentioned beam-waist values and peak intensities I_0 determined using Equation 2.32. There is excellent agreement between the curves. Subplots (c) and (d) highlight the agreement using a dimensionless error function ΣI given by

$$\Sigma I = \frac{I_{analytic}(x) - I_{num}(x)}{I_0}, \tag{4.4}$$

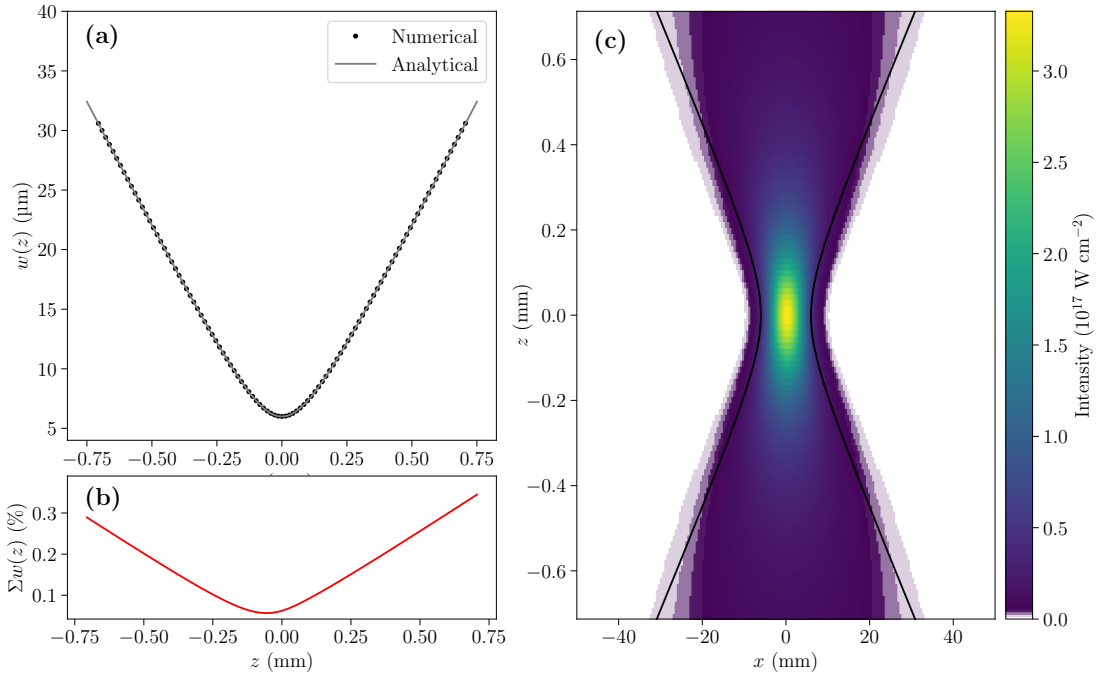

Figure 4.2: Further benchmarking of the propagation algorithm with a focal scan through the far-field of a 500 mm focusing optic.

The error values are on the order of 10^{-15} in the near-field and 10^{-10} in the far-field which represent negligible fractions of the peak intensity.

Figure 4.2 applies a similar analysis to the simulation of a scan through the focal region. Subplot (a) depicts the beam size as a function of z position where $z = 0\ mm$ is the focus. The analytical value of the spot size is determined by

$$w(z) = w_f \sqrt{1 + \left(\frac{z}{z_R}\right)^2}, \tag{4.5}$$

where z_r is the Rayleigh range which is $141.2\,\mu\text{m}$ for these values. The numerical values have been determined by fitting a gaussian to the intensity distribution at each step of the scan. There is, once again, excellent agreement between the numerical and analytical spot sizes, with a dimensionless error function given by

$$\Sigma w(z) = \frac{w_{analytic}(z) - w_{num}(z)}{w_f}, \tag{4.6}$$

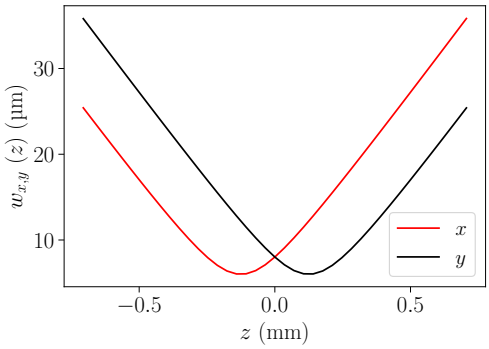

Figure 4.3: Demonstration of the effect of vertical astigmatism which shifts the foci in x & y. The focus is shifted up and downstream in the x & y planes respectively.

and plotted in Figure 4.2(b) remaining below the 0.5 percentage level. Figure 4.2(c) in the same figure shows the central lineouts for each step in Figure 4.2 (a). The black curves denote the theoretical values of w as a function of z position.

As the Fresnel integral includes the complex nature of the electric field, it is also possible to model the effect of applying phase terms to the field, such as the Zernike polynomials described in Section 2.2.4. Experimentally, the most common aberration is the form of astigmatism, which is described by the polynomials Z^2_{-2} and Z^2_2, which shift the x and y foci into different planes, as seen in Figure 4.3. Here a small amount of vertical astigmatism was added to the laser pulse and the pulse was propagated through focus over the same range. The calculated spot size $w\ (z)$ is plotted for both the x and y planes. The minimum is seen to be shifted by 0.1 mm from its location in Figure 4.2.

This was further explored using the 'defocus' Z^2_0 polynomial. In Appendix A.2, an analytical expression for the position of the focus d after a defocusing phase term of amplitude A has been applied to the laser was derived and linearised for small values of A

$$d = \frac{f}{1 - 4Af} \simeq f(1 + 4Af), \tag{4.7}$$

where f is the original focal length of the optic. In Figure 4.4, the amplitude of the defocusing term has been scanned between -5×10^{-4} and 5×10^{-4}, with the laser propagated through the same range. The position of the focus was determined by the position of the minimum w_z and is plotted as a function of the amplitude in Figure 4.4(a). Figure 4.4(b) depicts the absolute difference between the numerical focus position and the position predicted by

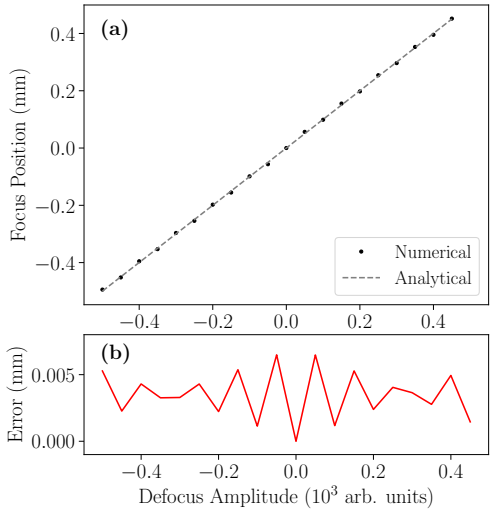

Figure 4.4: Demonstration of the effect of the defocusing Zernike polynomial Z_0^2 on the position of the focal spot. (a) The shift of the focus position with respect to the nominal position determined with the numerical simulation and an analytical expression. (b) The absolute difference between the analytical expression and the numerical result.

Equation 4.7, which is well below the $0.014\,\mathrm{mm}$ step-size of the focal spot scan. This demonstrates good agreement between the numerical and analytical values. These techniques could be used to arbitrarily shape the focus in order to optimise it for specific applications such as experiments like the one described in [107].

4.1.3 ADK Ionisation Simulation

The ionisation of a gas in the field of an intense laser pulse was simulated using the equations described in Section 2.4. The intensities calculated by the simulation code were used to calculate the electric field and then create a Gaussian profile based in time on the supplied pulse length. The ionisation rate was calculated over the length of the pulse and then integrated in time as shown in Equation 2.61.

The ionisation ratios as a function of intensity for a $50\,\mathrm{fs}$ FWHM laser pulse are plotted in Figure 4.5. The ratios were calculated for the ionisation species relevant to this work: Atomic Hydrogen (H - blue), the first three electrons of Argon (Ar, Ar^+ & Ar^{++} - Green) and Helium (He & He^+ - Red).

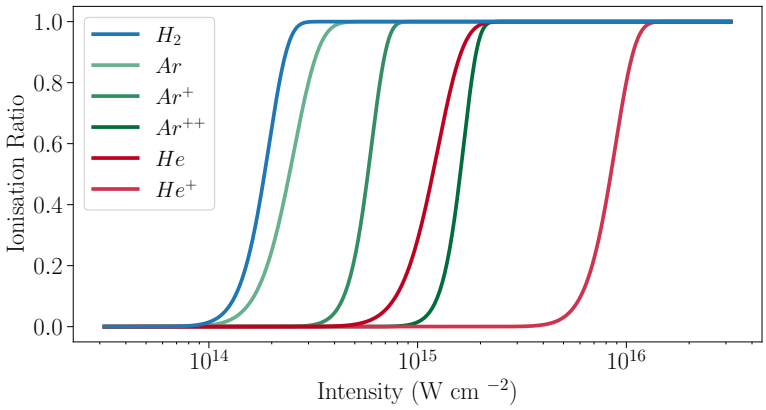

Figure 4.5: Ionisation ratios of Hydrogen, the first three electrons of Argon and the first two of Helium calculated for a pulse of length 50 fs FWHM.

4.1.4 Introduction to particle-in-cell simulations

A PIC simulation models the intricate physics of plasmas by using a spatial grid to calculate the dynamics of the electric, $\vec{E}(\vec{r},t)$, and magnetic, $\vec{B}(\vec{r},t)$, fields as well as the charge, $\rho(\vec{r},t)$, and current, $\vec{J}(\vec{r},t)$, densities. In a typical plasma wake-field accelerator, a cylindrical plasma of operating density $10^{16}\,\mathrm{cm}^{-3}$ of radius $0.5\,\mathrm{mm}$ and length of $50\,\mathrm{mm}$[1] will contain approximately 3×10^{14} particles. Rather than computing the properties of each individual plasma electron, a PIC simulation will use macro-particles which each represent numerous individual particles in order to reduce the computational demands of the simulation.

PIC simulations take place in a cycle, during which the physical interaction is calculated for a short time-step. In each step, the position and momentum of each macro particle will be used to calculate the charge and current densities, $\rho(\vec{r},t)$ and $\vec{J}(\vec{r},t)$. This is commonly referred to as 'current deposition'. These densities will then be used to determine the electric and magnetic fields, $\vec{E}(\vec{r},t)$ and $\vec{B}(\vec{r},t)$. The last step is to calculate the effect of these electric fields on the macro-particles, which will be pushed to a new location and the simulation cycle will begin again. Even with these methods, a PIC simulation is computationally expensive, requiring the use of multi-core processing on high performance computing infrastructure. The simulations presented in this work were performed across the DESY-based Maxwell cluster and the Juwells cluster at the Jülich Supercomputing Centre [108].

[1] Typical parameters expected at FLASHForward

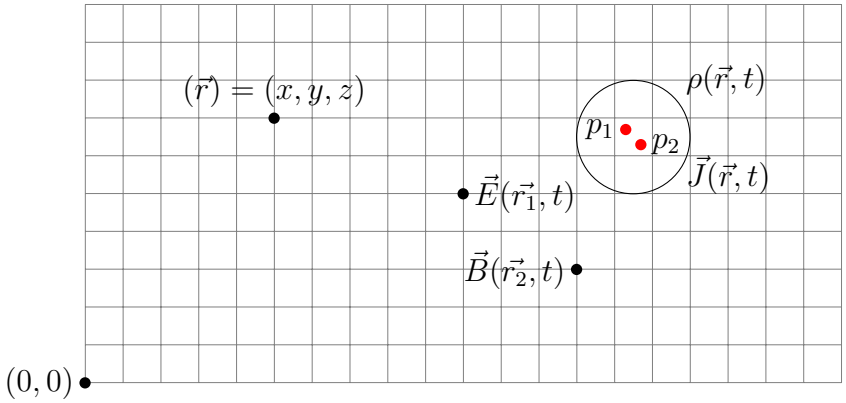

Figure 4.6: A simplified diagram of a PIC simulation. The macro-particles, p_1 and p_2 will have their properties (position and momentum) determined from the charge- and current-density profiles, $\rho(\vec{r}, t)$ and $\vec{J}(\vec{r}, t)$ respectivity. They will then be acted upon by the calculated fields $\vec{E}(\vec{r}, t)$ and $\vec{B}(\vec{r}, t)$. The particle positions and momenta will determine the charge and current densities, from which the electric fields will be recalculated.

4.2 Study Parameter Range

The study parameter range was heavily dependent on the gasses available for ionisation. Ideally the ionisation energy of the background and dopant species should be well separated such that intensities of the two laser pulses can be tuned to the desired ionisation levels. At FLASHForward Hydrogen, Argon and Helium are the preferred modes of operation and the first ionisation levels of these gases are plotted in Figure 4.5. Hydrogen would be the ideal choice as a background species due to its low ionisation energy; the large energy separation to the first ionisation level of helium then makes it a clear choice for the dopant species.

However, at the time of the experimental run, the hardware needed for the operation of hydrogen was not in operation, therefore argon-I was substituted for the background species. The remaining levels of argon have ionisation energies similar to those of helium-I and therefore these levels are expected to also contribute. The relative number of dopant electrons could be controlled by varying the ratio of helium to argon. A number of simulations in this chapter were performed with the expectation of using hydrogen as the background species which will be indicated where necessary.

Additional constraints were placed on the parameter range by the physical dimensions of the FLASHForward Target chamber and the space surrounding it. The chamber had a diameter of $500\,\mathrm{mm}$, with the viewports increasing the minimum distance from the electron

beam axis to the windows to 300 mm. To preserve the energy and beam quality of the high power laser, as few optical elements as possible should be used in the transport line. Where possible these should be reflective components, as transmissive optics will have a much larger impact on the properties of the beam. These boundary conditions therefore make techniques such as an insert into the chamber with a lens infeasible. Other solutions such as placing the focusing optics inside the chamber would have required in-vacuum motors in order to align the laser, which are strictly prohibited in order to prevent contaminants from entering the high-quality FLASH vacuum. Therefore the study began with a lower bound of 300 mm on the focal length, to focus the transverse laser.

4.2.1 Simulation set up

The simulations performed in this chapter were largely based around an idealised case within the parameter range for FLASHForward. A 500 pC of 25 μm RMS length electron beam with 2 μm emittance (2.5 kA peak current) at an energy of 1 GeV was focused to a spot size of 6 μm and then incident into a plasma with a nominal[2] flat density profile of $4 \times 10^{16}\,\mathrm{cm}^{-3}$, which yields the optimum accelerating gradient for the length of the drive bunch [109]. The simulations were performed using the OSIRIS [110] PIC code using a $576 \times 256 \times 256$ grid on a $10 \times 8 \times 8$ box (distances given in units of plasma skin depth [3]) or 26.57 μm × 20.56 μm × 20.56 μm.

4.3 Simulation Results

4.3.1 Transverse plasma size

The role of the plasma-filament size was simulated using a virtual aperture scan. The scan was carried out in the near-field, with a variable-sized mask applied to a 45 mm FWHM beam. The effect of the aperture on the laser energy was neglected by normalising the intensity to a set value of $2 \times 10^{15}\,\mathrm{W\,cm}^{-2}$. This was carried out in order to isolate the effect of the laser spot size and maintain a realistic filament shape. The radius of the aperture was scanned in steps from 30 mm down to 2 mm and then focused by a 651 mm focal-length lens. This

[2] If not otherwise specified, the nominal density refers to the density of the background plasma ionised by the longitudinal laser

[3] $\delta(n_0 = 4 \times 10^{16}\,\mathrm{cm}^{-3}) = 26.57\,\mu\mathrm{m}$

is visualised in Figure 4.7 where in (a) an aperture is applied to the near-field profile which results in a significantly larger far-field beam profile (b). The far-field intensity profiles have then been used in Figure 4.7(c) to calculate the expected shape of the plasma-filament, which significantly increases in size as the aperture is narrowed.

Each plasma profile was fitted with a super-Gaussian function and used as an input into a PIC-simulation. In this case, only the ionisation of helium was investigated as the dopant species, assuming a singly ionised background-gas species with equal proportions of argon and helium. As discussed in Section 4.1.3, the ionisation profile of the laser takes the form of an elongated ellipsoid which may be approximated by a cylindrical profile within a Rayleigh length of the focal-spot position. For these simulations, the effect of the plasma profile width was isolated by only considering the profile in the longitudinal direction.

The amount of injected charge was evaluated after $4\,\mathrm{mm}$ of propagation and is plotted against the aperture radius in Figure 4.8. The injected charge was seen to decrease with an increasing aperture radius. To explain this behaviour, Figure 4.9 explores the phase and electron velocities along the plasma profiles used in the scan. In subplot Figure 4.9(a) the individual ramps are shown; the effect on the phase (β_{ph}) and electron (β_z) velocities are shown Figure 4.9(b). Figure 4.9(c) uses these velocities to evaluate $f_{inj} = \beta_z - \beta_{ph}$. As explored in Section 2.7.1, when this is greater than zero (indicated by the grey dotted line) the condition for injection is satisfied and electrons may propagate forward in order to be trapped and accelerated. The electron velocities have been determined from simulation data provided by the authors of [52].

The extent and shape of the region over which the trapping condition, $f_{inj} > 0$, is satisfied will have an impact on the injection process. This is explored in Figure 4.10, where the data in Figure 4.9 has been use to parameterise the ramp in order to estimate the amount of charge available for injection along its length. The charge available for injection may be estimated by integrating the plasma density $n_e(r, z)$ over the region in which the injection condition is satisfied.

$$Q_{inj}^{est} = 2\pi \int_{r_0}^{r_1} r\, dr \int_{z_0}^{z_1} n_e(z)\, dz, \tag{4.8}$$

where z_0 and z_1 are the roots of the injection function f_{inj}. The term $2\pi \int_{r_0}^{r_1} r dr$ is included in the integral, along with the longitudinal component in order to produce a result term that is dimensionally consistent with the injected charge. The values r_1 and r_0 are the radial

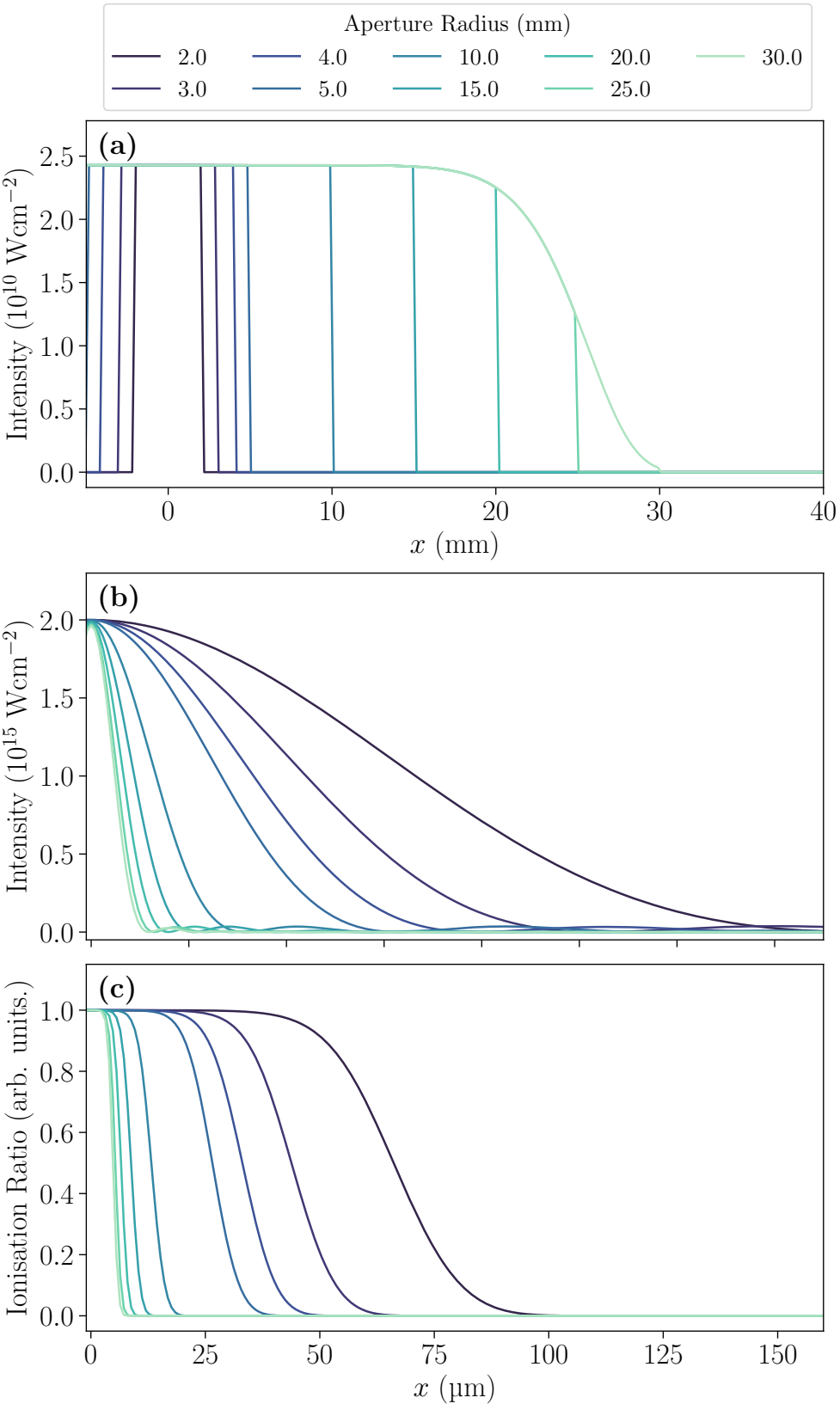

Figure 4.7: A visualisation of the virtual aperture scan in the (a) near-field and (b) far-field of the laser and its effect on the ionisation profiles in focus (c).

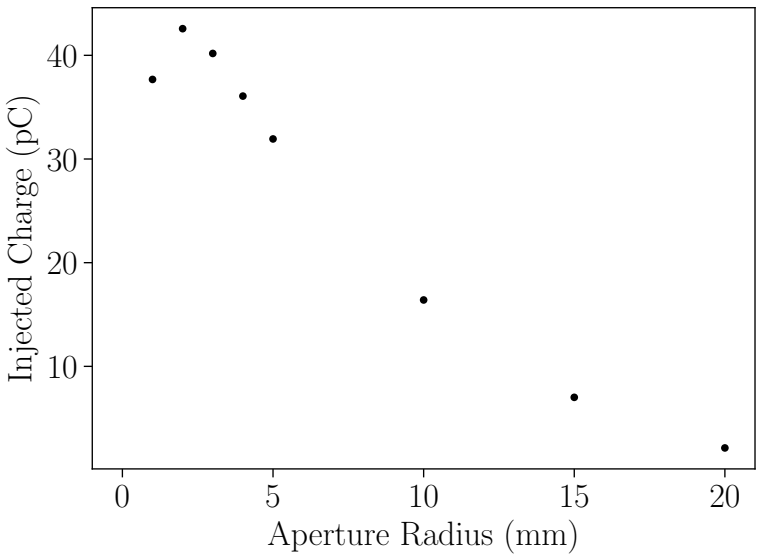

Figure 4.8: The injected charge plotted as a function of the aperture radius.

boundaries of the torus whence in the plasma those electrons that are trapped originate. The value of the radial integral is assumed to remain constant throughout the scan and may be determined via a linear fit to the injected charge. However in this work the radial term is not of interest and an injection parameter P_{inj} is defined in order to neglect it.

$$P_{inj} = \frac{Q_{inj}^{est}}{2\pi \int_{r_0}^{r_1} r\, dr} = \int_{z_0}^{z_1} n_e(z)\, dz. \tag{4.9}$$

P_{inj} is now independent of the value of the radial integral which defines the charge available along the length of the down-ramp [111]. Figure 4.10(a) plots the variation of P_{inj} against the aperture radius used in the scan, where the behaviour seen in Figure 4.8 is qualitatively reproduced. Figure 4.10(b) compares this directly with the injected charge seen in simulation with a linear fit applied to the data. The linear fit appears to be a good model for the injected charge. The two smallest aperture radii correspond to total beam energies of 45 and 170 mJ. These cases were explored to evaluate the extreme case of a very narrow aperture in order to produce a large plasma in focus. However, these energy densities are not practical to achieve within the boundary conditions of the experiment. Such energy densities may be available at facilities with a much larger near-field laser profile and longer focal lengths.

These simulations were carried out with a 651 mm focal length lens. At aperture radii be-

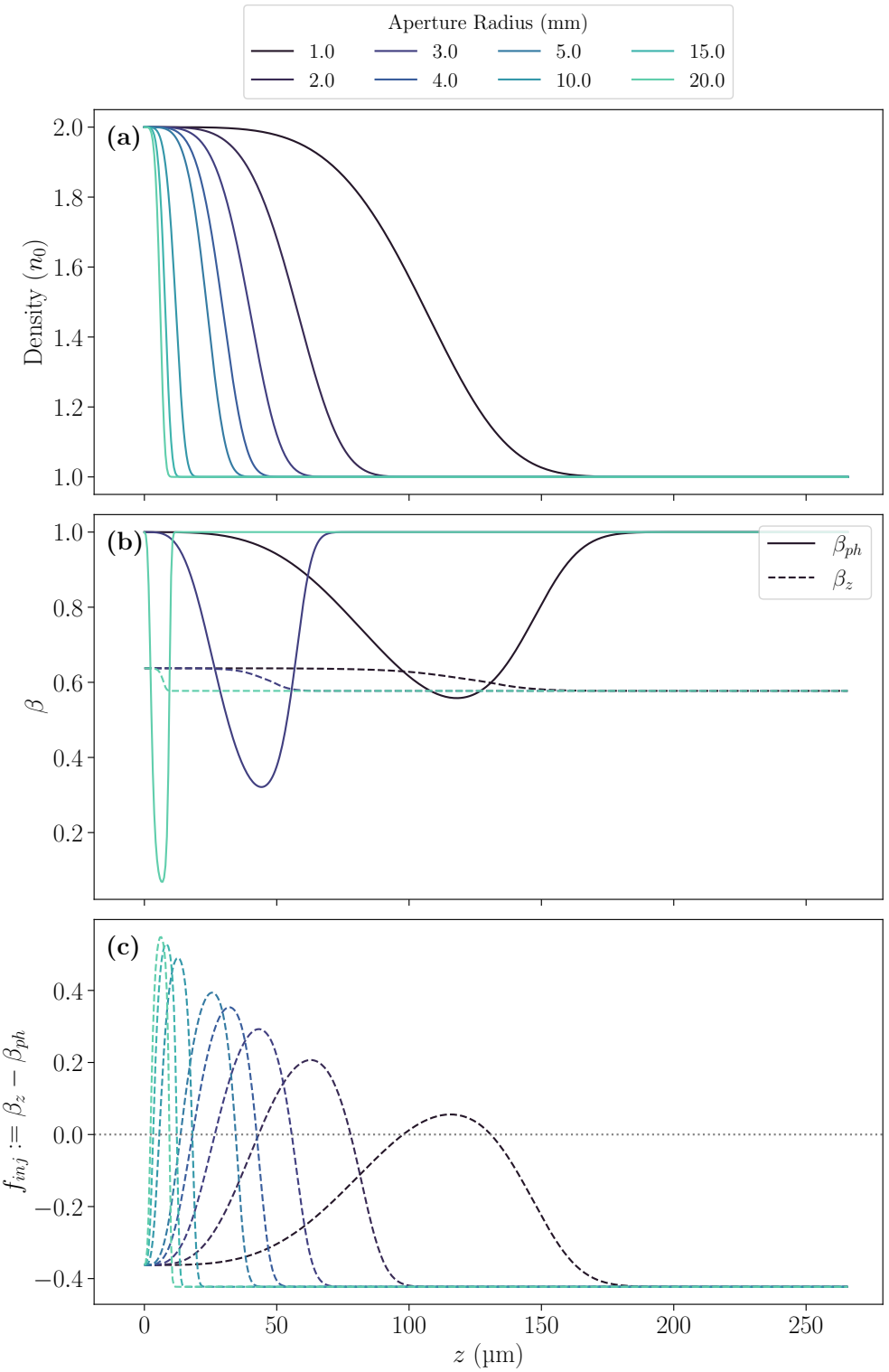

Figure 4.9: A schematic of the injection process on the plasma filament profiles generated during the aperture scan. (a) The down-ramps of the individual plasma filaments, (b) the behaviour of the plasma phase (β_{ph} - solid lines) and electron (β_z - dashed lines) velocities on the ramp and for three example ramps (1 mm, 3mm & 20mm) (c) the trapping condition $\beta_z - \beta_{ph}$ along the ramps depicted in (a).

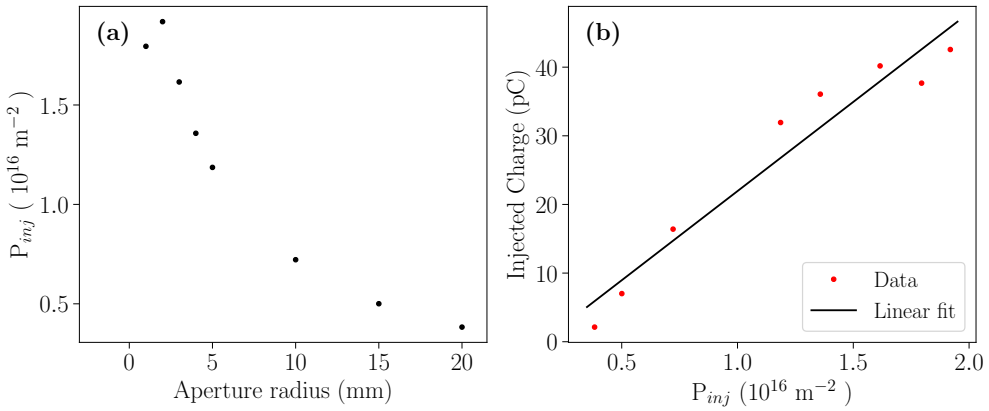

Figure 4.10: The injection parameter P_{inj} plotted in (a) as a function of the aperture radius and in (b) against the injected charge.

tween 3 and 5 mm a significant (and more importantly measurable) amount of charge was injected 32 pC to 36 pC as plotted in Figure 4.8. The energy required to create the profile at these radii is between 5 and 20 mJ, a feasible value for the laser system in question. This finding lead to the installation of the pick-off mirror discussed in Section 3.3.1 as the full-aperture beam would likely produce a plasma-filament which is too small for the injection of a significant amount of charge[4]. This also has the advantage of leaving the majority of the energy in the longitudinal transmitted beam, meaning that longitudinal ionisation is not impeded, as shown in Figure 3.5.

4.3.2 Simulations of the beam produced by a pick-off mirror

The effect of the pick-off mirror on the beam was simulated by applying a mask of radius 6.35 mm to the initialised full-aperture beam. This was then focused by a 651 mm focal-length lens. The corresponding near-field and far-field profiles are plotted in Figure 4.11. The focal spot size is 40.6 µm FWHM with a peak intensity of 2.4×10^{15} W cm^{-3}. These intensities were calculated in both regions for a beam with 2.7 mJ of energy and a pulse length of 50 fs.

The resulting focal-spot profile was then used to calculate the ionisation of helium-II and

[4]The production of a larger plasma filament may be possible with complex focusing-geometry such as a system with much longer focal length, however such geometries were deemed to complicated to implement for this experiment

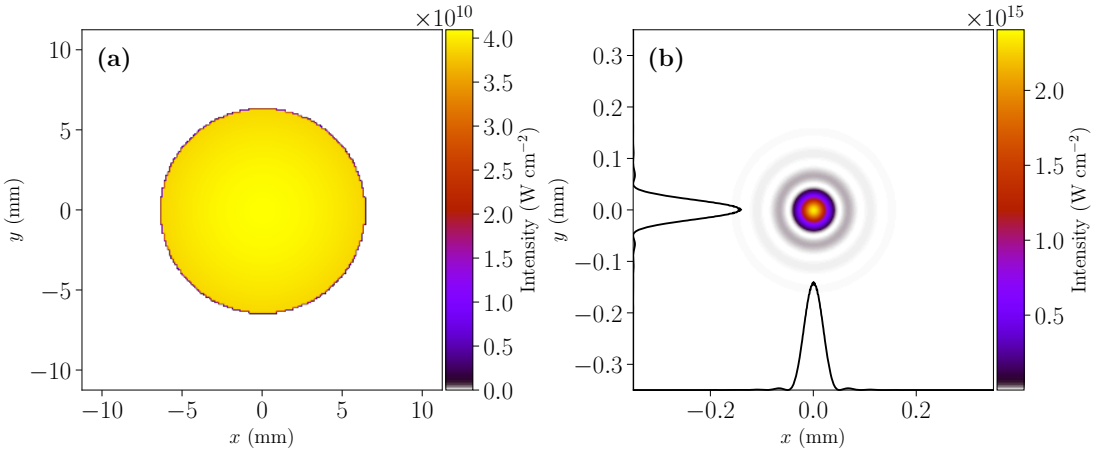

Figure 4.11: Simulation of the use of a pick-off mirror in the (a) near-field and (b) far-field

argon-II and III. The ionisation of these three ionisation species is plotted in Figure 4.12. Figure 4.12(a) shows the profile in one dimension where the contribution of each ionisation species is indicated by colour; Figure 4.12(b) shows the two dimensional profile. The total height of the plasma-filament may be adjusted by varying the mixing ratio of helium and argon. The use of three species ionisation to produce the plasma filament produces a taller and longer ramp which the simulations suggest increases the charge injected in simulations by a factor of roughly three. In these simulations the ramp was now also defined in two dimensions as shown in Figure 4.12, so that the filament is also truncated in one transverse dimension.

The bunch injected by the profiles shown in Figure 4.12 is shown in Figure 4.13. After 6 mm of propagation, the bunch had a charge of 103 pC with normalised emittances of $1.41\,\mu\text{m} \times 1.23\,\mu\text{m}$ in the x and y directions respectively, where x is the propagation axis of the transverse laser. It is important to note the asymmetries in the emittance values in the two transverse dimensions as this will become larger in later simulations. This asymmetrical bunch is expected to arise due to the intrinsic asymmetry of the plasma filament, which is truncated in the longitudinal and one transverse dimension and can be considered semi-infinite in the remaining transverse dimension. This assumption was made due to the Rayleigh length of the laser focus being approximately 4.66 mm[5]. Since the Rayleigh length is much larger than the simulation box itself, the laser focal-spot intensity and therefore the

[5]estimated for a Gaussian beam, Gaussian optics remain a good approximation for most laser beams, even when their profile is not strictly Gaussian

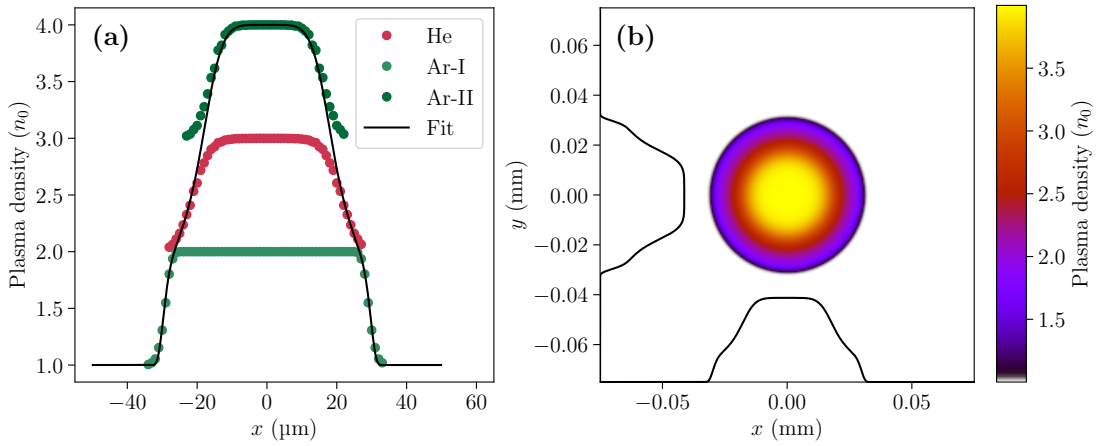

Figure 4.12: The plasma density calculated for the beam reflected from the pick-off mirror. (a) The central slice density profile plotted separately for each ionisation species and the overall fit to the density profile. The colours are used to indicate the individual contributions of each ionisation level to the overall filament profile. (b) the total two dimensional density profile

plasma-filament which it produces were assumed not to vary significantly over the box used in the simulation. Simulations performed with a one-dimensional ramp which is infinite in both transverse planes do not show this asymmetry. This asymmetry is also expected to cause the charge model used in the aperture scan to breakdown as the system is no longer cylindrically symmetric.

Exactly how these asymmetries in the injected bunch arise is the subject of further investigation. Detailed examination of the electron-bunch distribution reveals that it is not composed of one homogenous distribution, but rather two electron bunches or beamlets which oscillate around the centre of the plasma blowout. This inhomogeneity is displayed in the plane in which the plasma filament is truncated and is absent in the other dimension, as shown in Figure 4.14. This distinctive distribution shape is absent in the previous simulations in which the filament profile was homogenous between the two transverse dimensions.

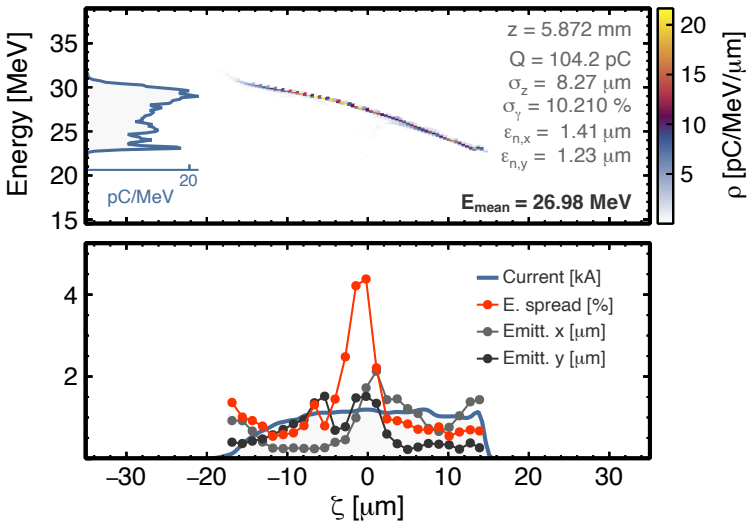

Figure 4.13: The parameters and longitudinal phase space of the injected witness-beam. The upper plot shows 1D and 2D histograms of the beam in the energy and longitudinal spaces. The lower plot shows the beam current, energy spread and emittances.

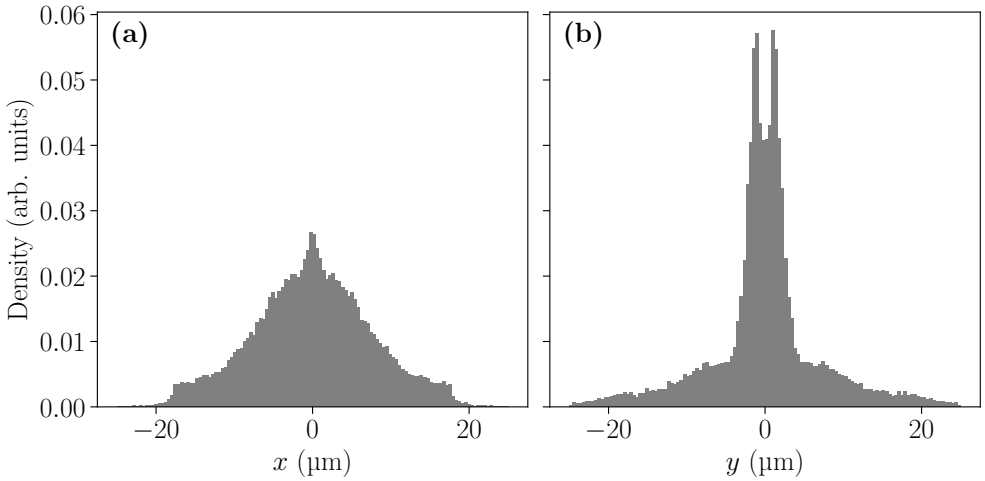

Figure 4.14: The distribution of the injected electron bunch immediately after injection with a two-dimensional plasma filament in the (a) $x - z$ and (b) $y - z$ planes.

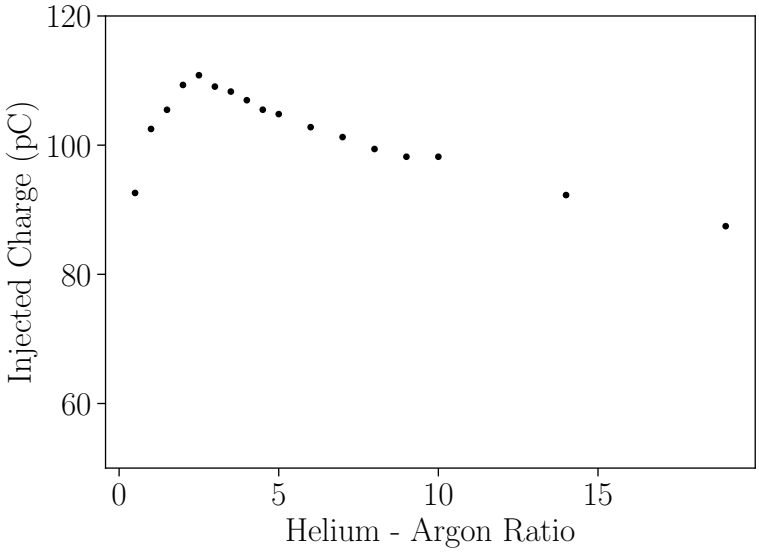

Figure 4.15: The charge of the simulated witness-beam as a function of the helium to argon ratio

4.3.3 Effect of the gas-mixing ratio

The impact of the mixing ratio of helium and argon was explored through another series of simulations. For these simulations, a plasma-density profile was fitted to each ionisation species independently. Therefore the mixing ratio could be adjusted with a simple change of the coefficient for the helium contribution. The expressions used for each ionisation level in this scan are listed in Table 4.1. The ratio of helium to argon was scanned between 0.5 and 20 by changing the value of N_{He} in Table 4.1, N_{Ar} was fixed at a value of 1. This range was selected to characterise a large range of ratios.

Ionisation Species	Expression
Argon-II	$N_{Ar} \times \exp\left(-\left(\frac{(z-z_0)^2}{1.39} + \frac{(y-y_0)^2}{1.39}\right)^{12.78}\right)$
Argon-III	$N_{Ar} \times \exp\left(-\left(\frac{(z-z_0)^2}{0.59} + \frac{(y-y_0)^2}{0.59}\right)^{4.43}\right)$
Helium-I	$N_{He} \times \exp\left(-\left(\frac{(z-z_0)^2}{0.88} + \frac{(y-y_0)^2}{0.88}\right)^{4.01}\right)$

Table 4.1: The expression used to describe the contribution of each ionisation level to the overall plasma filament shape in a scan over gas ratios. For the scan N_{Ar} was set to 1 and N_{He} was varied between 0.5 and 20.

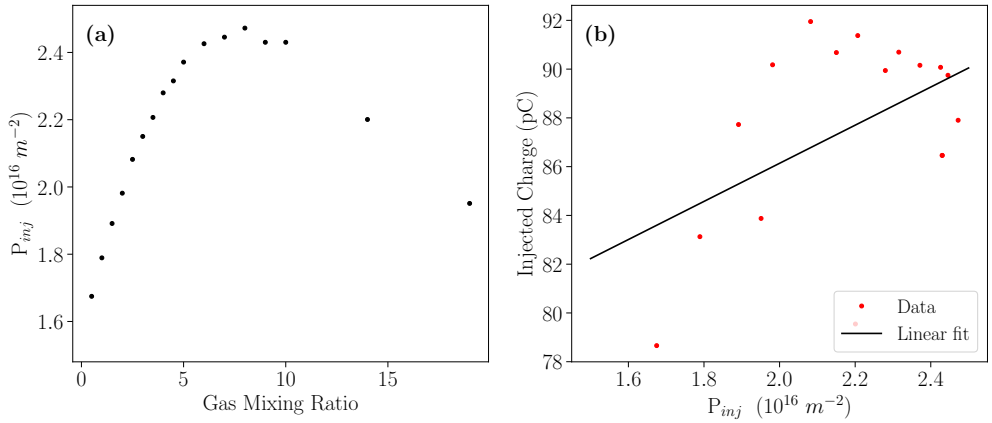

Figure 4.16: The injection parameter, P_{inj}, over the course of the gas ratio scan. (a) the parameter against the gas mixing ratio while (b) the parameter against the total injected charge. As discussed in the text, the cylindrical symmetry assumed when calculating P_{inj} no longer applies and therefore the linear fit no longer applies.

The resulting impact on the charge of the injected bunches is shown in Figure 4.15. The charge remains fairly constant and as shown in Figure 4.16, this is assumed to be due to less variation occurring in P_{inj} over the course of the scan. However, these simulations were carried out using the two-dimensional expression for the plasma filament shape as shown in Figure 4.12, which is not cylindrically symmetric around the z-axis. This absence of cylindrical symmetry is assumed to result in charge and P_{inj} no longer being linearly correlated as seen in Section 4.3.1, which now limits the application of the model.

Figure 4.17 explores this further by looking at the injection function over the full extent of the down-ramp for three different ratios of Helium and Argon. The ratios selected correspond to the start of the scan (He-Ar ratio of 0.5:1), the peak of the injected charge (2.5:1) and the point where the amount of charge has fallen again, but P_{inj} is maximised (9:1). The injection now occurs over a region with a marked difference in shape between the two transverse planes. In the y-plane, it is annular compared to infinite in the x-plane. A clear difference in the shape of the leading edge of the injection region between the steps in the scan is observed. This leading edge is where the injection will be initiated and therefore its shape will be crucial to the amount of charge that becomes trapped in the plasma wake. In Figure 4.17 the two-dimensional injection function is shown to be curved with radii between 10 and 20 μm. Along the course of the down-ramps the plasma-blowout radius will vary between 16 and 80 μm as shown in Figure 4.18, where the maximum extent of the blow-out has been calculated for each of the down-ramps shown in Figure 4.19 assuming that $k_p r_b \simeq 3$ [112]. There-

fore the curvature of the injection region can be expected to have an impact on the injection process.

The effect of the gas-mixing ratio on the emittances of the injected witness-beams is explored in Figure 4.21. In contrast to the charge, a large change is seen in the horizontal plane, where the emittance decreases as the helium ratio increases. The effect of the increased ratio on the injection parameters has been explored in Figure 4.19. This effect is attributed to the multiple ionisation levels that are now present in the plasma-filament. Here it is seen that the injection function f_{inj} no longer consist of a single peak but instead contains many peaks. The transitions between these peaks occur at the points where the individual filaments formed by one ionisation species meet those of another. At these points, the plasma-density gradient is briefly reduced before increasing again at the down-ramp corresponding to the next ionisation species. These transitions act to briefly slow down the injection process which is likely to be sub-optimal for the injection of high-quality bunches.

In Figure 4.20 the effect of the gas-mixing ratio on the spatial distribution of the electron bunch immediately after injection is explored. Figure 4.20(a) plots the RMS Beamsize, which can be seen to decrease as a function of increasing gas-mixing ratio in both planes. Figure 4.20(b) plots the mean position. However, as the spatial distribution of the bunch is expected to be symmetrical around the central axis, the mean position will ordinarily not be of much interest as it would be expected to be identically zero. Therefore in order to better demonstrate the effect of the gas-ratio scan, two different methods have been used: In the x-plane the analysis has been carried out using the standard method with the raw data, which results in the expected value of zero for all points. However, in the y-plane, the analysis was carried out using the absolute value of the electron positions. Here it is seen that the electron bunch moves towards the centre as the gas-mixing ratio increases. These effects partially explain the impact on the electron beam emittances which are plotted in Figure 4.21. Here the emittance is seen to fall in the y plane but increase in the x plane with increasing amounts of helium in the gas mixture. The reduction in emittance in the x plane is assumed to be a result of the reduced RMS beamsize.

In an ideal case, the gas-mixing ratio should be selected to minimise the emittance of the electron beams. Alternatively, the effect of the contribution of multiple ionisation levels to the ramp shape would be removed by using an alternative gas such as hydrogen. In this dataset, the emittance minimum occurs at a helium-to-argon ratio of 10-1, at which point the

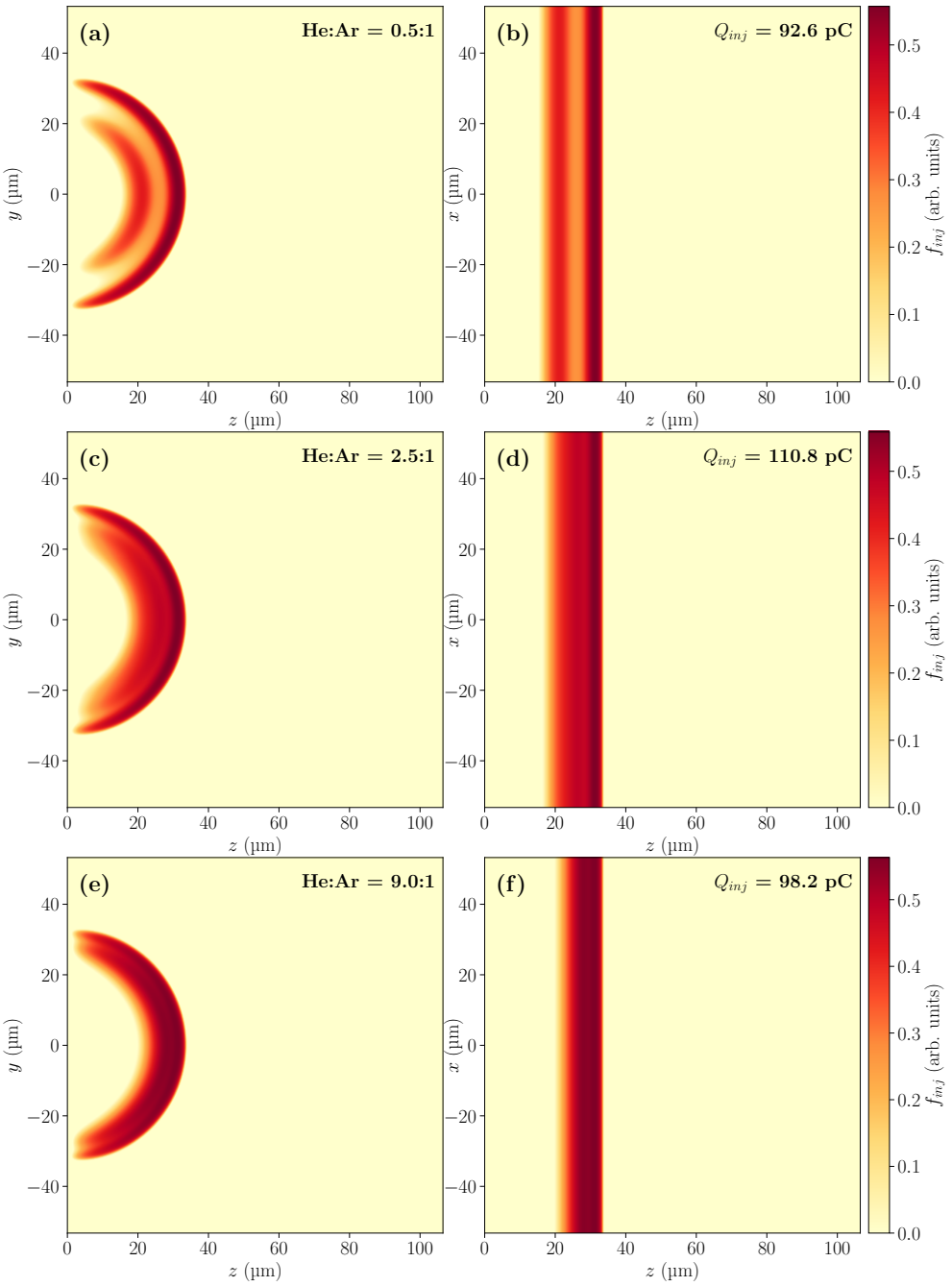

Figure 4.17: The two-dimensional shape of the injection region f_{inj} where $\beta_z > \beta_{ph}$ and electrons are able to propagate forward with respect to the wake-field. The shape is seen to change significantly for the different ratios of helium to argon.

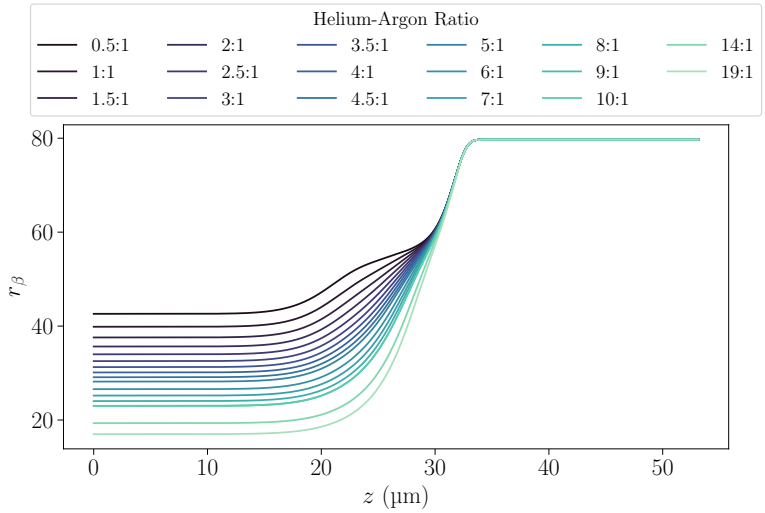

Figure 4.18: The maximum radii of the plasma blow-outs calculated along each of the ramps plotted in Figure 4.19. These radii were calculated to find the maximum extent of the region according to $k_p r_b \simeq 3$ [112]

plasma filament is twelve times denser than the background. Such a high ratio is likely to result in an excessive gas load on the vacuum system and the pumps, so the ratio should be set to one that is as high as possible while not exceeding 10-1, while avoiding excessively loading the pumping system.

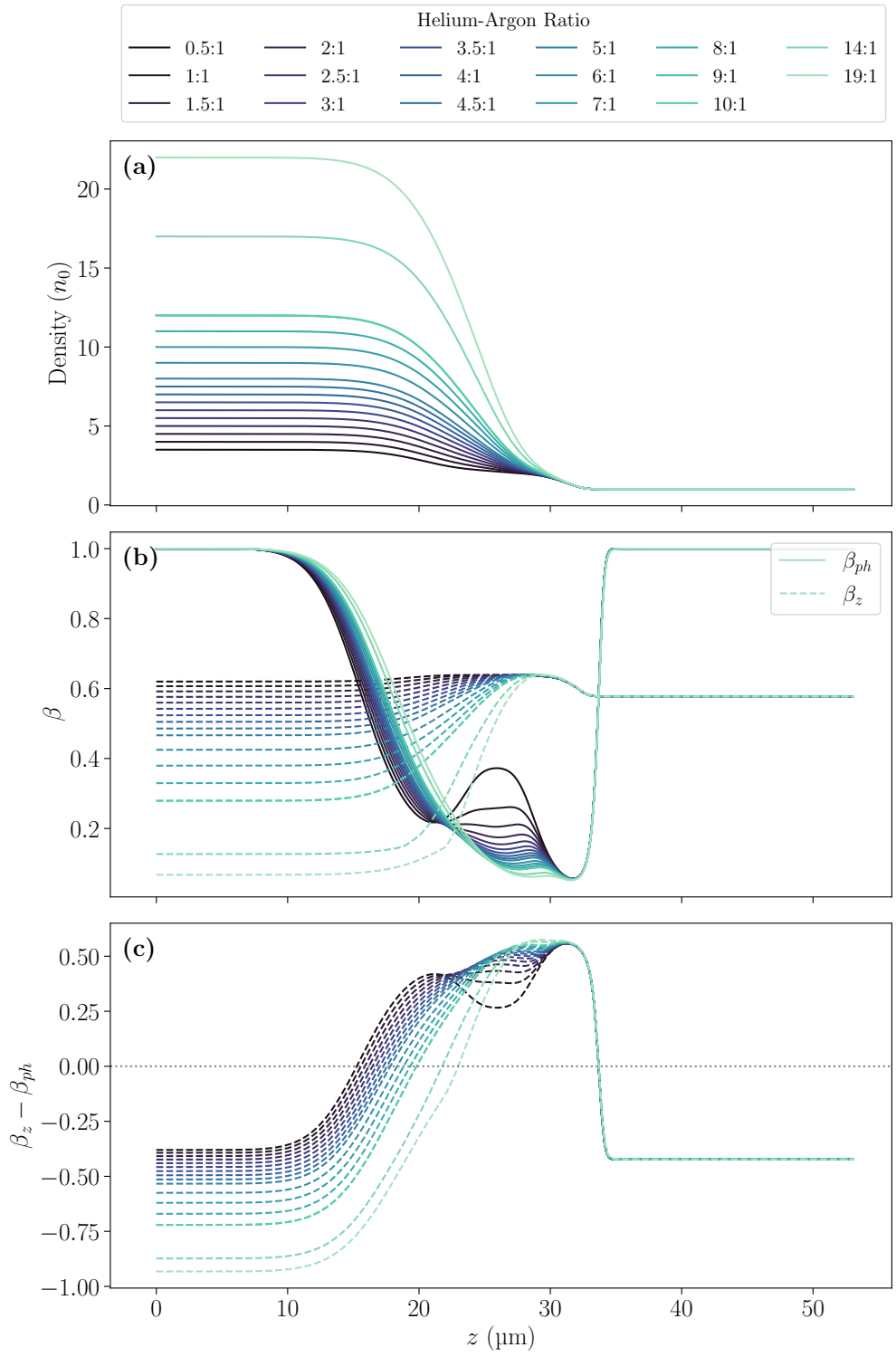

Figure 4.19: A schematic of the injection process on the plasma filament profiles generated during the gas-ratio scan. (a) The down-ramps of the individual plasma filaments, (b) the behaviour of the plasma phase (β_{ph}) and electron (β_z - dotted lines) velocities on the ramp and (c) the trapping condition $\beta_z - \beta_{ph}$ along the ramps depicted in (a). Darker colours correspond to lower ratios of helium and to argon as shown in the legend above the first plot

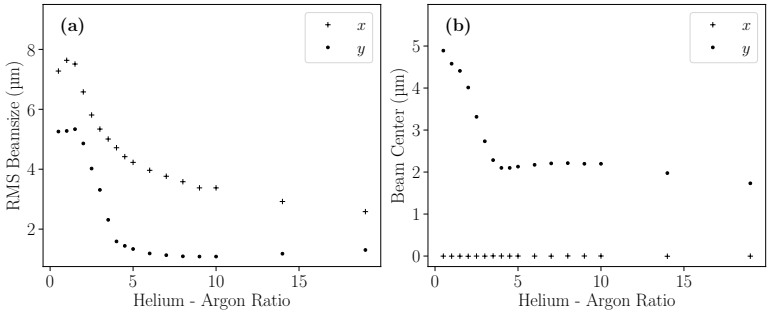

Figure 4.20: Effect of the gas mixing ratio on (a) the RMS beam size and (b) the mean electron position. In subplot (b) two different methods of analysis have been applied. The x values represent the mean of a distribution which is symmetrical around zero while the y values represent the mean of the absolute values. See text for further details.

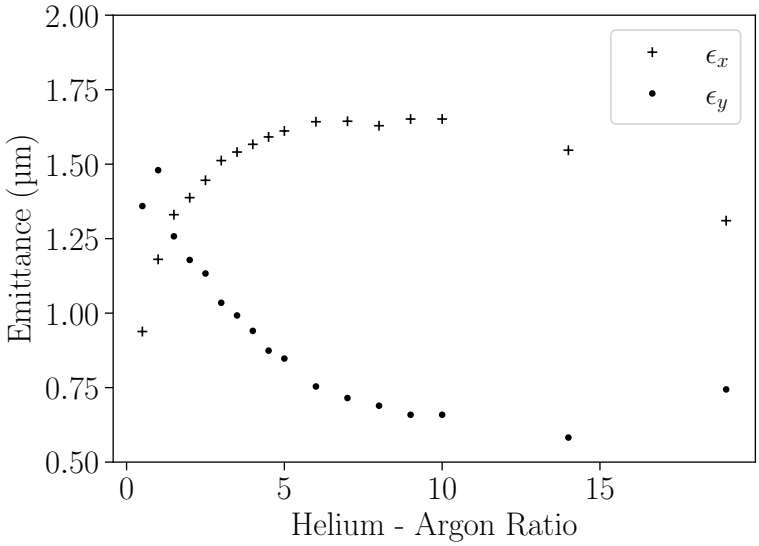

Figure 4.21: The emittance of the witness-beam as a function of the helium to argon ratio

4.3.4 Effect of Plasma filament position and alignment

Due to the small scale of the plasma filament ionised by the transverse laser, precise overlap between the electron beam, longitudinal plasma and transverse plasma is expected to be crucial to the injection process. In practice this will need be to achieved by precisely aligning the electron- and two laser-beams to one another. The impact of any potential misalignments in the system was explored in a series of simulations by varying the value of y_0 listed in Table 4.1 to scan the plasma filament over the electron-beam axis. In these simulations, the value of y_0 was scanned in $5\,\mu\mathrm{m}$ steps between -10 and $40\,\mu\mathrm{m}$ with the ratio of helium to argon set at $9:1$. This shifts the plasma filament in the y direction and results in the plasma-wake encountering down-ramps with differing shapes and heights. The induced asymmetry of the ramp in the y direction is expected to have the greatest impact on the injection and capture of electrons in the half of the plasma cavity where the density is reduced.

The effect of the asymmetry on the trapping process is explored in simulation in Figure 4.22, which plots the charge (normalised to the peak value of injected charge) over the propagation distance. As the witness bunch propagates, some charge is always lost, since some electrons will have a transverse momentum sufficiently large to escape the trapping forces of the wake-field. In this plot, it is apparent that significantly more charge is lost as the offset increases.

Figures 4.23 & 4.24 provide some insight into why this might be the case. Here the electron spatial (Fig. 4.23) and momentum (Fig. 4.24) distributions of the witness bunch are plotted for the $x-z$ and $y-z$ planes immediately after injection. The distributions have been plotted for three offset positions -10, 10 and $20\,\mu\mathrm{m}$. In the spatial domain, the distribution in the x plane remains symmetrical with some slight broadening. However, in the y plane the distribution is shown to shift to favour one side of the blowout. Figure 4.25 shows the charge and emittance of the injected bunches. As the wake-field trapping strength is shown to decrease with increasing offset values, this results in the charge falling linearly with the position of the filament at a rate of $(2.10 \pm 0.34)\,\mathrm{pC}\,\mu\mathrm{m}^{-1}$. The emittance is consequently shown to increase slightly in the x direction, while decreasing by a factor of two in the y direction likely due to the reduced charge in the bunch.

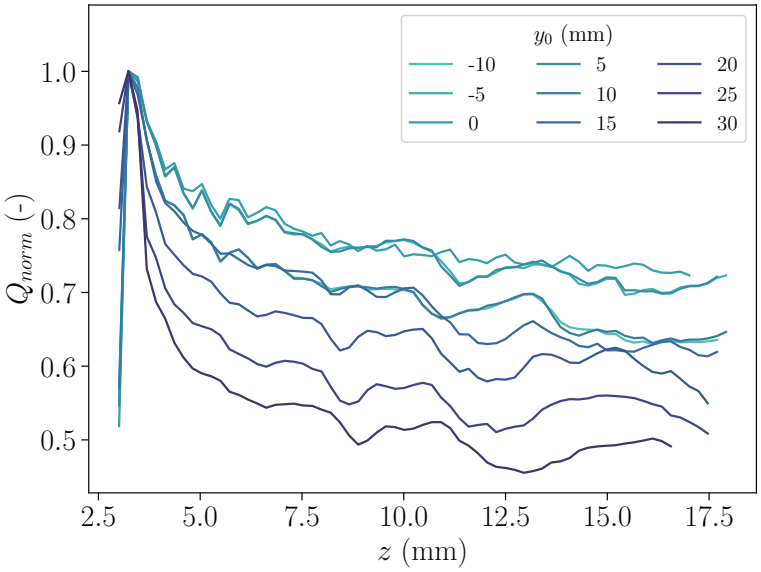

Figure 4.22: The effect of the trapping on the normalised charge of the injected bunches. The charge Q_{norm} has been normalised to the peak value of injected charge to better highlight reduction in trapping efficiency

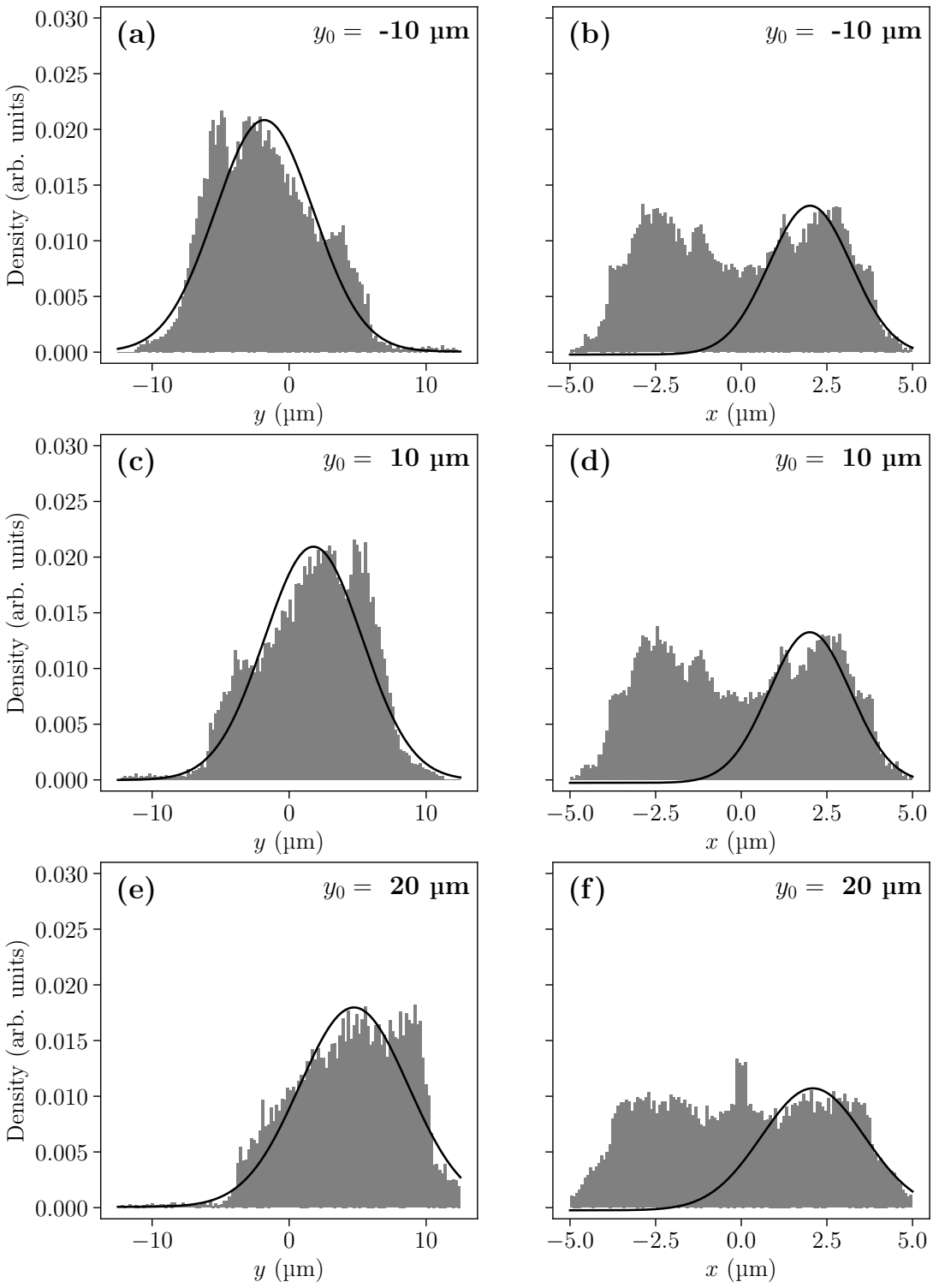

Figure 4.23: The electron distribution in x & y for three selected points during the offset scan. The x distribution is seen to remain fairly symmetrical, while the y distribution becomes significantly more off-centred. The fitted curves (black) in y represent a gaussian fit to the whole distribution which is asymmetrical around $y = 0$. In x the histograms appear to be symmetrical around $x = 0$ and therefore have been fitted to one size of the distribution only.

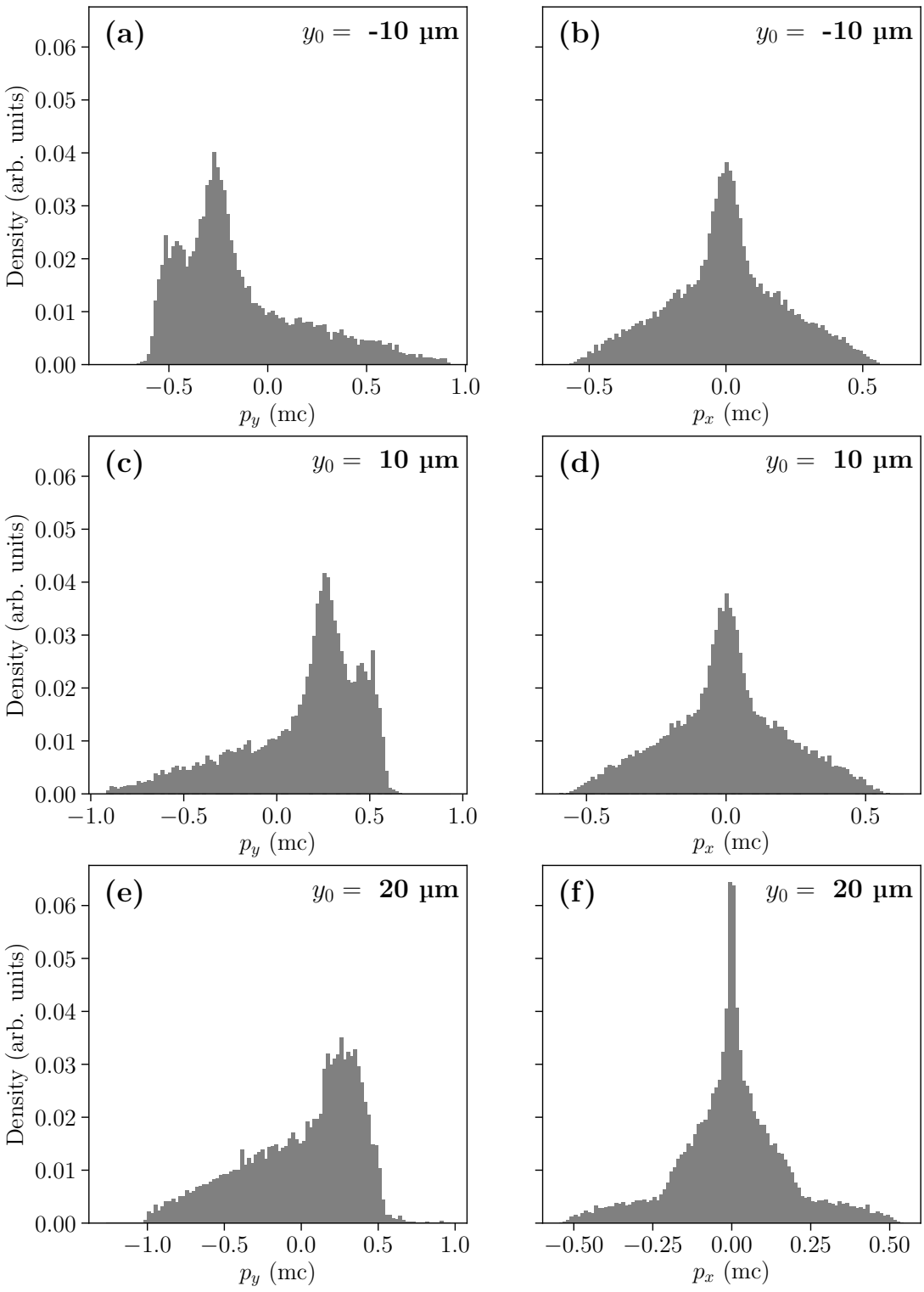

Figure 4.24: The distributions in momentum space of the bunches immediately after injection.

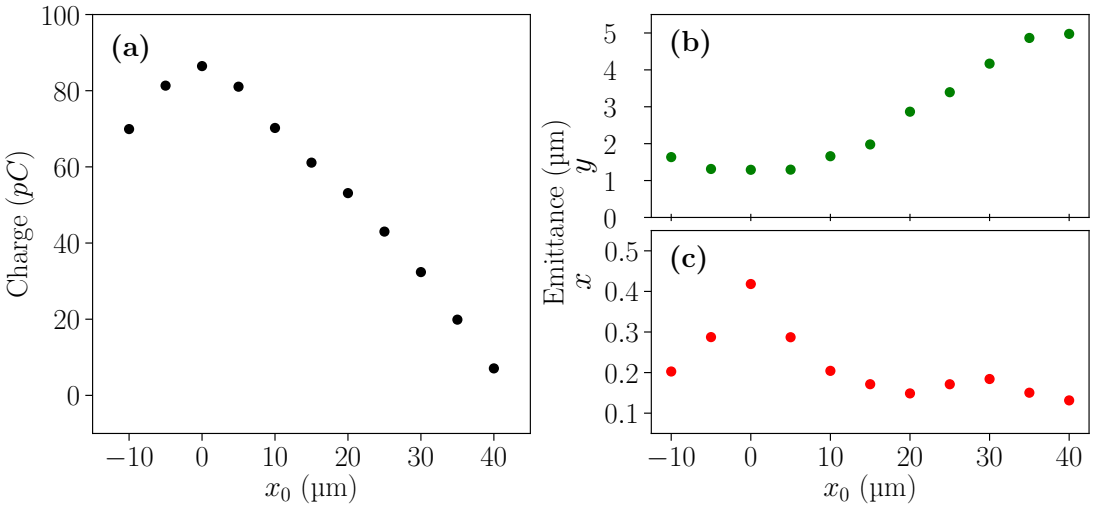

Figure 4.25: The results of the offset scan for (a) charge and (b & c) emittance of the injected witness-beams as a function of the offset value x_0.

In order to understand the injection process under the conditions outlined in Chapter 3, a further set of simulations was performed. The box size was $460 \times 400 \times 200$ μm with a $256 \times 256 \times 256$ grid. The plasma profile seen in Figure 3.18 (b) was fitted using a combination of 2 semi-super-Gaussian functions. In contrast to previous simulations, these no longer represented single ionisation species and instead represented the plasma as a whole; two functions were used in order to capture fully the shape of the plasma. In addition the plasma profile could no longer be described with a simple super-Gaussian profile and instead required the use of a modified version to extend the profile and rotate it to improve the description of the shape of the plasma profile. The modified profile had the form shown in Equation 4.10,

$$\begin{aligned} n_p =& R_1 \cdot \exp\left(\left(\frac{(z-z_{0,1})^2}{2(\sigma_{z_1} - k_{z_1}(z-z_{0,1}))^2} + \frac{(y-y_{0,1})^2}{2\cdot(\sigma_{y_1} - k_{y_1}\cdot(y-y_{0,1})^2}\right)^{P_1}\right) \\ &+ R_2 \cdot \exp\left(\left(\frac{(z-z_{0,2})^2}{2\cdot(\sigma_{z_2} - k_{z_2}(z-z_{0,2})^2} + \frac{(y-y_{0,2})^2}{2(\sigma_{y2} - k_{y2}\cdot(y-y_{0,2}))^2}\right)^{P_2}\right). \end{aligned} \tag{4.10}$$

The final fit and its discrepancy with respect to Figure 3.18 are shown in Figure 4.26. The fit is good, with the discrepancies between the fit and the calculated ramp approaching 5 %, which is well below the uncertainty in the plasma density. At the time of writing, only plasma density functions which could be represented by an analytical function could be imported into OSIRIS as the infrastructure to import a numerically defined density was not available.

A snapshot from the simulation is shown in Figure 4.27 and the phase space of the injected witness bunch in Figure 4.28. As will be discussed in Chapter 5, this simulation was performed with a plasma filament offset by $25\,\mu\mathrm{m}$ from the electron-beam and longitudinal-laser axes. These snapshots were produced from data taken $10.32\,\mathrm{mm}$ after the point of injection.

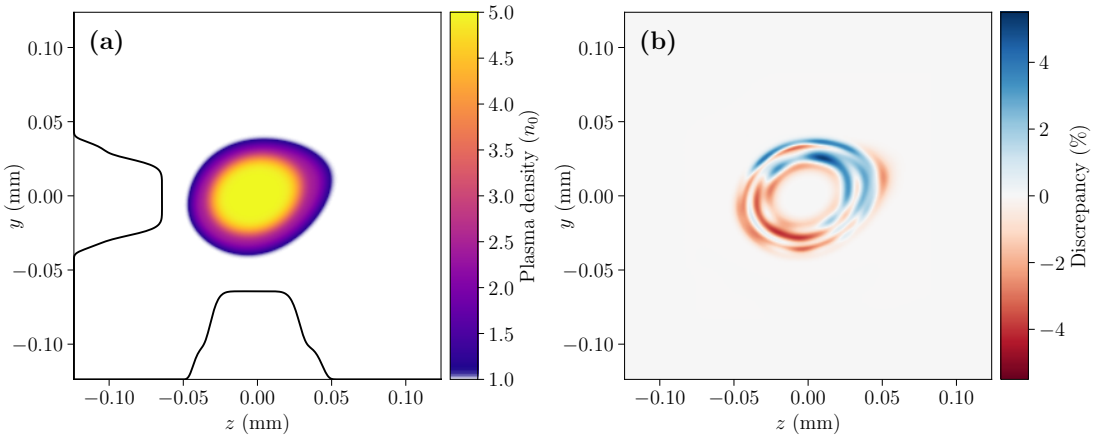

Figure 4.26: The performance of the fit to the plasma density. (a) The two-dimensional fitted plasma profile (b) the percentage error of the fit in comparison to that calculated using the ADK formula in Figure 3.18

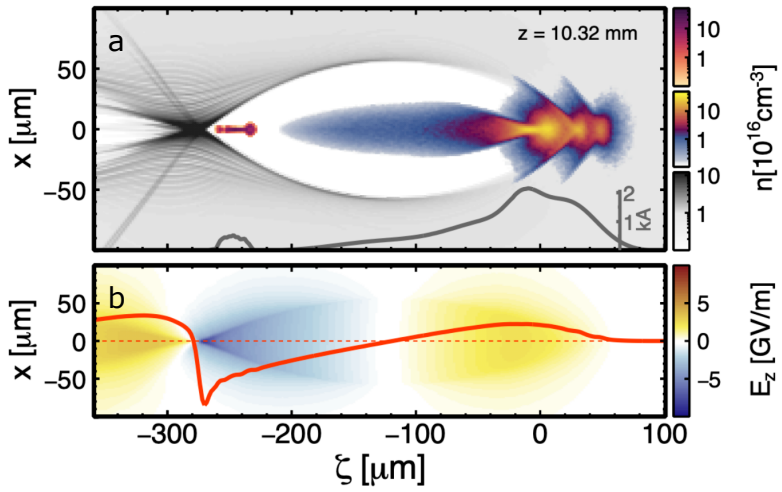

Figure 4.27: A snapshot of the simulation taken 10.32 mm after injection. (a) Overall densities of the plasma (grey), drive beam (centre right) and witness-beam (centre left). (b) Accelerating fields of the central slice with the central lineout in red

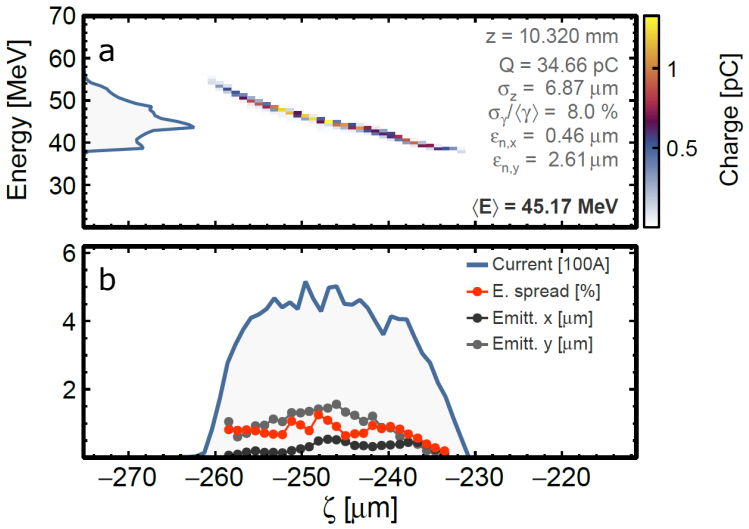

Figure 4.28: Longitudinal phase space of the witness-beam 10.32 mm after injection with (a) overall beam parameters and (b) slice parameters

4.5 Conclusion

These simulations show the effects of various experimental parameters on the properties of the injected witness-beams. The focus of this chapter was to explore the effects of the parameter-space that could be investigated during an experimental run. Initial simulations suggested that within the range of optimum plasma densities for the FLASH electron beam, the use of the full aperture (45 mm FWHM) laser beam, was likely to result in a plasma-filament profile that is too small for injection to occur. Options to increase this would require an order of magnitude increase in the focal length, plasma density or both. The simplest option however, was to reduce the aperture of the secondary laser using a half-inch diameter pick-off mirror, which had already been installed in the beam-line.

Simulations were performed in which the full aperture beam was cut down to the the size of the pick-off. The resulting focus and plasma were then calculated, fitted and used as input into a PIC simulation. Further simulations were performed to explore the effects of varying the dopant gas mixture and the position of the plasma-filament in preparation for the experimental run. These simulations all showed reliable injection, producing beams which should be well above the experimental detection thresholds. The charge and emittance of the beam also appear to be tuneable by varying the position and height of the plasma-filament.

5

Injection of witness-beams on a density down-ramp at FLASHForward

This section describes the results of X-1 experiment at FLASHForward. Section 5.1 describes how, prior to the commencement of the injection experiment, spatial and temporal overlap was achieved between the three beams used in the experiment. Following on from this, Section 5.2 showcases the first demonstration of stable internal-injection on a density down-ramp in PWFA. The methods used to calculate the charge of the witness-beam and factors such as the relative laser-to-electron-beam offset and the laser energy which contribute to the jitter of the electron-beam parameters are then described. Section 5.4 discusses the agreement between parameters seen in the simulations of Section 4.4 and the experimental results and introduces potential mechanisms to explain any discrepancies.

5.1 Three-beam spatio-temporal overlap

The three beams must be overlapped both spatially and temporally. The spatial overlap was first carried out using the two OTR screens: The position of the electron and longitudinal laser were imaged on both the upstream and downstream OTR cameras and the two signals

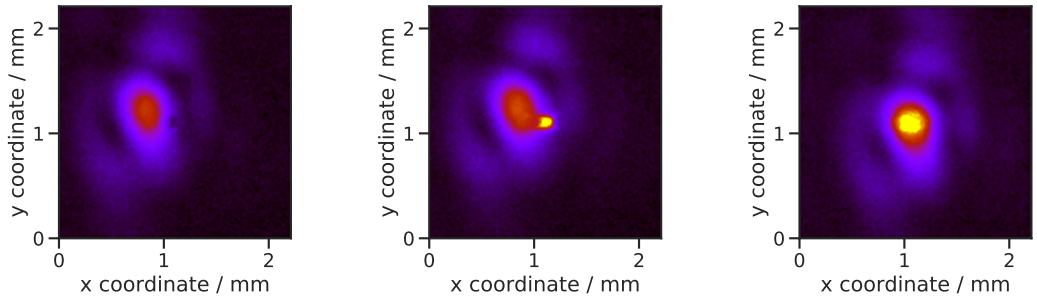

Figure 5.1: The process of spatially aligning the electron-beam and the longitudinal laser. (a) the longitudinal laser only, (b) the laser and the electron-beam which are offset to one another, (c) after adjusting the final spherical mirror to centre the laser and the elctron beam.

overlapped by adjusting the angle of the final spherical mirror. Since both beams were already on a path well defined by the electron-beam-line itself, only small changes to the alignment were needed to overlap the laser with the electron-beam on both screens which required only one mirror to be adjusted instead of the usual two. The process of this alignment can be seen in Figure 5.1. The transverse laser was transmitted through a gap between the OTR screen and the holder, such that it could be viewed simultaneously on the US_OTR camera. It was brought into vertical alignment with the electron-beam using the y stage of the TFA.

The temporal overlap was more complicated and was split into two procedures known as *coarse* and *fine* timing. The coarse timing was carried out using either the upstream OTR screen. The arrival time of both laser pulses was adjusted by tuning the delay of the trigger provided to the laser from the FLASH timing system. The camera exposure time was first reduced to the shortest possible time of $18\,\mu s$ and the timing between the beams adjusted until both beams could be seen on the screen where the maximum separation between them was given by the exposure time of the camera. The delay between the beams was then further shortened to under a microsecond by shifting the signals to the leading edge of the exposure window where, due to the readout procedure of the camera, only half the pixels would see the beam.

Following the microsecond-level pulse synchronisation, fine timing was carried out to reduce the difference in arrival time down to the picosecond level. This was carried out using the expected observation that an increased plasma-light output correlates strongly with the

energy loss of the electron-beam [113] as measured on the electron spectrometer. The correlation between these signals at FLASHForward is explored in Figure 5.2. Figure 5.2(a) shows the light-output as a function of the relative time of arrival of the longitudinal ionising laser and the electron-beam; Figure Figure 5.2(b) shows the corresponding electron spectromenter images for each of the steps in (a). The signal is shown to have a fast – sub picosecond – onset time. Additionally, Figure 5.2(c) shows that the light output from the plasma is seen to be linearly correlated to the mean energy loss of the driver, supporting the theory and evidence presented by Scherkl et al in [113]. Finally Figure 5.2(d) shows the average image taken at the beginning and end of the timing scan, depicting how the appearance of the plasma changes over the course of the scan.

These characteristics make the plasma-glow signal an ideal tool to determine the relative arrival times of the electron-beam and the two laser pulses. The relative arrival time of the laser pulses – both being derived from the same laser system – was fixed by the relative path length between the two arms and was set at 20 ps using the delay stage and a fast diode, connected to an oscilloscope, to observe the two laser pulses.

The arrival time of the laser with respect to the electron-beam could be controlled on a picosecond timescale using the oscillator-based FLASH laser-synchronisation system [114]. The system changes the length of the oscillator cavity in order to shift the phase of the laser pulse with respect to a reference pulse from the FLASH master oscillator. The system was used to bring the electron-beam and laser into a timing regime where the plasma-glow signal could be turned off and on by adjusting the timing by a single picosecond. This signal was then used to set the arrival of the longitudinal and transverse lasers to be approximately 40 and 20 ps, respectively, before the arrival of the electron-beam, as shown in Figure 5.3. The arrival of both lasers prior to the electron-beam is to ensure that the injection falls entirely in the Laser-Triggered Density Down-ramp Injection(LT-DDI) scheme.

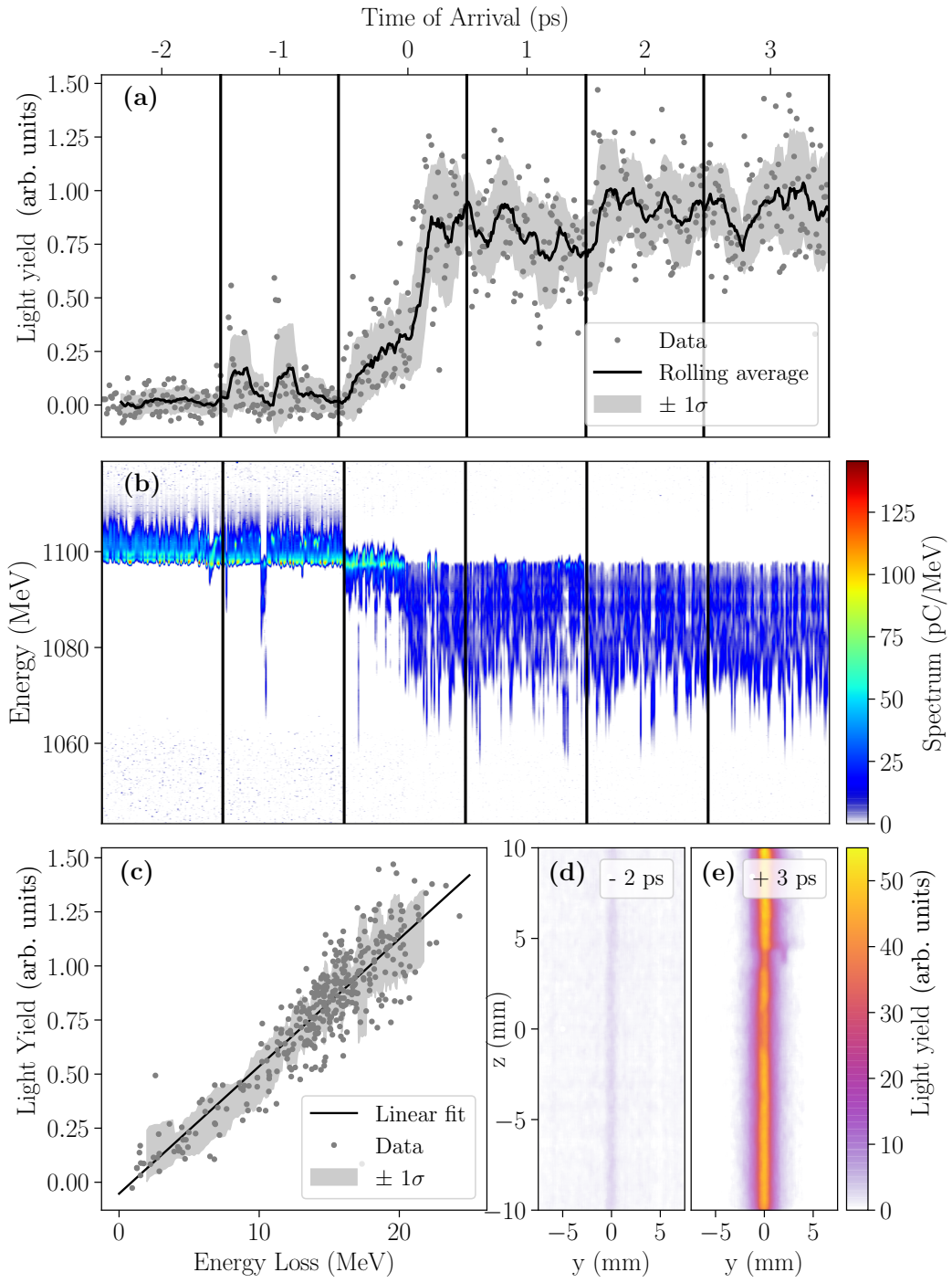

Figure 5.2: The plasma-glow signal as studied at FLASHForward in October 2018. The signal was studied by varying the phase shifter in picosecond steps while observing the electron-beam and plasma on the Electron Spectrometer and Target Side View Cameras, respectively. Here the arrival time corresponds to the arrival time of the electron-beam after the laser. (a) The integrated signal on the target side view camera as a function of laser to electron-beam arrival time. (b) A waterfall plot of the electron-beam on the electron spectrometer over the same range as (a). (c) The correlation between the mean energy loss seen on the spectrometer in (c) – calculated by subtracting the mean of each shot from 1.1 GeV – and the integrated plasma signal (data points without any interaction have been removed). (d) & (e) The average plasma light yield as seen at (d) −2 ps and at (e) 3 ps.

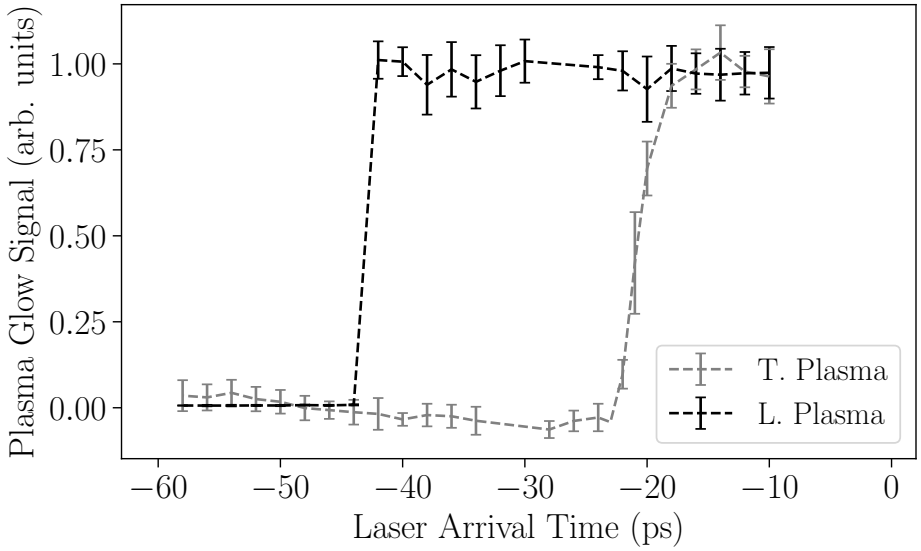

Figure 5.3: The plasma-glow signal for the longitudinal and transverse plasmas plotted as a function of the timing shifter delay. The signals are plotted with respect to the arrival time of the electron-beam at t = 0 ps. The error bars were calculated by taking the mean and standard deviation of 10 images per step.

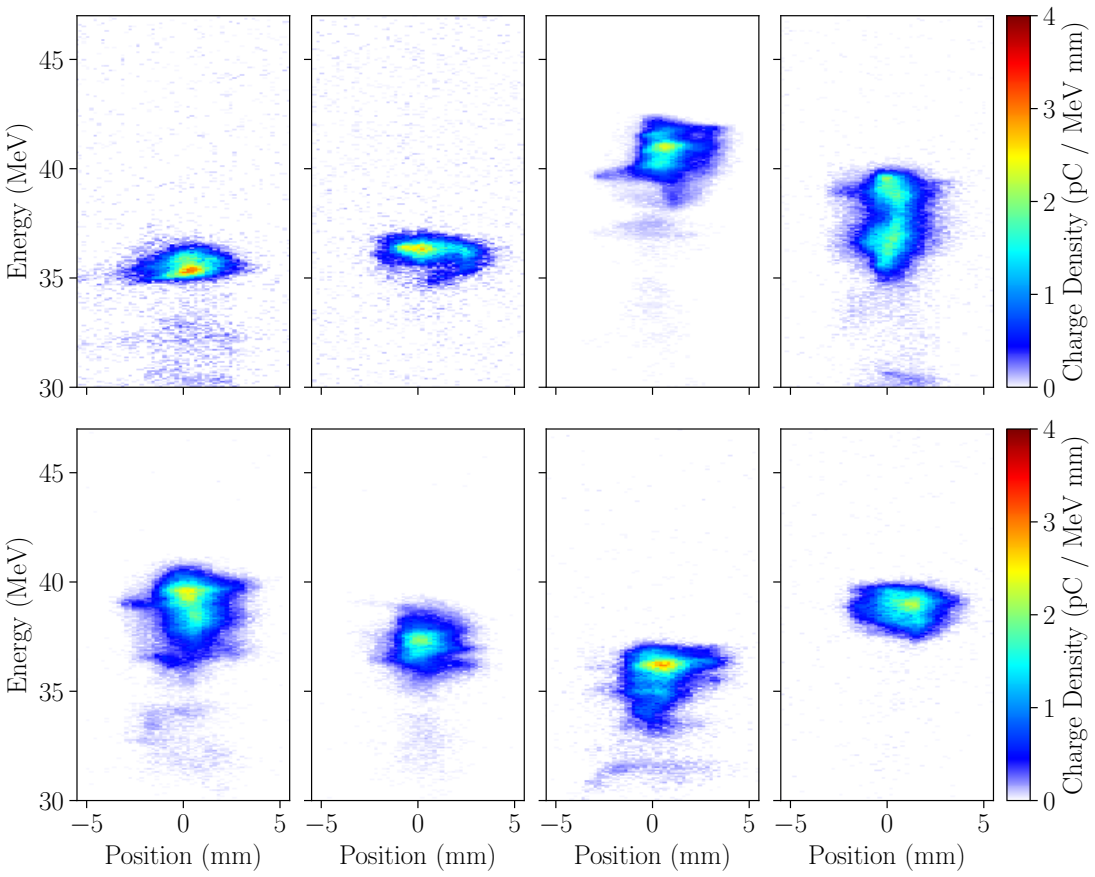

Figure 5.4: Selected electron-spectrometer images with witness-beams; the charge has been calibrated using the methods described in Appendix B.

5.2 Injection results

After achieving the spatio-temporal overlap of all three beams and optimising their transmission through the capillary, internally injected witness-beams were observed for the first time at FLASHForward. Figure 5.4 shows a selection of these first beams, which fluctuated in energy from 30 MeV to 50 MeV with beam charges in the tens of pico-coulomb range. In this section the source of injection will be verified and the injected charge calibrated, followed by an investigation of the stability of charge, energy and finally the demonstration of control over these properties.

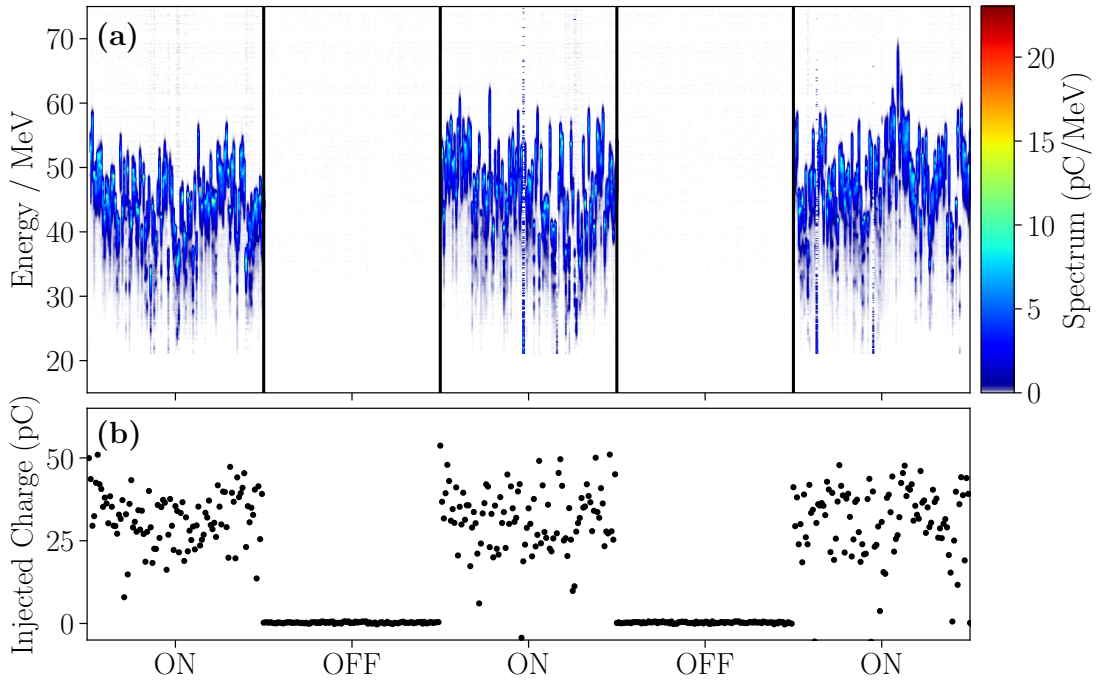

Figure 5.5: The results of a scan in which the transverse laser was allowed to propagate for 100 shots, then blocked for 100 shots and the pattern repeated. (a) The charge calibrated low-energy electron spectrometer traces (b) The surplus charge as measured by the beam-line charge diagnostics

5.2.1 Source of injection

Figure 5.5 (a) shows the low-energy spectrometer screen during a scan in which the transverse laser was turned on and off by inserting the transverse beam block into its path. There is a clear correlation between the presence of a witness-beam on the spectrometer screen and the status of the transverse laser. The charge of these beams was determined by examining any additional charge present in the beam-line after the plasma cell as will be detailed in the following Section. In summary, the presence of the transverse laser was associated with (32.8 ± 8.2) pC of surplus charge in the beam-line, while in its absence this figure was measured to be (-0.03 ± 0.20) pC. The difference is most striking in Figure 5.5(b) where the single-shot surplus charge is plotted over the scan. This phenomenon confirms that the injection is indeed triggered by the transverse laser. The 20 ps timing offset between the arrival of the electron-beam and the transverse laser as described in Section 5.1 means that injection in the so-called Trojan-Horse scheme is excluded and therefore the injection is almost certainly occurring on the down-ramp of the plasma filament created by the transverse laser.

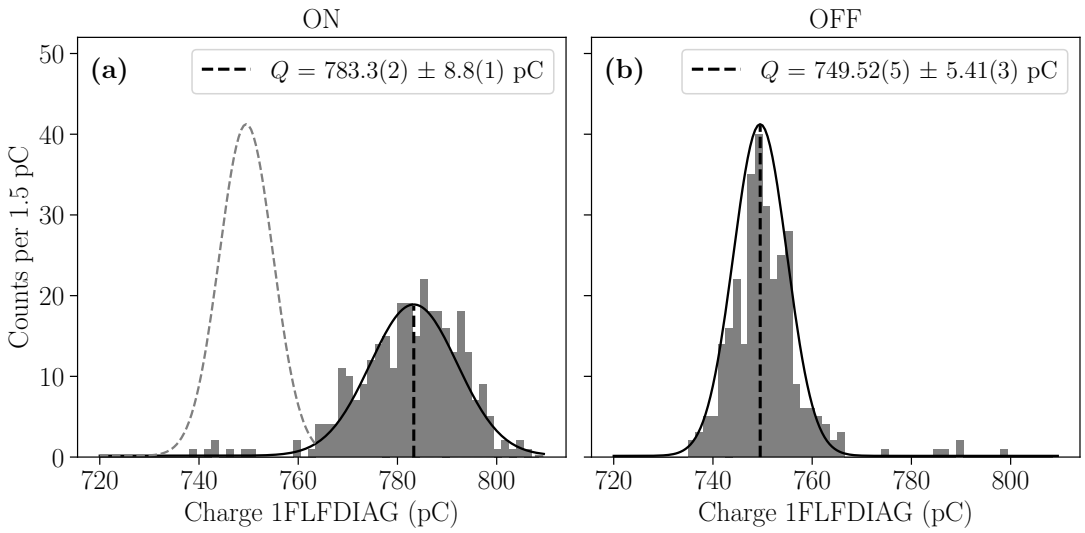

Figure 5.6: The charge measured on the 1FLFDIAG BPM with the injection laser (a) turned on and (b) off , a Gaussian function has been fitted to each distribution, the mean and standard deviation are denoted in the legend of each plot with the brackets denoting the statistical uncertainty from the fit.

5.2.2 Calibration of witness-beam charge

The data presented in Sections 5.2 & 5.2.1 show the calibrated charge present in the electron spectrometer. To achieve this the image counts in the electron spectrometer were compared to the charge diagnostics present along the beam-line. Three different charge-monitoring diagnostics were present in the beam-line prior to the plasma chamber, which were compared to the diagnostic located immediately down-stream of the plasma chamber using the data presented in Figure 5.5. The corresponding charge in the downstream diagnostic (1FLFMAFF) is plotted in Figure 5.6. The charge present in the up-stream diagnostic 7FLFMAFF is then subtracted from this quantity to calculate the charge difference along the beam-line ($\Delta Q_{\text{7FLFMAFF}}$). However, as some charge of the driver is expected to be lost during the interaction with the plasma, the value of $\Delta Q_{\text{7FLFMAFF}}$ must be corrected with an offset value which is determined by applying a linear fit against the integrated signal on the electron spectrometer to calculate the true charge difference ΔQ. The charge of the witness-beam ($Q_{witness}$) is then retrieved according to:

$$Q_{witness} = \Delta Q_{\text{7FLFMAFF}} + Q_{\text{Offset}}, \tag{5.1}$$

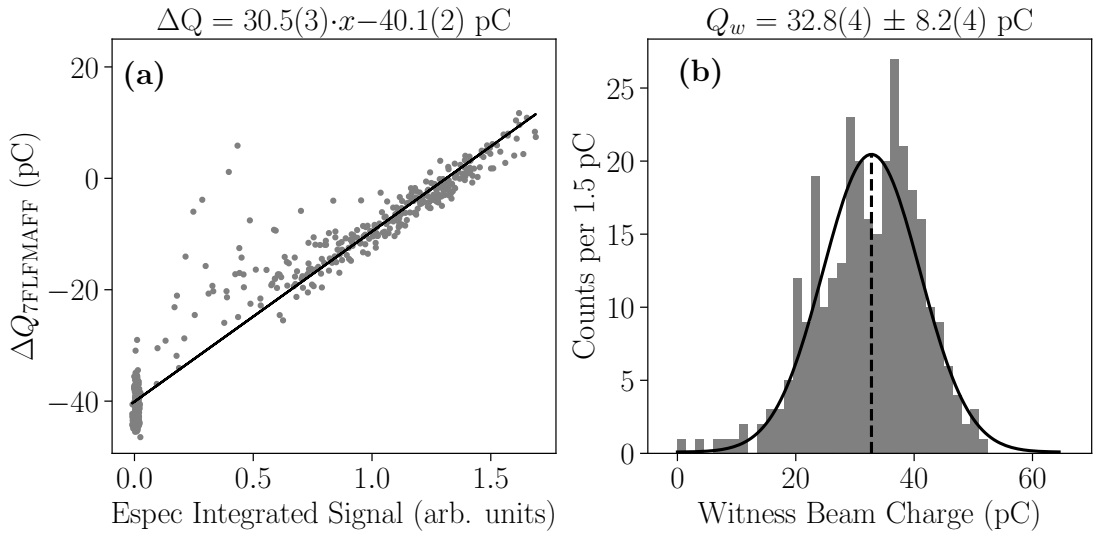

Figure 5.7: The charge calibration using the charge difference from the 7FLFMAFF charge diagnostic. In (a) a linear fit is performed to determine the value of Q_{Offset}

where Q_{Offset} is the coefficient from the linear fit, as shown in Figure 5.7(a). The offset was determined to be (40.1 ± 0.2) pC which resulted in a witness-beam charge (plotted in Figure 5.7 (b)) of (32.8 ± 8.2) pC. A full evaluation of the witness-beam charge using all three up-stream diagnostics present in the beam-line may be found in Appendix B.

5.2.3 Stability

The medium-term stability of the injection process was explored in a further dataset containing approximately 1800 sequential shots taken over a period of 10 minutes. From this dataset, the charge-calibrated spectra, mean energy and rms energy spread as well as the injected beam charge, are plotted in Figure 5.8. The charge was calculated using the excess charge in the beam-line with the 7FLFMAFF toriod as a reference diagnostic. The data, taken at 2 Hz over approximately 15 minutes, show remarkably little drift in any of the quantities plotted.

In fact the distribution of the witness-beam charge, mean and rms energy spread are dominated by random effects as show in the histograms in Figure 5.9. The mean charge was (36.1 ± 9.4) pC, as measured by excess beam-line charge and follows a Gaussian distribution. The distributions of the mean and rms energy spread also follow a similar Gaussian distribution, with the mean energies averaging (45.58 ± 4.93) MeV and an average energy

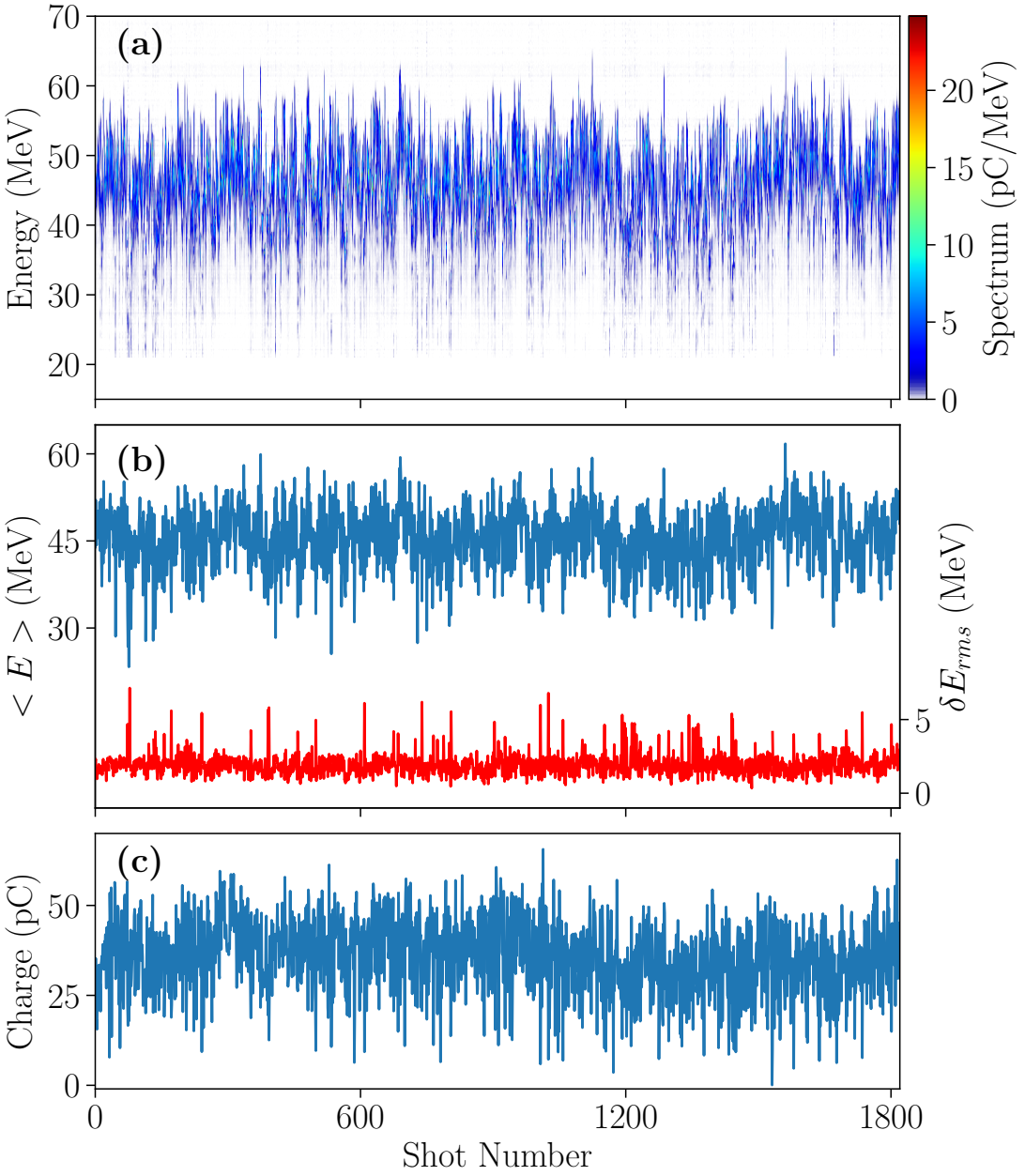

Figure 5.8: Result from the stability measurement of injected witness-beams. (a) The charge-normalised energy spectra, (b) the mean energy (blue) and rms energy-spread (red), (c) witness-beam charge as measured through excess charge

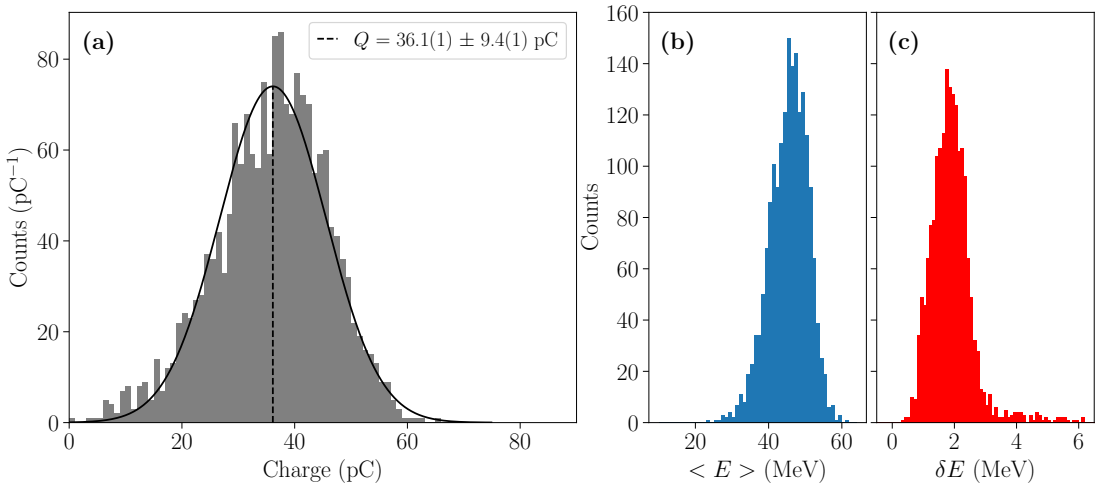

Figure 5.9: Statistical distribution of (a) the witness-beam charge with a Gaussian fit for the mean and standard deviation, (b) the mean energy and (c) the rms energy spread

spread of (1.83 ± 0.51) MeV or (3.91 ± 0.96) %.

5.2.4 Spatial Alignment

As discussed in Chapter 4, the spatial alignment of the electron-beam and the plasma filament ionised by the transverse laser is crucial to the injection process. To investigate its impact in practice, the elevation stage (y-stage in Figures 3.8 & 3.9) was used to scan the position of the transverse laser over the electron-beam axis. The resulting effect on the position of the focal-spot is shown in Figure 5.10. The position appears to have a non-linear correlation to the motor positions, while the appearance of the focal spot itself is consistent over the scan, indicating that the total weight of the optical components exceeded the capacity of the motor causing its behaviour to be non linear. Similar and repeatable behaviour was also seen when performing this calibration with the green laser. As the stage position could only be controlled using and stored in motor step position values, this results in the repeating of some absolute positions during the course of the scan.

The charge of the witness-beam is plotted as a function of the focal-spot position in Figure 5.11. In both Figure 5.10 and Figure 5.11, the zero position in y has been set to the starting position of the scan. A witness-beam was detected on the screen of the electron spectrometer from $y = 0\,\mu\mathrm{m}$ to $75\,\mu\mathrm{m}$ as shaded in grey in Figure 5.10. The region between the points labeled (b) and (c) between $30\,\mu\mathrm{m}$ to $50\,\mu\mathrm{m}$ includes several steps where the stage was stalled, and as a result the data has been sorted into bins with a $10\,\mu\mathrm{m}$ width, resulting in the two data points at $34.7\,\mu\mathrm{m}$ and $44.2\,\mu\mathrm{m}$, representing 59 and 60 shots respectively. The remaining data points each represent between 19 and 22 shots. The electron-beam was positioned low in the capillary, such that only one side of the transition could be fully characterised by this scan. The horizontal error bars include (added in quadrature) the pointing jitter of the laser ($\sigma_{x,L} = 4.04\,\mu\mathrm{m}$), the electron-beam ($\sigma_{x,e} = 1.4\,\mu\mathrm{m}$) and the uncertainty in the position arising from the binning of the data.

As expected, as the laser spot moves away from the optimum position, located at y = $(12.00 \pm 4.24)\,\mu\mathrm{m}$, there is a clear drop off in the amount of charge injected. The distribution has a larger width than those seen previously in Chapter 4, which may be attributed to a number of factors including the larger spot size or the evolution of the plasma filament in the time between its ionisation and the arrival of the electron-beam. Simulations were performed by shifting the centre of the realistic plasma profile from Section 4.4 vertically away from the electron-beam axis to a maximum of $\pm 60\,\mu\mathrm{m}$. In Figure 5.11, the simulation data

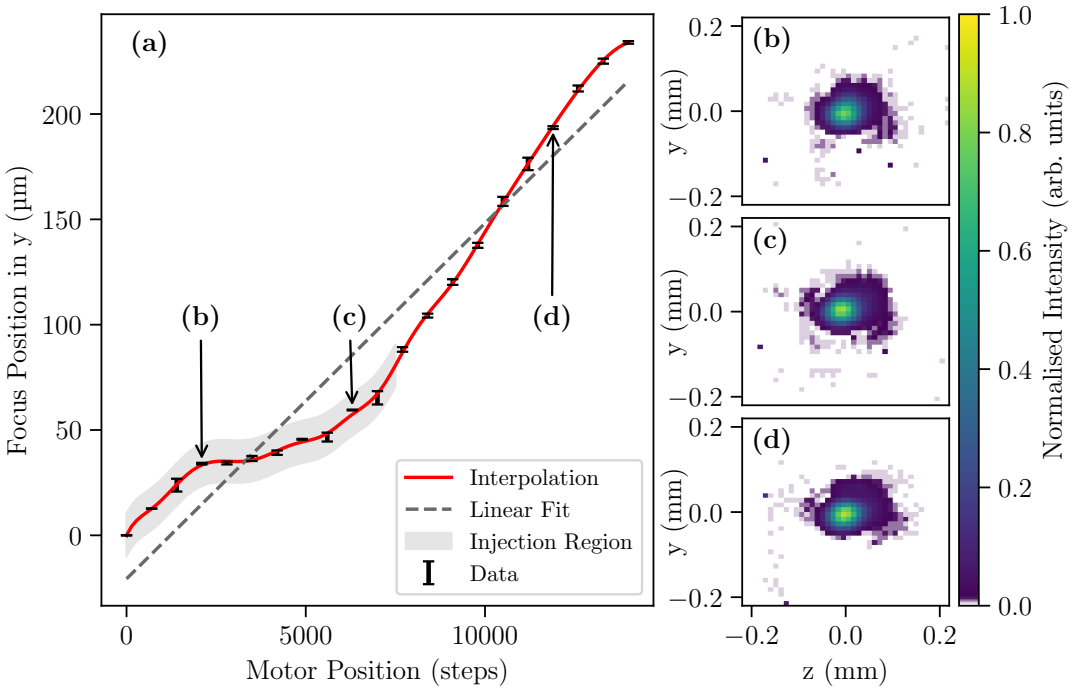

Figure 5.10: Calibration of the transverse laser offset scan. (a) the position of the focal spot with respect to the motor position, which has been fitted with both an interpolation and linear fit, the grey shading indicates the region over which injection was seen during the data taking. (b-d) representative focal-spot images for the positions along the scan which are indicated in (a). The individual laser focal-spots do not show significant evolution throughout the scan, indicating that the non-linear behaviour is not the result of any clipping of the laser pulse. The behaviour of the spot was expected to be linear with the motor position step number. However, the data indicates that its behaviour deviates significantly from linearity and therefore the interpolation curve was used to determine the absolute position of the laser spot.

has been shifted by $15.2\,\mu\mathrm{m}$ to improve the agreement between the experimental and simulated datasets. This also provides an estimate for the initial offset between the electron-beam axis and the transverse laser, as the alignment between these beams was not completed to sub-spot-size-accuracy. This offset scan was one of the final scans performed in the experimental campaign. Therefore the data presented previously were not taken at the optimum position of the laser spot but at an offset value of approximately $30\,\mu\mathrm{m}$. At this position, the simulation data have a slope of approximately $\pm 1.25\,\mathrm{pC}\,\mu\mathrm{m}^{-1}$. Combining this with the position jitter of the transverse laser in y and the electron-beam of $4.24\,\mu\mathrm{m}$ yields a charge jitter resulting from position jitter of $\Delta Q(\sigma_y) = \pm 5.3\,\mathrm{pC}$, which accounts for some of the $\Delta Q_{Total} = \pm 9.4\,\mathrm{pC}$ of charge jitter seen in the experimental data.

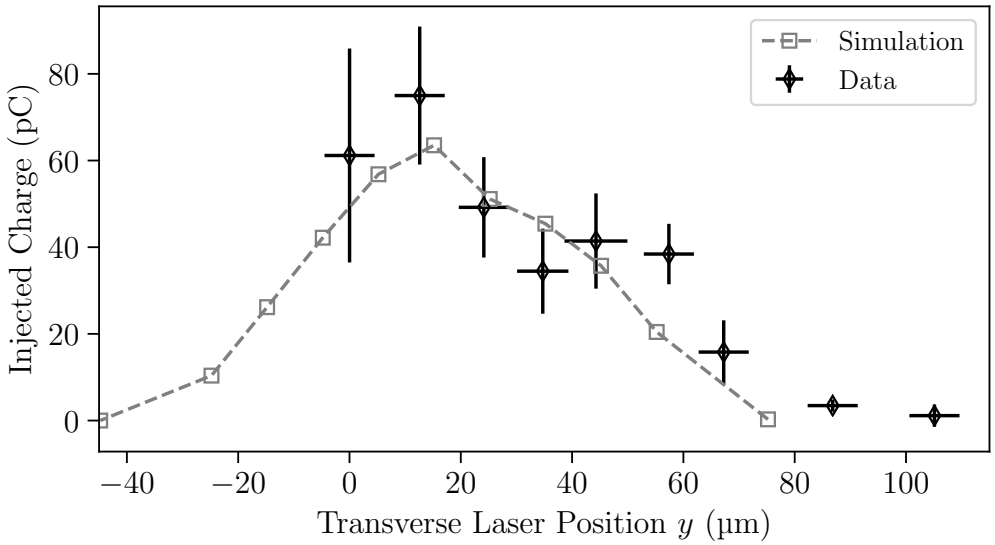

Figure 5.11: The injected charge as a function of the focal-spot position. Experimental data is plotted in black with error bars; a simulation scan is plotted in grey. The relative offset between the two datasets was optimised during the analysis process.

5.2.5 Laser Energy

The injection and acceleration process is, naturally, highly dependent on the shape of the plasma in which it takes place. This necessitates the examination of the ionisation process and the properties of the laser pulses that drive it. To this end, the total energy of both laser pulses was adjusted using the wave-plate attenuator introduced in Section 3.3, which is positioned after the the last amplifier. The attenuator was able to vary the total laser energy between 42 and $821\,\mathrm{mJ}$ on a scale of $0\,\%$ to $100\,\%$ with increasing percentages corresponding to higher energies. It was not possible to scan the energy of each laser arm independently.

The laser energy was scanned between the 0 and $60\,\%$ settings of the laser attenuator, at which point injection ceased to occur. The cessation of injection at higher laser energies was initially attributed to a combination of B-Integral effects in the transverse-laser and the onset of helium ionisation by the longitudinal laser. The B-integral effects include the distortion of the temporal pulse shape and self focusing, resulting in the focal plane being shifted further away from the electron-beam axis, as seen in Section 3.4.4.

The charge-normalised ESPEC traces are plotted as a waterfall plot in Figure 5.12; the electron-beam properties over the course of the scan are shown in Figure 5.13;. As the laser energy increased, the mean witness-beam energy is seen to increase in both figures from 40 to $80\,\mathrm{MeV}$. The injected charge peaked at approximately $40\,\mathrm{pC}$ before decreasing due to the the aforementioned effects. The rms energy spread was relatively stable at $(2.14 \pm 0.32)\,\mathrm{MeV}$, with some increase in the statistical uncertainty arising as a result of the reduced charge compared to the beginning of the scan.

The impact of increased laser energy on the witness-beam energy may be understood by considering the effect on the longitudinal plasma profile. Here we assume that an increase in the on-target laser energy leads to an increased ionisation of the second level of argon and therefore a higher plasma density and a stronger accelerating field. Practically, this is carried out using the data from Figure 3.7 to model the effect of laser energy on the intensity and resulting ionisation rate. In this model, the on-target laser energy was scanned over a range between 20 and $125\,\mathrm{mJ}$ with a FWHM pulse length of $50\,\mathrm{fs}$. At each step, the laser intensity was calculated using raw data from Figure 3.7. These intensity values were then used to calculate the expected ionisation of the first two levels of argon, and helium. The resulting plasma densities as a fraction of n_0 are shown in Figure 5.14. The accelerating field was assumed to

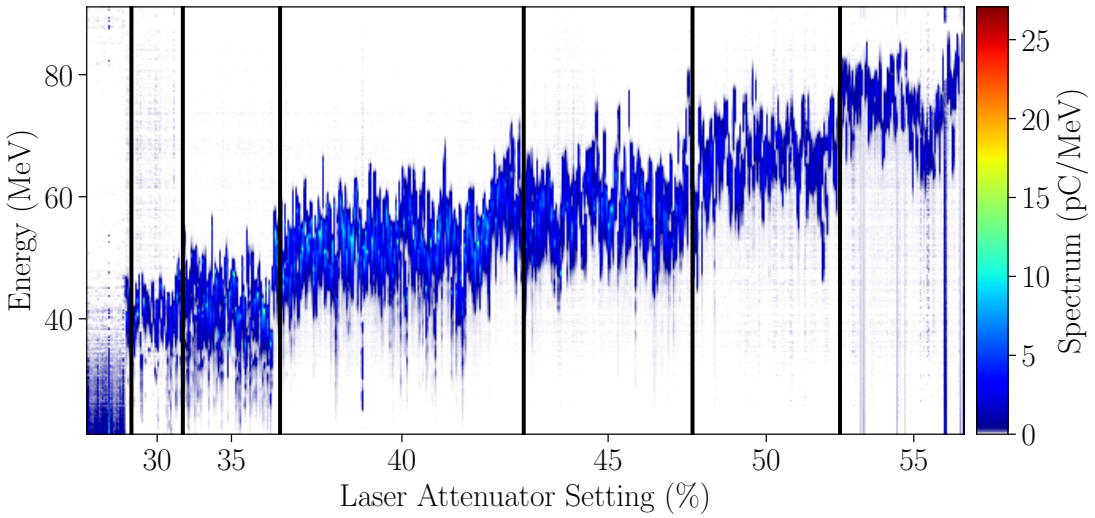

Figure 5.12: The witness-beam Espec traces as a function of the laser attenuator setting.

be a fraction η of the wave-breaking field which is given by $E_{WB} = c\sqrt{m_e n_e/\epsilon_0}$ [32]. The resulting witness-beam energy $\mathcal{E}$ is then given by

$$\mathcal{E} = eL_{acc}\eta E_{WB} = ceL_{acc}\eta\sqrt{\frac{m_e(n_e + n_f)}{\epsilon_0}}, \tag{5.2}$$

where n_f is an additional fitting parameter which accounts for differences between the calculated and actual plasma densities along the acceleration length L_{acc}, which was assumed to be 30 mm.

In Figure 5.15, this model has been fitted to the data of Figure 5.13 (a), demonstrating a good agreement between the model and the data. The fitted parameters converged on the values $n_f = -0.641 \times 10^{16}\,\mathrm{cm}^{-3}$ and $\eta = 0.218$. Both of these parameters indicate that the average plasma density is lower than expected and that the acceleration of the witness-beam occurs over a reduced acceleration length. In this model, helium was ionised to a maximum ratio of 0.15, indicating that the cessation of injection at higher laser energies most likely originates from B-Integral effects as shown by the behaviour of the transverse plasma in Section 3.4.4, rather than the ionisation of helium by the longitudinal laser. The deviation of the plasma from its previously assumed flat-top profile will be explored through the mechanism of ionisation defocusing in the Section 5.4.

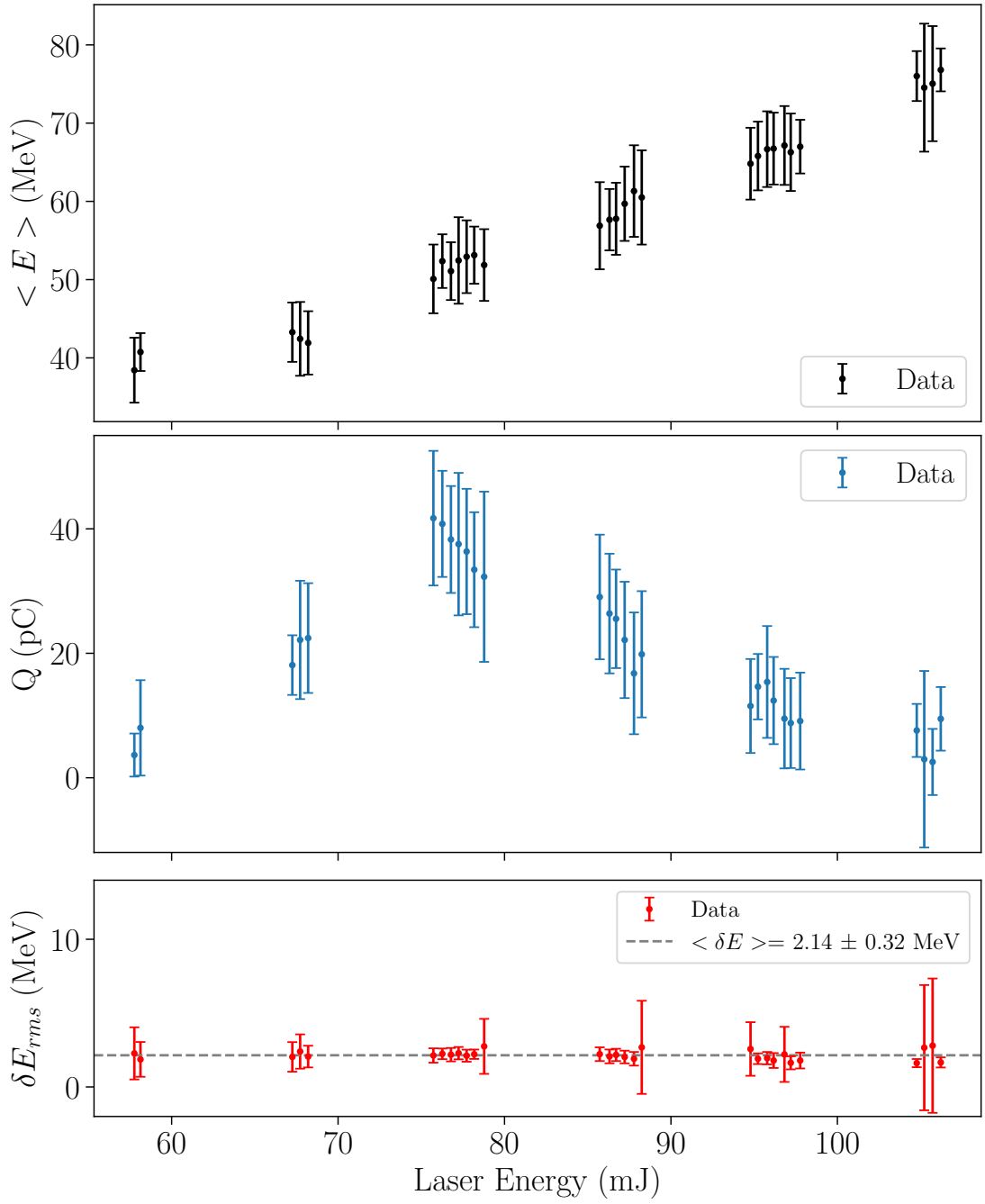

Figure 5.13: The witness-beam properties (a) mean energy, (b) charge and (c) energy spread over the laser energy scan

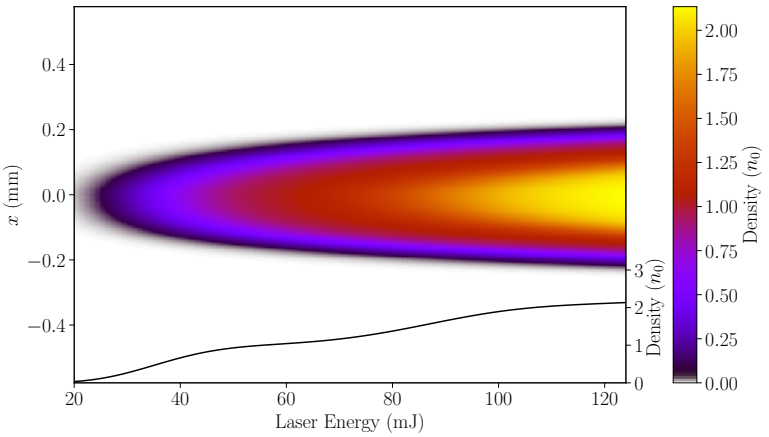

Figure 5.14: The expected longitudinal plasma density as a function of on-target laser energy. The densities have been calculated using the intensity distribution in Figure 3.7 and the ADK formula. The line-out in black represents the central on-axis density.

It is important to note that the performance of the fit shown in Figure 5.15 and the resulting chi-squared of 6.51 leaves much to be desired. As shown in Figure 5.12 there is a large spread in the energy of the injected witness-beams for the same attenuator settings. Even accounting for the effect of laser power fluctuations using the up-stream laser diagnostic cameras, it is clear that other effects are present and have a strong influence on the injection and acceleration of the witness beams resulting in the large uncertainties shown in Figure 5.15. Further work is therefore required to stabilise the injection process in order to produce higher quality data which is better suited to these analyses.

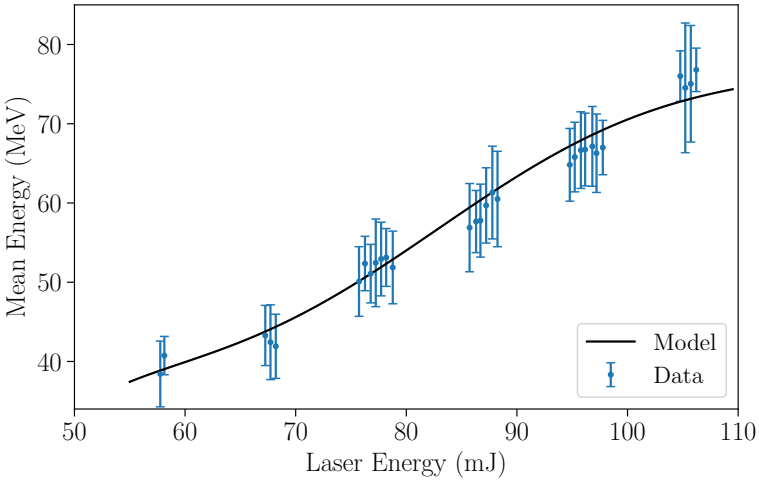

Figure 5.15: The mean witness-beam energy fitted to the model described by Equation 5.2. The performance of the fit is poor with a X^2 of 6.51 due to the large errors on the values of mean energy. See text for further details.

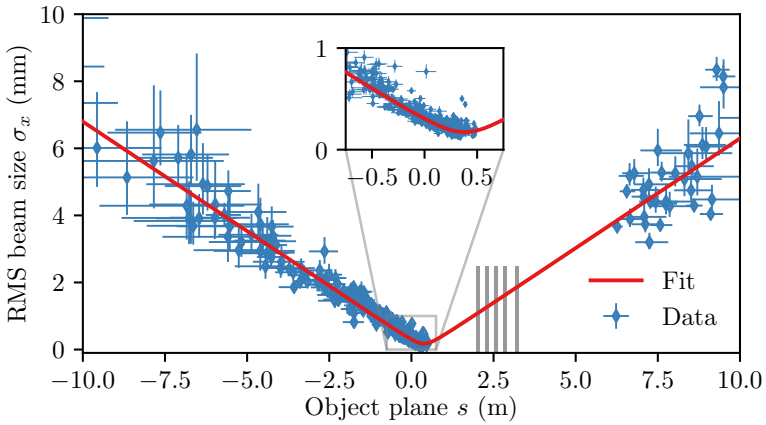

Figure 5.16: A scan of the object plane of the quadrupoles. Analysis and data courtesy of C.A Lindstroem.

5.3 Witness-beam emittance measurement

As discussed in Section 2.5.1, the transverse beam size, σ_x, and divergence, σ'_x, of an electron-beam will evolve in accordance with the transfer matrix of the beam-line,

$$\begin{pmatrix} \sigma_x \\ \sigma'_x \end{pmatrix}_s = \begin{pmatrix} R_{11} & R_{12} \\ R_{21} & R_{22} \end{pmatrix} \begin{pmatrix} \sigma_x \\ \sigma'_x \end{pmatrix}_0 . \tag{5.3}$$

The divergence of the beam σ'_x is typically not a quantity that can be measured by a single diagnostic. Therefore it is typically determined from the beam size and the transfer-matrix elements,

$$\sigma_x(s) = R_{11}(s)\sigma_x(0) + R_{12}(s)\sigma'_x(0). \tag{5.4}$$

Depending on the beam-line, the elements of the transverse matrix R_{ij} are often dependent on both the energy of the beam as well as the longitudinal position s. For a set of quadrupoles such as those directly before the electron spectrometer of FLASHForward, it is possible to image an object plane s_{obj}. This is achieved with direct mapping of transverse position between the initial plane and the plane of the spectrometer, which is achieved when $R_{12}(s)$ is identically zero. In this case the value of $R_{11}(s = s_{obj})$ is then known as the magnification.

In order to optimise the imaging of the witness-beams, the strength of the quadrupoles was adjusted over a wide range. This, along with the jitter seen in their energies, resulted in a large range of object planes being imaged. The transfer matrix for any individual shot was determined from the quadrupole strengths and the mean energy of the beam measured on

the spectrometer screen. From the transfer matrix, the object plane could then be determined by finding the value of s_{obj} for which $R_{12} \to 0$. The value of $R_{11}(s = s_{obj})$ was then used to calculate the transverse beam size at the resulting object plane.

In Figure 5.16, the transverse size of the witness-beam at the object plane s has been plotted as a function of the the object-plane position. Both the horizontal and vertical error bars are dominated by the energy spread of the electron-beam. In the case of the object-plane scan, the RMS energy spread yielded an error in the position of the object plane itself, whereas in the vertical case, it resulted in uncertainty in the value of the magnification R_{11}. The data points have been fitted with Equation 5.5, which describes the evolution of the transverse beam size in the absence of any focusing forces for a beam of normalised emittance, $\varepsilon_{x,n}$, mean Lorentz factor $\langle\gamma\rangle$ and beta function of β_0. The witness-beam will expand from its virtual source point s_0 which was expected to correspond to the exit of the plasma:

$$\sigma_x(s) = \sqrt{\frac{\varepsilon_{x,n}}{\langle\gamma\rangle}\left(\beta_0 + \frac{(s - s_0)^2}{\beta_0}\right)}. \tag{5.5}$$

The normalised emittance was calculated to be $(9.3 \pm 0.3)\,\mu\mathrm{m}$ over the 589 shots in this dataset, with the beam waist s_0 located $(381 \pm 6)\,\mathrm{mm}$ down-stream of the capillary exit at $s = 0$. The position of this waist provides an indication that the plasma may continue for some distance outside the capillary. The chamber was at an ambient pressure of $0.0031\,\mathrm{mbar}$ which may correspond to a plasma with densities on the order of $10^{13}\,\mathrm{cm}^{-3}$ assuming the laser remains sufficiently intense to continue ionising. The emittance, at $(9.3 \pm 0.3)\,\mu\mathrm{m}$ is also significantly higher than the value predicted in simulation. It should be noted that many of the shots in Figure 5.4 show transverse offsets and bunching of the energy slices in the witness-beam. This is indicative of transverse oscillations occurring during the acceleration process. These oscillations could result from the hosing instability [115] and may be seeded by transverse offsets in the driver beam or betatron oscillations of the bunch electrons [116]. Mitigation strategies for this instability include the optimisation of the driver-beam phase space [117] as well as taking steps to reduce any transverse offsets present in the driver beam. The later method has been successfully trialled at FLASHForward over the course of 2020 and was used to optimise the acceleration of an externally injected witness beam [118]. It is expected that a similarly optimised driver bunch will yield a significant improvement in the properties of an internally injected witness-beam.

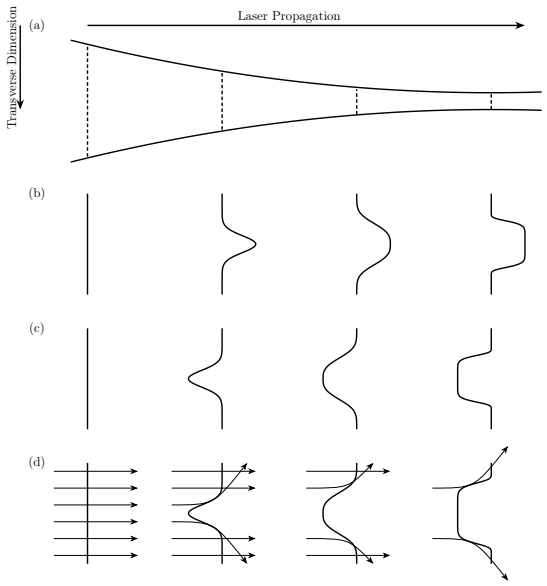

Figure 5.17: Schematic of ionisation defocusing as the laser (a) focuses and begins to ionise the gas producing a plasma on-axis (b) which will have a radial dependent refractive index as shown in (c) which results in the refraction of the laser pulse away from the axis (d). Adapted from [94]

5.4 Effects of ionisation defocusing and optimisation of the acceleration process

The witness-beam energies described in Section 5.2 are notably lower than the expected energies detailed in Chapter 4. The simulations presented in Section 4.4, when run over the full acceleration length of the capillary (30 mm) produced witness-beams with energies well in excess of 100 MeV. The design study and these investigatory simulations both assumed a flat-top background plasma profile with a constant density defined by the gas pressure extending over the complete length of the capillary. The lower energies of the witness-beams suggests a significant deviation from this assumption.

One such explanation for this discrepancy could be the defocusing of the laser due to the plasma it ionises, also known as ionisation defocusing [94]. For an electromagnetic wave of angular frequency ω, a plasma will have a refractive index that scales with its density according

to,

$$\begin{aligned} n_r &= \sqrt{1 - \frac{\omega_p^2}{\omega^2}} \\ &= \sqrt{1 - \frac{n_e}{n_c}} \end{aligned} \tag{5.6}$$

where ω_p is the plasma frequency, n_e the electron density and n_c the critical density corresponding to the frequency of the light ω ($n_c = 1.745 \times 10^{21}\,\mathrm{cm}^{-3}$ for $800\,\mathrm{nm}$ light). A schematic example of ionisation defocusing is shown in Figure 5.17. As the laser focuses, the intensity increases on axis and starts to ionise the gas in the capillary. However, as the gas is not fully ionised, a gradient occurs in the plasma density which results in a plasma with a transversely non-uniform refractive index - otherwise known as a lens. This lens defocuses the beam resulting, in a reduced on-axis intensity compared to the in-vacuum maximum and therefore a significantly reduced maximum plasma density.

Simulations were performed in FB-PIC[1] to investigate the significance of this effect. In these simulations, a Gaussian laser pulse with a $350\,\mu\mathrm{m}$ FWHM spot size and $35\,\mathrm{fs}$ FWHM pulse length was incident into an argon-filled capillary. The intensity and gas density were scanned over a range of experimentally realistic values. For the laser intensity, this was between 4 and $8 \times 10^{14}\,\mathrm{W\,cm}^{-2}$ with gas densities between 1 and $4 \times 10^{16}\,\mathrm{cm}^{-3}$. The plasmas ionised by the laser pulse at these intensities and densities are shown in Figure 5.18. The plasma generated is far from the assumed flat-top profile for a large part of the scan, and, in the extreme case drops by a factor of two over the length of the capillary.

The impact of a decrease in plasma density as a result of ionisation defocusing was investigated using a further series of OSIRIS simulations[2]. Because the exact gas density and laser intensity during the experimental run are unknown, the simulations were performed with semi-arbitrary profiles where the density was set to the nominal value of $1 \times 10^{16}\,\mathrm{cm}^{-3}$ and then ramped down immediately following injection. These simulations showed a significant decrease in the witness-beam energy, reducing to a minimum value of $(51.5 \pm 4.6)\,\mathrm{MeV}$, which is consistent with the energy of the experimental witness-beams at $(45.58 \pm 4.93)\,\mathrm{MeV}$.

[1] FB-PIC which simulates in a cylindrically symmetric, Lorentz-boosted frame, was significantly better suited in terms of its efficiency to performing simulations of laser propagation.

[2] The simulation of injection on a non-cylindrically-symmetric down-ramp requires full 3D geometry, therefore necessitating the use of OSIRIS, a fully 3D PIC code.

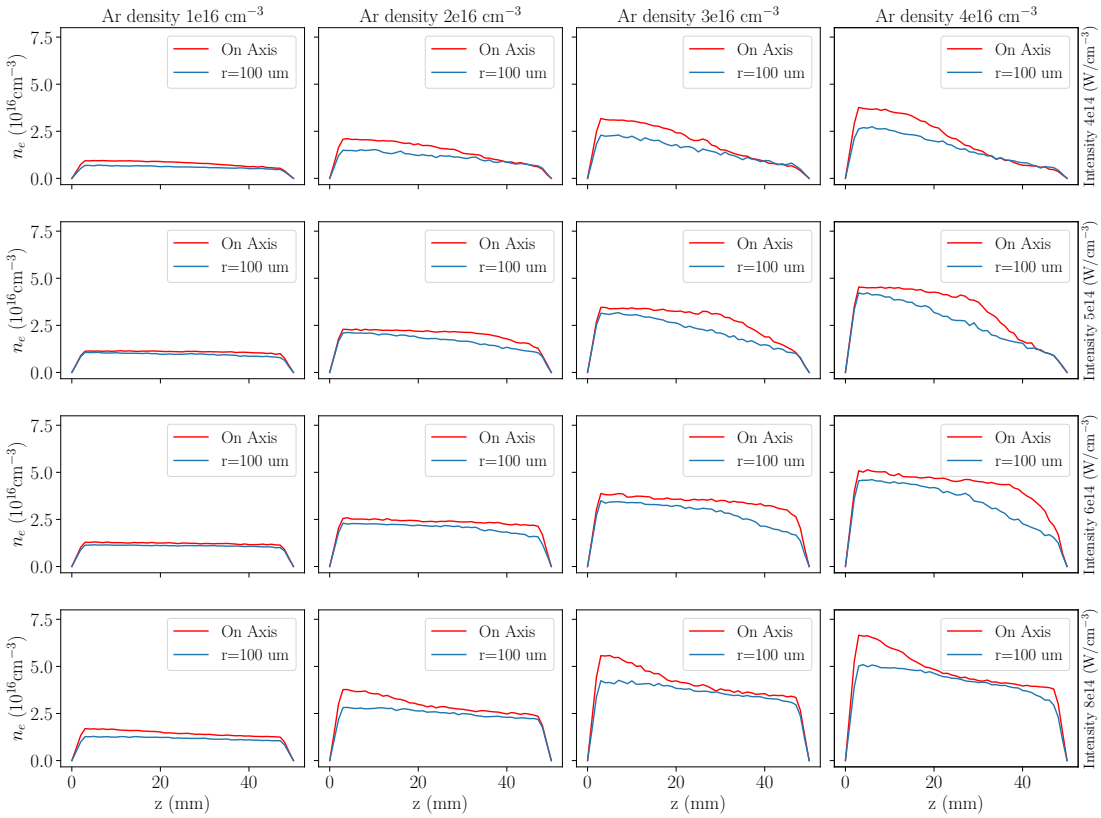

Figure 5.18: Lineouts of the axial (red) and off-axis (at a radius of 100 μm) plasma densities in argon

In an argon plasma, due to its valence electrons, small intensity fluctuations and irregularities are likely to induce low-level ionisation of the upper levels, leading to further ionisation defocusing. This will pose a challenge to the realisation of a flat-top plasma-density profile with argon as it may be difficult to find an operating range in which such a profile may be achieved. While some simulations in Figure 5.18 do show flat-top-like profiles, the experimental measurement of such laser-ionised plasmas at these densities has been notoriously difficult [119] and an online diagnostic to monitor the plasma density would be necessary to achieve such a profile with certainty, an exercise which is well beyond the scope of this work. At FLASHForward, one of the goals is the demonstration of injection and acceleration of a witness-beam in the $195\,\mathrm{mm}$ capillary target with an extended acceleration length of $175\,\mathrm{mm}$. This will be dependent upon the realisation of an optimum plasma-density profile for acceleration.

As the profiles produced in argon do not appear to be optimal, further simulations were performed in FBPIC using atomic hydrogen in place of argon. The results of these are shown in Figure 5.19. In Figure 5.20, the average density along the acceleration region (from the point of injection to the end of the cell) is compared with (a) a $50\,\mathrm{mm}$ argon plasma (b) a $50\,\mathrm{mm}$ hydrogen plasma and (c) a $195\,\mathrm{mm}$ hydrogen plasma. Together these results show that hydrogen is the favoured gas for operation in the shorter $50\,\mathrm{mm}$ capillary as the ionisation saturates at much lower intensities and is flat above intensities of $4 \times 10^{14}\,\mathrm{W\,cm^{-2}}$. In the longer $195\,\mathrm{mm}$ capillary, the ionisation has yet to saturate along the full length of the capillary. However, the average plasma density is still shown to increase with gas density. As shown in Figure 5.18, a plasma extending over the full length of the capillary was only achieved in one out of sixteen simulations. The remaining simulations show an acceleration length that depends on the gas density and the laser intensity. While hydrogen is likely to be favourable for demonstrating injection and acceleration in the long cell, understanding the density and length of the plasma profile is critical to understanding and modelling the acceleration process. Online diagnostics of the plasma are therefore likely to be important in understanding this acceleration process.

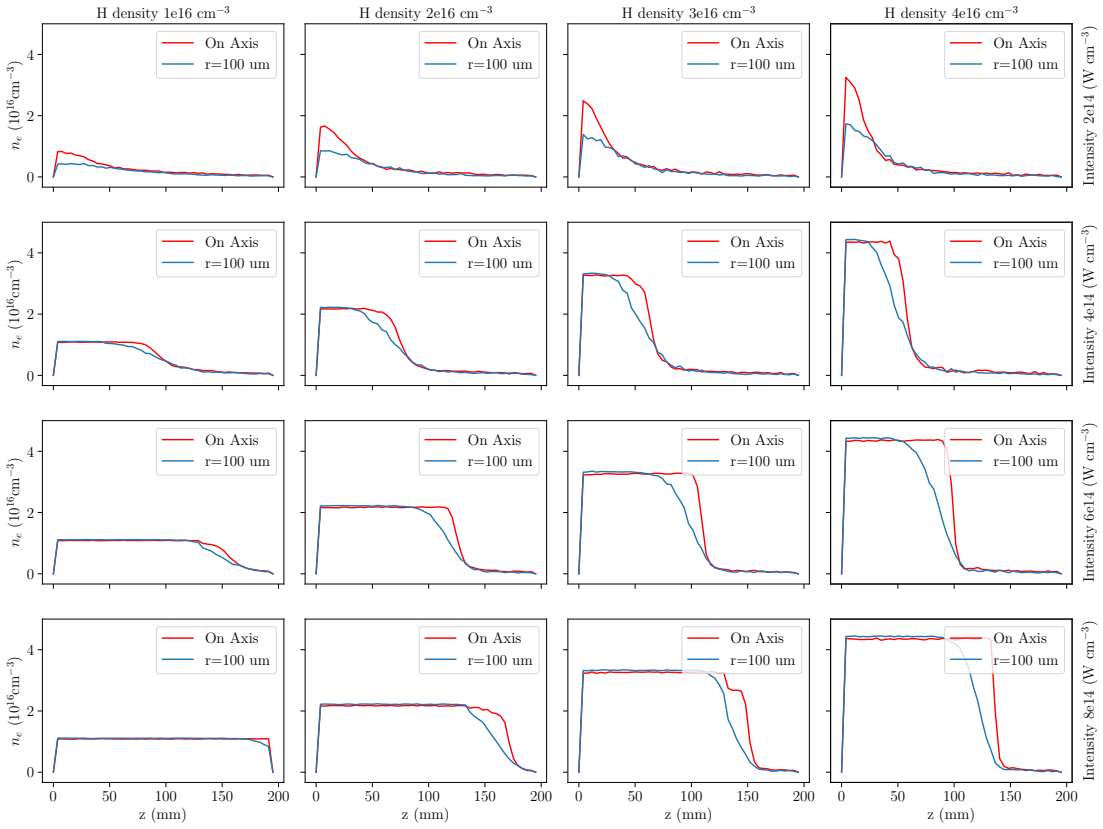

Figure 5.19: Lineouts of the axial (red) and off-axis (at a radius of 100 μm) plasma densities in hydrogen

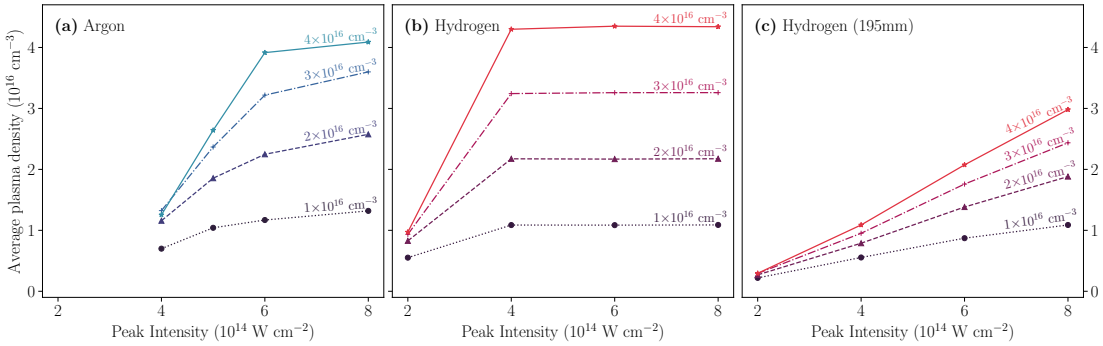

Figure 5.20: The average plasma density along the acceleration length of the plasma cell (after the injection point) as a function of peak laser intensity for four different gas densities (coloured lines) for (a) 50 mm argon plasma (b) 50 mm hydrogen plasma and (c) 195 mm hydrogen plasma.

5.4.1 Implications of ionisation defocusing on the model for laser energy

In Section 5.2.5, a model was derived to describe the effect of laser energy on the witness-beam energy. The model assumed the density profile to be a flat top with density increasing as a function of laser energy. However, as discussed previously, this is unlikely to be realistic. Instead the effect of increasing laser energy likely results in an increase in the density and the overall acceleration length. This is explored in Figure 5.21, where the plasma densities plotted in Figures 5.18 & 5.19 have been used with the model derived in Section 5.2.5 to calculate the expected witness-beam energy. Here only the η value of 0.218 was used, as it was not necessary to use the n_f term to account for the shift from a flat-top plasma such that the energy is given by

$$\mathcal{E} = \eta e L_{acc} E_{WB} = \eta c e \sqrt{\frac{m_e}{\epsilon_0}} \sqrt{\int_{z_{inj}}^{z_1} n_e(z) \mathrm{d}z}, \tag{5.7}$$

where the integral was calculated using the on-axis densities (Fig. 5.18) after the injection point at $20\,\mathrm{mm}$ and trapezoidal integration. This simplistic model assumes a fixed phase of the witness-beam with respect to the wake such that it experiences the same fraction of E_{wb} as an accelerating field.

Figure 5.21(a) shows the expected change in witness-beam energy during a scan of laser energy in a $50\,\mathrm{mm}$ argon plasma. The behaviour is qualitatively similar to that shown in Section 5.2.5. Figure 5.21 (b) & (c) then show the same analysis applied to the hydrogen plasmas at capillary lengths of $50\,\mathrm{mm}$ and $195\,\mathrm{mm}$, respectively. While the $50\,\mathrm{mm}$ hydrogen plasma does not yield an improvement on the maximum-achievable witness-beam energy, the same energies are achieved with lower values of laser intensity. Moving to the longer $195\,\mathrm{mm}$ capillary, the acceleration lengths are longer and therefore higher energies of up to $500\,\mathrm{MeV}$ may be achieved. As the plasma does not extend to the full length of the cell, saturation of the energies is not seen within the parameter space.

5.5 Conclusion

This chapter has outlined the set-up and procedures necessary to achieve the successful internal injection of electrons on a density-down-ramp into a wake-field-accelerator, a method

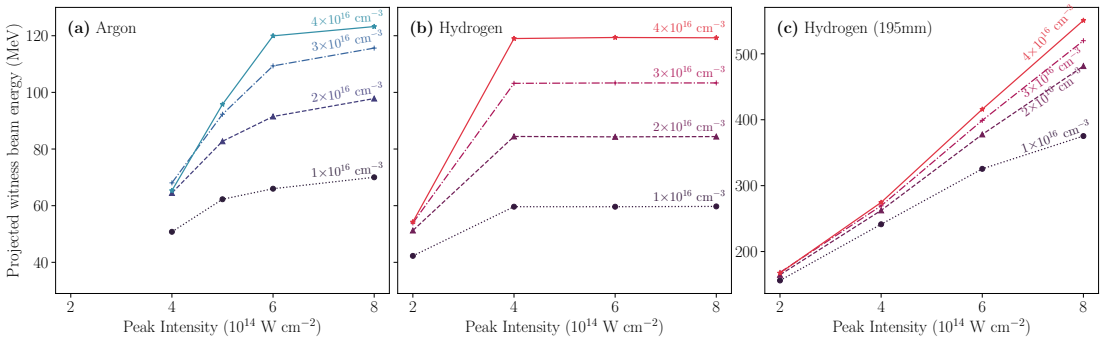

Figure 5.21: The projected witness-beam energies for the argon and hydrogen plasmas depicted in Figures 5.18 & 5.19 for (a) 50 mm argon plasma (b) 50 mm hydrogen plasma and (c) 195 mm hydrogen plasma. The energies were calculated using Equation 5.7 with an η value of 0.218

which has been shown in the literature to be capable of producing high quality beams. The data in this chapter represents the first stable realisation of laser-triggered density-down-ramp injection in a plasma-wake-field-accelerator. The stability of the injection enabled the first experimental characterisation of key properties that influence the injection process, namely the position of the transverse laser, and the state of the plasma in which the acceleration takes place. Furthermore, this chapter also presents the first emittance measurement of witness-beams injected using such a technique. The witness-beams described in this chapter represent a proof of principle and demonstrate that with a highly reliable accelerator such as FLASH such techniques are not only feasible but repeatable.

Possible improvements on these results include better alignment between the transverse laser and the electron-beam, which has been shown to be critical to the injection process. Future experiments should be carried out with an improved overlap between the beams and the initial alignment techniques presented in this chapter should be improved upon. In future experiments, an offset scan to determine the optimum overlap between the transverse beam and the laser should be carried out to first optimise the charge yield before making further measurements. On the other hand, this effect would be largely eliminated by increasing the size of the transverse plasma by a factor of 2 or more in the direction transverse to the beam-propagation axis. Such an effect could be achieved with cylindrical lenses to produce an asymmetric focus or with a symmetric focusing optic with a larger f-number to produce a larger focus and hence a longer plasma ramp. A longer ramp may also be beneficial to the injection progress. However, it is important to note that, in the design of the plasma chamber and the transverse laser arm, the focusing optic for the transverse laser is placed outside the

chamber and the pulse must be transmitted through a window in order to ionise the plasma. In order to avoid non-linear pulse distortion inside this window, the intensity at and thickness of this window must be minimised. These factors must be carefully considered when planning alterations to the experimental set up described in this work.

Section 5.4 discusses a critical issue for the set-up, namely that the argon ionisation of the longitudinal laser does not result in a flat-top density profile as had been assumed. The laser is defocused by the plasma as it starts to ionise and therefore the peak laser intensity inside the gas-filled capillary may deviate significantly from the in-vacuum maximum. The consequences for the acceleration process were significant, with the energy being reduced by a factor of two from its expected value with a flat-top profile background plasma. The use of hydrogen presents a potential route to resolving this issue in a longer capillary, but was not available for use at the time of the experimental run. The characterisation of these laser-ionised plasmas prior to the experiment or the implementation of online diagnostics should be a priority for future optimisation of the acceleration process.

6

Conclusion and outlook

This thesis demonstrates stable and reliable internal injection on a laser-triggered density-down-ramp in a plasma-wake-field accelerator for the first time. The experiment took place at the FLASHForward facility [120], which is a dedicated beam-line of the FLASH FEL [121] for the study of plasma-wake-field acceleration. This acceleration scheme uses the intense electromagnetic fields of a charged particle beam to drive wake-fields inside a plasma that yield accelerating gradients up to $10\,\mathrm{GV\,m^{-1}}$.

High-quality driver beams were extracted from the FLASH accelerator and transported to a chamber with a laser-ignited plasma in order to inject electrons into the wake-field which was formed behind the driver. A laser pulse was transported over $50\,\mathrm{m}$ from a second-floor laser lab before being split into two. These two pulses were focused into the target chamber using optical systems designed to produce a plasma with the required properties for injection, as determined by simulations. The pulses were precisely overlapped in time and space in order to preshape the plasma $20\,\mathrm{ps}$ prior to the arrival of the electron beam.

Following interaction of the electron beam with the plasma, injection was seen in 98% of all shots over a $15\,\mathrm{min}$ period with a mean charge of $(36.1 \pm 9.4)\,\mathrm{pC}$ and an energy of $(45.58 \pm 4.93)\,\mathrm{MeV}$. The stable injection enabled the characterisation of the emittance of

the beams at $(9.3 \pm 0.3)\,\mu\mathrm{m}$. Further measurements were made to determine the impact of the offset of the electron beam with respect to the plasma and the energy of the laser. The investigation into these effects was also augmented with further simulations based upon the conditions realised during the experimental campaign.

There are a number of challenges that limit the performance of the injection technique. These include the intrinsic mismatch between the shape of the plasma filament in the two transverse planes, which result in asymmetrical emittance in the transverse planes. Another issue is that the technique is highly sensitive to the alignment of the laser and electron beams, resulting in large jitter effects from, for example, pointing jitter in the transverse laser arm. A larger plasma filament is expected to be able to resolve both of these issues. The technique also requires laser ionisation of this background plasma, which was shown to not be able to fully ionise the plasma, leading to lower than expected witness-beam energies. Simulations utilising hydrogen as a background species indicate that the ignition of a long plasma may be significantly more feasible, due to the lower energies required. Alternative techniques may include the use of electrical discharge to ionise the plasma. As an electrical discharge is likely to result in a high degree of ionisation of the dopant species, time would have to be allowed for the recombination process to occur prior the arrival of the transverse laser. However, the peak density of the plasma filament may be limited resulting in a probably reduction in the charge available for injection.

This work documents a critical step towards the optimisation of density-down-ramp injection. The stable electron-injection described in this thesis will allow optimisation to be carried out over subsequent experimental campaigns.

A

Further Gaussian Beam Optics

A.1 Complex radius of curvature

In Equation A.1, Equation 2.23 is rewritten in terms of the complex radius of curvature $q(z)$ which is defined in Equation A.2,

$$\vec{E}(r,z) \propto \exp\left\{\left(-i\frac{kr^2}{2q(z)}\right)\right\} \tag{A.1}$$

$$\frac{1}{q(z)} = \frac{1}{R(z)} - \frac{i\lambda}{n\pi w(z)^2} \tag{A.2}$$

The $q(z)$ parameter is an important parameter as it contains both the wave front curvature and the spot size. Critically, it may also be shown that $q(z)$ varies according to the Ray-Transfer Matrix of the optical system which the beam is propagating through.

In classical ray optics, the relation between the Ray's initial position and divergence $\binom{x_i}{x_i'}$ and the final position and divergence $\binom{x_f}{x_f'}$ following propagation through an arbitrary optic

Definition	w_0	σ_I	σ_E
$FWHM$	$w_0 = \frac{FWHM}{\sqrt{2\ln 2}} = 0.849FWHM$	$\sigma_I = \frac{FWHM}{2\sqrt{2\ln 2}} = \frac{FWHM}{2.355} = 0.425FWHM$	$\sigma_E = \sqrt{2}\sigma_I = \frac{FWHM}{2\sqrt{\ln 2}} = \frac{FWHM}{1.665}$
$R_{e^{-1}}$	$w_0 = \sqrt{2}R_{e^{-1}} = 1.424R_{e^{-1}}$	$\sigma = \frac{R_{e^{-1}}}{\sqrt{2}} = 0.707R_{e^{-1}}$	
$R_{e^{-2}}$	$w_0 = R_{e^{-2}}$	$\sigma = \frac{R_{e^{-2}}}{2} = 0.5R_{e^{-2}}$	
$D_{e^{-1}}$	$w_0 = \frac{D_{e^{-1}}}{\sqrt{2}} = 0.707D_{e^{-1}}$	$\sigma = \frac{D_{e^{-1}}}{2\sqrt{2}} = 0.354D_{e^{-1}}$	
$D_{e^{-2}}$	$w_0 = \frac{D_{e^{-2}}}{2} = 0.5D_{e^{-2}}$	$\sigma = \frac{D_{e^{-2}}}{4} = 0.25$	

Table A.1: Table of further conversions table between various beam size definitions of a Gaussian laser beam and the parameters, w_0 and σ_t and σ_E

system is given by Equation A.3,

$$\begin{pmatrix} x_f \\ x'_f \end{pmatrix} = \begin{bmatrix} A & B \\ C & D \end{bmatrix} \cdot \begin{pmatrix} x_i \\ x'_i \end{pmatrix}, \tag{A.3}$$

, The central matrix is commonly known as the $ABCD$ matrix and is the product of the matrices of each optical element of the optical system. When applied to the $q(z)$ parameter, the transformation is as stated in Equations A.4 and A.5,

$$q_2 = \frac{Aq_0 + B}{Cq_0 + D} \tag{A.4}$$

or

$$\frac{1}{q_2} = \frac{C + \frac{D}{q_0}}{A + \frac{B}{q_0}} \tag{A.5}$$

A.2 Defocusing zernike polynomial

The 'defocus' Zernike Polynomial is given by $(n, m) = (2, 0)$

$$Z_2^0 = 2r^2 - 1 \tag{A.6}$$

Some definitions include a factor of $\sqrt{3}$, which is neglected here in order to simplify the mathematics

The phase term for a Zernike polynomial is given by

$$\phi_{Z_n^m} = \exp\{(-ikAZ_n^m(r, \theta))\} \tag{A.7}$$

$$\phi_{Z_2^0} = \exp\big\{(-ikA(2r^2 - 1))\big\} \tag{A.8}$$

where A is an arbitrary amplitude of the Zernike aberation

Substituting this in to the electric field formula, we obtain $E = E_0\phi_{Z_2^0}$

$$\vec{E}(r,z) \propto \exp\left\{\left(-i\frac{kr^2}{2}\left(\frac{1}{R(z)} - \frac{i\lambda}{n\pi w(z)^2}\right)\right)\exp\{(-ikA(2r^2-1)\}\right\} \tag{A.9}$$

$$\vec{E}(r,z) \propto \exp\left\{\left(-i\frac{kr^2}{2}\left(\frac{1}{R(z)} - \frac{i\lambda}{n\pi w(z)^2}\right)\right)\right\}\exp\left\{\left(-i\frac{4kAr^2}{2}\right)\right\}e^{iAk} \tag{A.10}$$

Dropping the constant phase factor,

$$\vec{E}(r,z) \propto \exp\left\{\left(-i\frac{kr^2}{2}\left(4A + \frac{1}{R(z)} - \frac{i\lambda}{n\pi w(z)^2}\right)\right)\right\} \tag{A.11}$$

The $q(z)$ paremeter is now written as

$$\frac{1}{q'(z)} = 4A + \frac{1}{q(z)} = 4A + \frac{1}{R(z)} - \frac{i\lambda}{n\pi w(z)^2} \tag{A.12}$$

Now the case of a collimated beam is considered. In this case for $z = 0$, $R(z) = \infty$, and writing the Rayleigh length as $z_r = \frac{\pi n w_0^2}{\lambda}$ thus

$$\frac{1}{q'_0} = 4A + \frac{1}{q'_0} = 4A - iz_r^{-1} \tag{A.13}$$

Using the ABCD matrix (Eq. A.5) we find

$$\frac{1}{q'_2} = \frac{4A - \frac{i}{z_r} - \frac{1}{f}}{d\left(4A - \frac{i}{z_r}\right) - \frac{d}{f} + 1} \tag{A.14}$$

$$\frac{1}{q'_2} = \frac{4Afz_r - if - z_r}{df\,(4Az_r - i) - dz_r + fz_r} \tag{A.15}$$

$$\frac{16A^2df^2z_r^2 - 8Adfz_r^2 + 4Af^2z_r^2 + df^2 + dz_r^2 - fz_r^2}{16A^2d^2f^2z_r^2 - 8Ad^2fz_r^2 + 8Adf^2z_r^2 + d^2f^2 + d^2z_r^2 - 2dfz_r^2 + f^2z_r^2} \\ -i\frac{f^2z_r}{16A^2d^2f^2z_r^2 - 8Ad^2fz_r^2 + 8Adf^2z_r^2 + d^2f^2 + d^2z_r^2 - 2dfz_r^2 + f^2z_r^2} \tag{A.16}$$

Following the previous strategy, the location of the focus is derived by solving for $R(z) = \infty$,

$$\frac{1}{R_2} = \frac{16A^2df^2z_r^2 - 8Adfz_r^2 + 4Af^2z_r^2 + df^2 + dz_r^2 - fz_r^2}{16A^2d^2f^2z_r^2 - 8Ad^2fz_r^2 + 8Adf^2z_r^2 + d^2f^2 + d^2z_r^2 - 2dfz_r^2 + f^2z_r^2}$$

$$R_2 = \frac{16A^2d^2f^2z_r^2 - 8Ad^2fz_r^2 + 8Adf^2z_r^2 + d^2f^2 + d^2z_r^2 - 2dfz_r^2 + f^2z_r^2}{16A^2df^2z_r^2 - 8Adfz_r^2 + 4Af^2z_r^2 + df^2 + dz_r^2 - fz_r^2}$$

Hence the focus is found by the solution of

$$16A^2df^2z_r^2 - 8Adfz_r^2 + 4Af^2z_r^2 + df^2 + dz_r^2 - fz_r^2 = 0 \tag{A.17}$$

$$d = \frac{fz_r^2\left(-4Af + 1\right)}{16A^2f^2z_r^2 - 8Afz_r^2 + f^2 + z_r^2}$$

$$d = \frac{f\left(-4Af + 1\right)}{16A^2f^2 - 8Af + \frac{f^2}{z_r^2} + 1}$$

Using the previous approximation of $\frac{f}{z_{r0}} \ll 1$, where z_{r0} is the Rayleigh length of the incoming beam and for an ideally collimated beam $z_{r0} = \infty$. this will simplify to

Function	Expression
Propagation to longitudinal position d	$U' = U_0 \exp\left(\frac{ik}{2d}r^2\right)$
Focusing optic with focal length f	$U' = U_0 \exp\left(-\frac{ik}{2f}r^2\right)$
Defocusing Zernike Polynomial of amplitude A	$U' = U_0 \exp\left(ikA(2r^2-1)\right)$

Table A.2: Numerical expressions describing the electric field of the laser after propagation

$$d = -\frac{f(4Af-1)}{16A^2f^2 - 8Af + 1} = -\frac{f}{4Af-1} \simeq f(1+4Af) \tag{A.18}$$

A.2.1 Alternative derivation

A far simpler derivation of the proceeding equation, may be found using the appropriate phase terms for the propagation of a laser field through a focusing optic and to the focus. These terms are listed in Table A.2.

Combining the first two terms together for the total spatial phase added to the laser yields

$$\phi_l(r) = \frac{ik}{2d}r^2 - \frac{ik}{2f}r^2 \tag{A.19}$$

as discussed in Section 2.2.3, when the distance $z = f$ the first two terms in Equation A.19 exactly cancel and $\phi_l(r) = 0$. This can therefore be defined as a condition for the laser to be in focus. Now introducing the defocusing term yields,

$$\phi_l(r) = \frac{ik}{2d}r^2 - \frac{ik}{2f}r^2 + ikA(2r^2-1) \tag{A.20}$$

the previous condition of $\phi_l(r) = 0$ can now be applied to find the focusing position by solving for d for an arbitrary defocus amplitude A

$$\frac{ik}{2d}r^2 - \frac{ik}{2f}r^2 + ikA(2r^2-1) = 0 \tag{A.21}$$

, dropping the constant factor of -A and dividing through by ikr^2,

$$\frac{1}{2d} - \frac{1}{2f} + 2A = 0 \tag{A.22}$$

$$\frac{1}{f} - 4A = \frac{1}{d} \tag{A.23}$$

$$d - 4Afd = f \tag{A.24}$$

$$d(1 - 4Af) = f \tag{A.25}$$

$$d = \frac{f}{(1 - 4Af)} \simeq f(1 + 4Af) \tag{A.26}$$

This second method derivation yields an identical result to Equation A.18, while being significantly more straightforward. The first derivation relied heavily on the symbolic mathematics package SymPy [122], while the second could be done trivially by hand. Both are included for matters of interest.

B

Evaluation of surplus beam line change

The charge of the witness beams was determined with four beam charge diagnostics along the beam-line and the Espec LANEX screen. Two BPMs and one toroidal charge monitor (Toroid) measure the total charge in the beam-line prior to the plasma chamber, with an additional one measuring the charge directly after. The integrated light yield from the low energy LANEX screen was expected to be be directly correlated to the witness beam charge. Further details relating to these diagnostics are listed in Table B.1. Any excess charge present in the beam-line after the target chamber was assumed to be as a result of injection. However as some charge loss from the driver is expected to occur during its interaction with the plasma, this is not a straightforward measurement. The calibration was carried out by progressively turning on and off the injection by inserting the transverse beam block (shown in Figure 3.8) into the path of the transverse laser. The corresponding traces on the low energy electron spectrometer screen are shown in Figure 5.5, while the charge measured by the post-plasma BPM (1FLFDIAG) during this scan is plotted in Figure B.1. There is a clear absence of signal on the Spectrometer while the laser is blocked ("OFF") and the mean of the charge distribution is seen to shift from (749.52 ± 5.41) pC to (783.4 ± 8.7) pC when the injection laser is turned on. The clear separation between the two distributions is demonstrated in subplot (a), where the Gaussian fit to the distribution from subplot (b) (grey, dashed) has minimal overlap with the distribution of charge measured by the BPM.

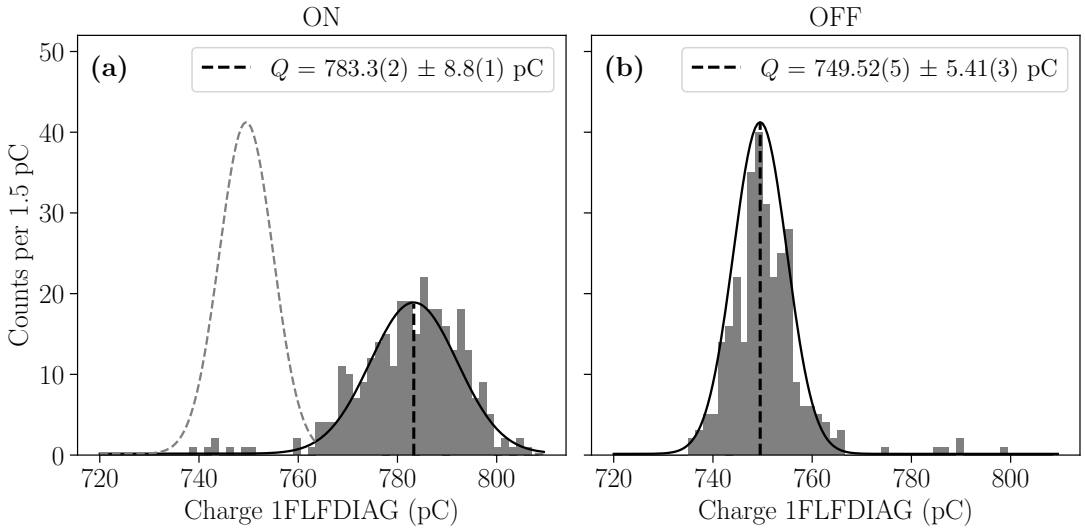

Figure B.1: The charge measured on the 1FLFDIAG BPM with the injection laser (a) turned on and (b) off , a Gaussian function has been fitted to each distribution, the mean and standard deviation are denoted in the legend of each plot with the brackets denoting the statistical uncertainty from the fit.

To extract the witness beam charge from this dataset, the charge of the driver was measured at the three pre-plasma BPMs and subtracted from the total charge measured by the post-plasma BPM. These quantities, along with the integrated signal on the electron spectrometer are plotted in Figure B.2. In Figure B.3 a linear fit is applied between the electron spectrometer signal and the charge difference between 1FLFDIAG and each of the respective pre-plasma BPMs. At low values of electron spectrometer signal, the fit performance is noticeably poorer than at higher values, it is suggested that these correspond to events where the witness beam was not fully captured by the spectrometer due the pointing of the witness beam. The y-offset of each plot is assumed to be the result of driver charge loss in the plasma, hence the witness

Name	Location	Type
7FLFMAFF	Pre-plasma	Toroidal
11FLFMAFF	Pre-plasma	BPM
14FLFMAFF	Pre-plasma	BPM
1FLFDIAG	Post-plasma	BPM
Electron Spectrometer	Post-plasma	LANEX screen imaged by a CCD camera

Table B.1: List of beam charge diagnostics considered for the charge calibration

beam charge may be calculated with the following,

$$Q_{witness} = Q_{1FLFDIAG} - Q_{7FLFMAFF} + 40.1\,\mathrm{pC}, \tag{B.1}$$

where (40.1 ± 0.2) pC is the offset from the linear fit from Figure B.3. Or by

$$Q_{witness} = Q_{1FLFDIAG} - Q_{11FLFMAFF} + 25.8\,\mathrm{pC}, \tag{B.2}$$

with an offset value of (25.8 ± 0.2) pC or by using 14FLFMAFF offset of (30.8 ± 0.8) pC by,

$$Q_{witness} = Q_{1FLFDIAG} - Q_{14FLFMAFF} + 30.78\,\mathrm{pC}. \tag{B.3}$$

These calibrations were then used to extract the witness beam charge for each diagnostic reference value, the results of which are plotted in Figure B.4. A Gaussian distribution was used to determine the mean charge of witness beams which were (32.8 ± 8.2) pC, (32.9 ± 7.8) pC and (79.1 ± 12.2) pC using 7,11 and 14 FLFMAFF BPMs respectively. When the laser was blocked the charges were measured as (-0.03 ± 6.26) pC, (0.01 ± 6.30) pC and (62 ± 16) pC respectively. The values using the 7FLFMAFF and 11FLFMAFF diagnostics as references are in remarkably good agreement. However 14FLFMAFF was positioned directly prior to the plasma chamber and shows much larger fluctuations in the shot-to-shot charge with the injection laser off as shown in Figure B.2(h) therefore its use as a reference was concluded to be unreliable for such charge measurements.

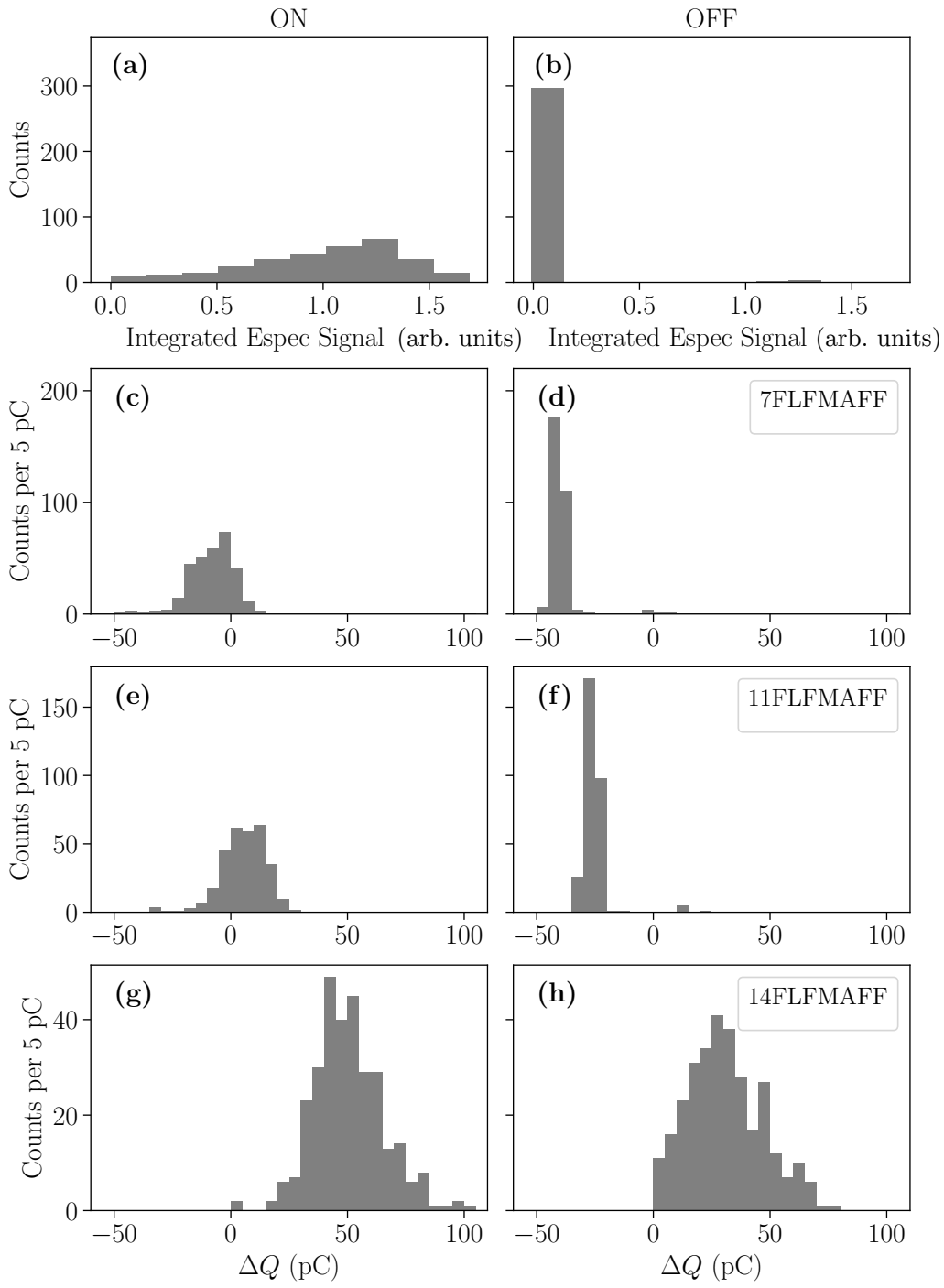

Figure B.2: Histograms of the raw witness beam charge signal when the injection laser was turned on (a,c,e,g) and turned off (d,b,f,h) from the diagnostics listed in Table B.1. (a) & (b) the integrated light yield of the electron spectrometer camera. (c) & (d) the charge at 1FLFDIAG with the charge at 7FLFMAFF subtracted, (e) & (f) same as previous using 11FLFMAFF, and (g) & (h) the same with 14FLFMAFF

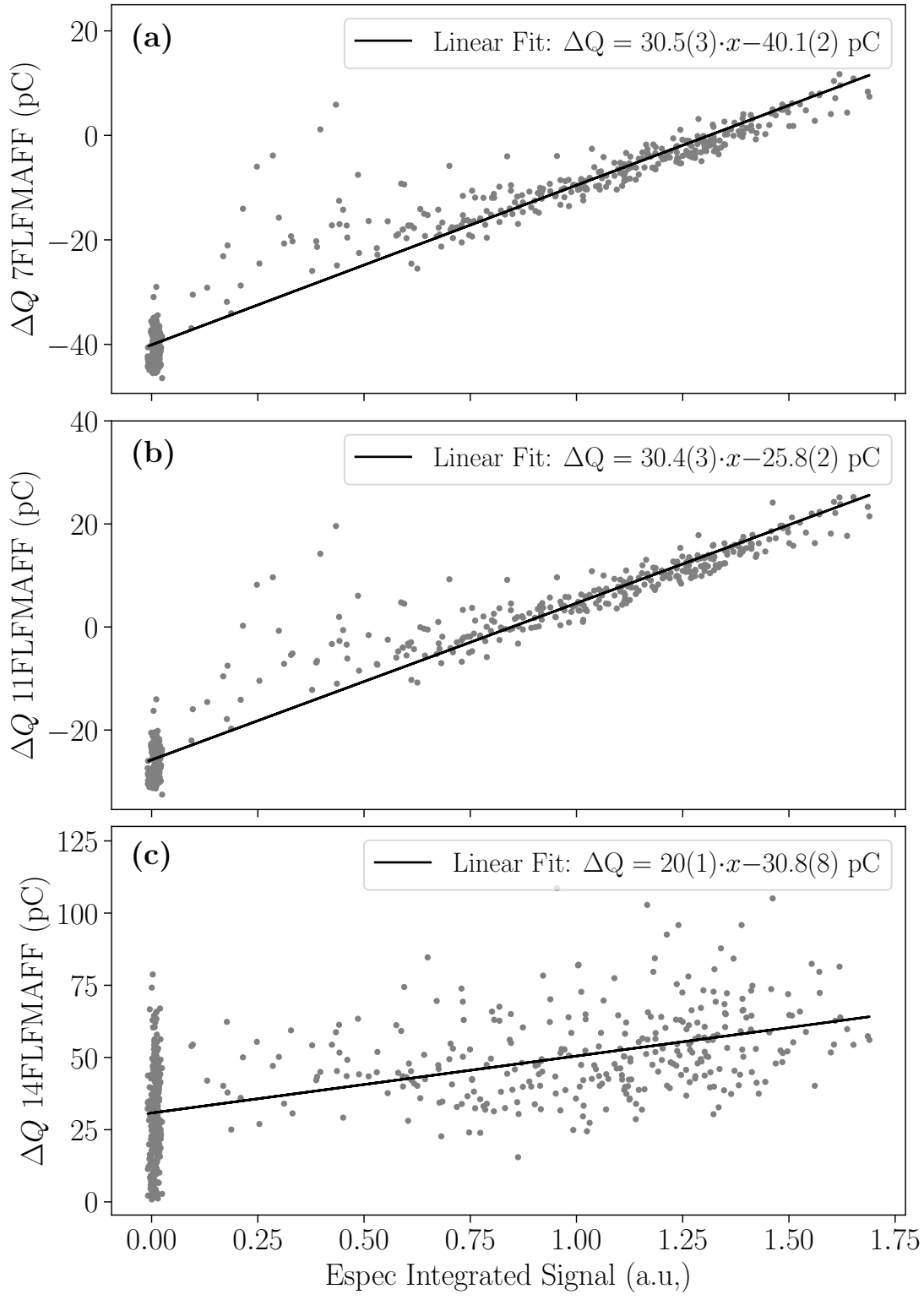

Figure B.3: Witness Beam Charge Calibration plots for the charge difference between 1FLFDIAG and 7,11, and 14-FLFMAFF charge diagnostics. Each curve is fitted. with a linear fit, the coefficients of which are marked in the legend, where the () denote the statistical uncertainty of the fit.

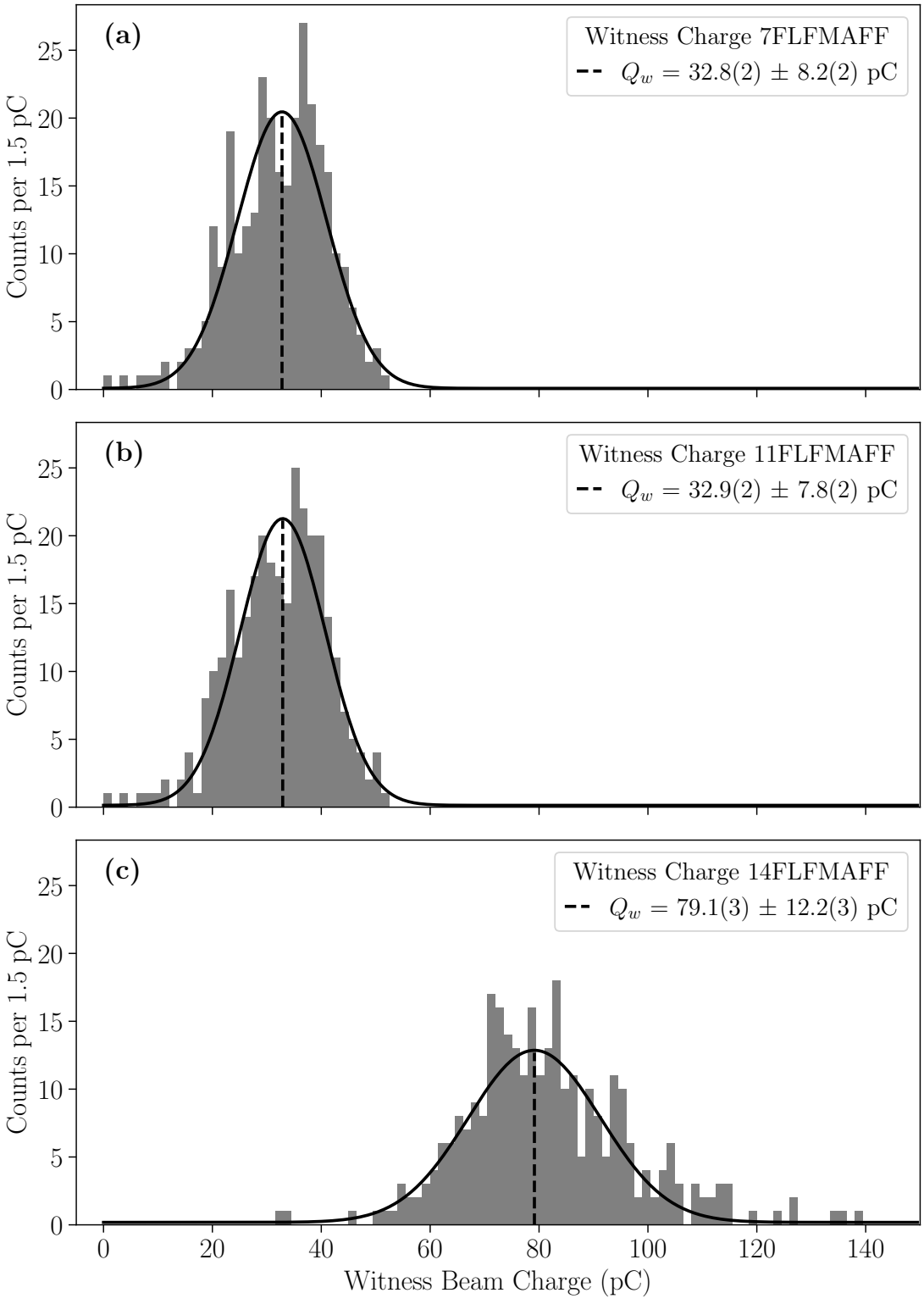

Figure B.4: Extracted witness beam charges using the calibrated offsets from Figure B.3. A Gaussian function has been fitted to each distribution, the mean and standard deviation are denoted in the legend of each plot with the brackets denoting the statistical uncertainty from the fit.

C

Further Transverse Laser Parameters

The focal spot quality can be further investigated by evaluating the so called fractional power in the bucket (PIB). This is calculated by radially integrating the profile shown in Figure 3.10a. This radial profile I_r can then be used with Equation C.1,

$$PIB(r) = \frac{\sum_0^R I_r}{\sum_0^\infty I_r} \tag{C.1}$$

to calculate the relative power enclosed within each radial bucket. This is plotted for both the simulated and measured intensity profiles in Figure C.2.

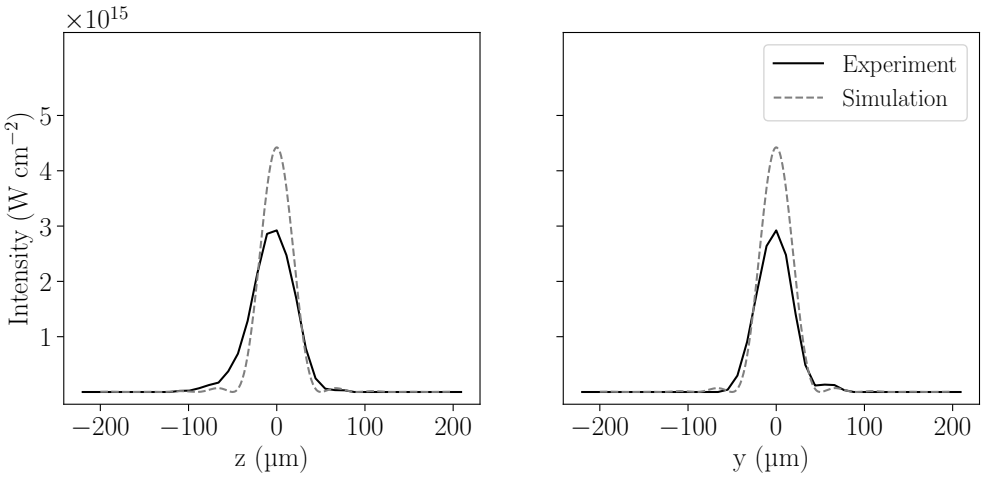

Figure C.1: A comparison between horizontal and vertical lineouts of the focal spot produced by simulation of the focusing system as described in Chapter 4 and that measured during the experiment shown in Figure 3.10

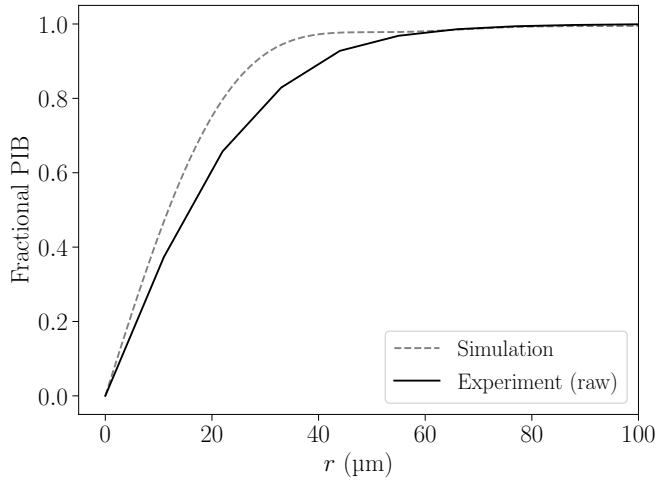

Figure C.2: Fractional PIB for both the simulated and measured focal spot profiles

Bibliography

[1] A. Canepa, "Searches for supersymmetry at the large hadron collider," *Reviews in Physics*, vol. 4, p. 100 033, 2019, ISSN: 2405-4283. DOI: https://doi.org/10.1016/j.revip.2019.100033. [Online]. Available: https://www.sciencedirect.com/science/article/pii/S2405428318300091.

[2] B. a. Abi, "Measurement of the positive muon anomalous magnetic moment to 0.46 ppm," *Phys. Rev. Lett.*, vol. 126, p. 141 801, 14 2021. DOI: 10.1103/PhysRevLett.126.141801. [Online]. Available: https://link.aps.org/doi/10.1103/PhysRevLett.126.141801.

[3] G. W. Bennett, B. Bousquet, H. N. Brown, *et al.*, "Final report of the e821 muon anomalous magnetic moment measurement at bnl," *Phys. Rev. D*, vol. 73, p. 072 003, 7 2006. DOI: 10.1103/PhysRevD.73.072003. [Online]. Available: https://link.aps.org/doi/10.1103/PhysRevD.73.072003.

[4] J. D. Jackson, *Classical Electrodynamics*, 3rd. John Wiley & Sons, Inc., 1998.

[5] S. Krinsky, M. L. Perlman, and R. E. Watson, "Characteristics of synchrotron radiation and of its sources," DOI: 10.2172/5395804. [Online]. Available: https://www.osti.gov/biblio/5395804.

[6] G. Shenoy, "Basic characteristics of synchrotron radiation," *Structural Chemistry*, vol. 14, no. 1, pp. 3–14, 2003. DOI: 10.1023/a:1021656723964.

[7] M. S. Smyth and J. H. Martin, "X ray crystallography.," eng, *Molecular pathology : MP*, vol. 53, no. 1, pp. 8–14, 2000, ISSN: 1366-8714 (Print). DOI: 10.1136/mp.53.1.8.

[8] J. Yano and V. K. Yachandra, "X-ray absorption spectroscopy," *Photosynthesis Research*, vol. 102, no. 2, p. 241, 2009, ISSN: 1573-5079. DOI: 10.1007/s11120-009-9473-8. [Online]. Available: https://doi.org/10.1007/s11120-009-9473-8.

[9] N. A. Vinokurov and E. B. Levichev, "Undulators and wigglers for the production of radiation and other applications," *Physics-Uspekhi*, vol. 58, no. 9, pp. 850–871, 2015. DOI: 10.3367/ufne.0185.201509b.0917. [Online]. Available: https://doi.org/10.3367/ufne.0185.201509b.0917.

[10] E. Weckert, K. Balewski, W. Brefeld, *et al.*, "PETRA III: A new high brilliance synchrotron radiation source at DESY," *AIP Conference Proceedings*, vol. 705, pp. 73–76, 2004, ISSN: 15517616. DOI: 10.1063/1.1757737.

[11] B. W. Mcneil and N. R. Thompson, "X-ray free-electron lasers," *Nature Photonics*, vol. 4, no. 12, pp. 814–821, 2010, ISSN: 17494885. DOI: 10.1038/nphoton.2010.239.

[12] S. Günther, P. Y. Reinke, Y. Fernández-Garciá, *et al.*, "X-ray screening identifies active site and allosteric inhibitors of SARS-CoV-2 main protease," *Science*, vol. 372, no. 6542, pp. 642–646, 2021, ISSN: 10959203. DOI: 10.1126/science.abf7945.

[13] T. Charles, *Synchrotrons on the coronavirus frontline*, 2020. [Online]. Available: https://cerncourier.com/a/synchrotrons-on-the-coronavirus-frontline/.

[14] *Corona research at desy*. [Online]. Available: https://www.desy.de/news/corona_research/index_eng.html.

[15] R. Wideröe, "Über ein neues Prinzip zur Herstellung hoher Spannungen," *Archiv für Elektrotechnik*, vol. 21, no. 4, pp. 387–406, 1928, ISSN: 00039039. DOI: 10.1007/BF01656341.

[16] J. D. Cockcroft, E. T. S. Walton, and E. Rutherford, "Experiments with high velocity positive ions," *Proceedings of the Royal Society of London. Series A, Containing Papers of a Mathematical and Physical Character*, vol. 136, no. 830, pp. 619–630, 1932. DOI: 10.1098/rspa.1932.0107. [Online]. Available: https://royalsocietypublishing.org/doi/abs/10.1098/rspa.1932.0107.

[17] E. O. Lawrence and M. S. Livingston, "The production of high speed light ions without the use of high voltages," *Phys. Rev.*, vol. 40, pp. 19–35, 1 1932. DOI: 10.1103/PhysRev.40.19. [Online]. Available: https://link.aps.org/doi/10.1103/PhysRev.40.19.

[18] D. W. Kerst, "The acceleration of electrons by magnetic induction," *Phys. Rev.*, vol. 60, pp. 47–53, 1 1941. DOI: 10.1103/PhysRev.60.47. [Online]. Available: https://link.aps.org/doi/10.1103/PhysRev.60.47.

[19] E. M. McMillan, "The synchrotron—a proposed high energy particle accelerator," *Phys. Rev.*, vol. 68, pp. 143–144, 5-6 1945. DOI: 10.1103/PhysRev.68.143. [Online]. Available: https://link.aps.org/doi/10.1103/PhysRev.68.143.

[20] V. I. Veksler, "A new method of acceleration of relativistic particles," *J. Phys.*, vol. 9, pp. 153–158, 1945. [Online]. Available: https://cds.cern.ch/record/109364.

[21] E. D. Courant, M. S. Livingston, and H. S. Snyder, "The strong-focusing synchroton—a new high energy accelerator," *Phys. Rev.*, vol. 88, pp. 1190–1196, 5 1952. DOI: 10.1103/PhysRev.88.1190. [Online]. Available: https://link.aps.org/doi/10.1103/PhysRev.88.1190.

[22] P. Schmüser, "Superconductivity in high energy particle accelerators," *Progress in Particle and Nuclear Physics*, vol. 49, no. 1, pp. 155–244, 2002, ISSN: 01466410. DOI: 10.1016/S0146-6410(02)00145-X.

[23] J. Kirchgessner, H. Padamsee, H. L. Phillips, *et al.*, "Superconducting Cavities for Synchrotron Use," *IEEE Trans. Nucl. Sci.*, vol. 22, F. E. Mills, Ed., pp. 1141–1143, 1975. DOI: 10.1109/TNS.1975.4327830.

[24] M. Tigner, "Cesr - an electron positron colliding beam facility at cornell," *IEEE Transactions on Nuclear Science*, vol. 24, no. 3, pp. 1849–1853, 1977. DOI: 10.1109/TNS.1977.4329107.

[25] G. A. Voss and B. H. Wiik, "The electron-proton collider HERA," *Annual Review of Nuclear and Particle Science*, vol. 44, no. 1, pp. 413–452, 1994, ISSN: 01638998. DOI: 10.1146/annurev.ns.44.120194.002213.

[26] B. Aune *et al.*, "Superconducting tesla cavities," vol. 3, p. 092 001, 9 2000. DOI: 10.1103/PhysRevSTAB.3.092001. [Online]. Available: https://link.aps.org/doi/10.1103/PhysRevSTAB.3.092001.

[27] W Wuensch, "CLIC Accelerating Structure Development," 2008. [Online]. Available: https://cds.cern.ch/record/1124103.

[28] P. J. Bryant, "A Brief history and review of accelerators," in *CERN Accelerator School: Course on General Accelerator Physics*, 1992.

[29] M. Wenskat, "Automated Surface Classification of SRF Cavities for the Investigation of the Influence of Surface Properties onto the Operational Performance," Universität Hamburg, Diss., 2015, Dr. Universität Hamburg, Hamburg, 2015, p. 174. [Online]. Available: https://bib-pubdb1.desy.de/record/221603.

[30] B Faatz, E Plönjes, S Ackermann, *et al.*, "Simultaneous operation of two soft x-ray free-electron lasers driven by one linear accelerator," *New Journal of Physics*, vol. 18, no. 6, p. 062 002, 2016. DOI: 10.1088/1367-2630/18/6/062002. [Online]. Available: https://doi.org/10.1088/1367-2630/18/6/062002.

[31] F. Grüner *et al.*, "Design considerations for table-top, laser-based VUV and X-ray free electron lasers," *Applied Physics B: Lasers and Optics*, vol. 86, no. 3, pp. 431–435, 2007, ISSN: 09462171. DOI: 10.1007/s00340-006-2565-7. arXiv: 0612125 [physics].

[32] T Tajima and J. M. Dawson, "Laser electron accelerator," *Physical Review Letters*, vol. 43, no. 4, p. 267, 1979.

[33] J. Norem, A. Hassanein, Z. Insepov, and I. Konkashbaev, "Breakdown in rf cavities," in *Proceedings of the 2005 Particle Accelerator Conference*, 2005, pp. 1886–1888. DOI: 10.1109/PAC.2005.1590946.

[34] R Ruth, A. Chao, P Morton, and P Wilson, "A Plasma Wake Field Accelerator," *Particle Accelerators*, 1985, ISSN: 00219991. DOI: 10.1006/jcph.2000.6570.

[35] C. Joshi, "The development of laser- and beam-driven plasma accelerators as an experimental field," *Physics of Plasmas*, vol. 14, no. 5, 2007, ISSN: 1070664X. DOI: 10.1063/1.2721965.

[36] J. B. Rosenzweig, B. Breizman, T. Katsouleas, and J. J. Su, "Acceleration and focusing of electrons in two-dimensional nonlinear plasma wake fields," *Physical Review A*, 1991, ISSN: 10502947. DOI: 10.1103/PhysRevA.44.R6189.

[37] S. Schröder *et al.*, "High-resolution sampling of beam-driven plasma wakefields," *Nature Communications*, vol. 11, no. 1, 2020, ISSN: 20411723. DOI: 10.1038/s41467-020-19811-9. [Online]. Available: http://dx.doi.org/10.1038/s41467-020-19811-9.

[38] R. D'Arcy *et al.*, "FLASHForward: Plasma wakefield accelerator science for high-average-power applications," *Philosophical Transactions of the Royal Society A: Mathematical, Physical and Engineering Sciences*, 2019, ISSN: 1364503X. DOI: 10.1098/rsta.2018.0392.

[39] M. J. Hogan, T. O. Raubenheimer, A. Seryi, *et al.*, "Plasma wakefield acceleration experiments at FACET," *New Journal of Physics*, 2010, ISSN: 13672630. DOI: 10.1088/1367-2630/12/5/055030.

[40] V. Yakimenko, L. Alsberg, E. Bong, *et al.*, "FACET-II facility for advanced accelerator experimental tests," *Physical Review Accelerators and Beams*, vol. 22, no. 10, Oct. 2019, ISSN: 24699888. DOI: 10.1103/PhysRevAccelBeams.22.101301.

[41] S. Gessner, "Demonstration of the Hollow channel Plasma Wakefield Accelerator," Ph.D. dissertation, Stanford University, 2016.

[42] J. B. Rosenzweig, D. B. Cline, B. Cole, *et al.*, "Experimental observation of plasma wake-field acceleration," *Phys. Rev. Lett.*, vol. 61, pp. 98–101, 1 1988. DOI: 10.1103/PhysRevLett.61.98. [Online]. Available: https://link.aps.org/doi/10.1103/PhysRevLett.61.98.

[43] M. J. Hogan, C. D. Barnes, C. E. Clayton, *et al.*, "Multi-gev energy gain in a plasma-wakefield accelerator," *Phys. Rev. Lett.*, vol. 95, p. 054 802, 5 2005. DOI: 10.1103/PhysRevLett.95.054802. [Online]. Available: https://link.aps.org/doi/10.1103/PhysRevLett.95.054802.

[44] I. Blumenfeld, C. E. Clayton, F. J. Decker, *et al.*, "Energy doubling of 42 GeV electrons in a metre-scale plasma wakefield accelerator," *Nature*, 2007, ISSN: 14764687. DOI: 10.1038/nature05538.

[45] M. Litos, E. Adli, W. An, *et al.*, "High-efficiency acceleration of an electron beam in a plasma wakefield accelerator," *Nature*, 2014, ISSN: 14764687. DOI: 10.1038/nature13882.

[46] E. Gschwendtner *et al.*, "AWAKE, The Advanced Proton Driven Plasma Wakefield Acceleration Experiment at CERN," *Nuclear Instruments and Methods in Physics Research, Section A: Accelerators, Spectrometers, Detectors and Associated Equipment*, 2016, ISSN: 01689002. DOI: 10.1016/j.nima.2016.02.026.

[47] E. Adli *et al.*, "Acceleration of electrons in the plasma wakefield of a proton bunch," *Nature*, p. 1, 2018, ISSN: 0028-0836. DOI: 10.1038/s41586-018-0485-4. [Online]. Available: http://www.nature.com/articles/s41586-018-0485-4.

[48] A. Deng, O. S. Karger, T. Heinemann, *et al.*, "Generation and acceleration of electron bunches from a plasma photocathode," *Nature Physics*, 2019, ISSN: 17452481. DOI: 10.1038/s41567-019-0610-9.

[49] R. D'Arcy, S. Wesch, A. Aschikhin, *et al.*, "Tunable Plasma-Based Energy Dechirper," *Physical Review Letters*, 2019, ISSN: 10797114. DOI: 10.1103/PhysRevLett.122.034801.

[50] C. A. Lindstrøm *et al.*, "Energy-Spread Preservation and High Efficiency in a Plasma-Wakefield Accelerator," *Physical Review Letters*, vol. 126, no. 1, p. 14 801, 2021, ISSN: 10797114. DOI: 10.1103/PhysRevLett.126.014801. [Online]. Available: https://doi.org/10.1103/PhysRevLett.126.014801.

[51] A. M. de la Ossa, C Behrens, J Grebenyuk, *et al.*, "High-quality electron beams from field-induced ionization injection in the strong blow-out regime of beam-driven plasma accelerators," *Nuclear Instruments and Methods in Physics Research Section A: Accelerators, Spectrometers, Detectors and Associated Equipment*, vol. 740, pp. 231–235, 2014, ISSN: 0168-9002. DOI: http://dx.doi.org/10.1016/j.nima.2013.10.016.

[52] A. Martinez De La Ossa, Z. Hu, M. J. Streeter, *et al.*, "Optimizing density down-ramp injection for beam-driven plasma wakefield accelerators," *Physical Review Accelerators and Beams*, vol. 20, no. 9, 2017, ISSN: 24699888. DOI: 10.1103/PhysRevAccelBeams.20.091301.

[53] B Hidding, G Pretzler, J. B. Rosenzweig, *et al.*, "Ultracold Electron Bunch Generation via Plasma Photocathode Emission and Acceleration in a Beam-Driven Plasma Blowout," *Phys. Rev. Lett.*, vol. 108, no. 3, p. 35 001, Jan. 2012. DOI: 10.1103/PhysRevLett.108.035001. [Online]. Available: http://link.aps.org/doi/10.1103/PhysRevLett.108.035001.

[54] S. Bulanov, N. Naumova, F. Pegoraro, and J. Sakai, "Particle injection into the wave acceleration phase due to nonlinear wake wave breaking," *Physical Review E - Statistical Physics, Plasmas, Fluids, and Related Interdisciplinary Topics*, vol. 58, no. 5, R5257–R5260, 1998, ISSN: 1063651X. DOI: 10.1103/PhysRevE.58.R5257.

[55] G. Wittig, O. Karger, A. Knetsch, *et al.*, "Optical plasma torch electron bunch generation in plasma wakefield accelerators," *Physical Review Special Topics - Accelerators and Beams*, 2015, ISSN: 10984402. DOI: 10.1103/PhysRevSTAB.18.081304.

[56] A Aschikhin, C Behrens, S Bohlen, *et al.*, "The {FLASHForward} facility at {DESY}," *Nuclear Instruments and Methods in Physics Research Section A: Accelerators, Spectrometers, Detectors and Associated Equipment*, vol. 806, pp. 175–183, 2016, ISSN: 0168-9002. DOI: http://dx.doi.org/10.1016/j.nima.2015.10.005.

[57] J. Hecht, "Beam: The race to make the laser," *Opt. Photon. News*, vol. 16, no. 7, pp. 24–29, 2005. DOI: 10.1364/OPN.16.7.000024. [Online]. Available: http://www.osa-opn.org/abstract.cfm?URI=opn-16-7-24.

[58] A. Einstein, "Zur Quantentheorie der Strahlung. (German) [On the Quantum Theory of Radiation]," German, vol. 18, pp. 121–128, 1917, Republication of Einstein:1916:QSG.

[59] K. Renk, *Basics of Laser Physics: For Students of Science and Engineering*, ser. Graduate Texts in Physics. Springer Berlin Heidelberg, 2012, ISBN: 9783642235658. [Online]. Available: https://books.google.de/books?id=dpVDTLPySTQC.

[60] P. F. Moulton, "Spectroscopic and laser characteristics of ti:al2o3," *J. Opt. Soc. Am. B*, vol. 3, no. 1, pp. 125–133, 1986. DOI: 10.1364/JOSAB.3.000125. [Online]. Available: http://www.osapublishing.org/josab/abstract.cfm?URI=josab-3-1-125.

[61] R. Paschotta, *Field Guide to Lasers*. 2009. DOI: 10.1117/3.767474.

[62] W. E. Lamb, "Theory of an optical maser," *Phys. Rev.*, vol. 134, A1429–A1450, 6A 1964. DOI: 10.1103/PhysRev.134.A1429. [Online]. Available: https://link.aps.org/doi/10.1103/PhysRev.134.A1429.

[63] D. Strickland and G. Mourou, "Compression of amplified chirped optical pulses," *Optics Communications*, vol. 56, no. 3, pp. 219 –221, 1985, ISSN: 0030-4018. DOI: https://doi.org/10.1016/0030-4018(85)90120-8. [Online]. Available: http://www.sciencedirect.com/science/article/pii/0030401885901208.

[64] C. Iaconis and I. Walmsley, "Self-referencing spectral interferometry for measuring ultrashort optical pulses," *IEEE Journal of Quantum Electronics*, vol. 35, no. 4, pp. 501–509, 1999. DOI: 10.1109/3.753654.

[65] K. Poder, "Characterisation of self-guided laser wakefield accelerators to multi-gev energies," Ph.D. dissertation, 2016. [Online]. Available: https://books.google.de/books?id=rs0PvwEACAAJ.

[66] J. W. Goodman, *Introduction to Fourier optics*. Roberts and Company Publishers, 2005.

[67] J. D. Schmidt, *Numerical simulation of optical wave propagation with examples in MATLAB*. SPIE, 2010.

[68] M Born, E Wolf, A. B. Bhatia, *et al.*, *Principles of Optics: Electromagnetic Theory of Propagation, Interference and Diffraction of Light*. Cambridge University Press, 1999, ISBN: 9781139643405. [Online]. Available: https://books.google.de/books?id=kURdAAAAQBAJ.

[69] K. Poder, "Personal communication."

[70] F. F. Chen, *Introduction to Plasma Physics and Controlled Fusion*. Plenum Press New York and London, 1974, vol. 1.

[71] G Mainfray and G Manus, "Multiphoton ionization of atoms," *Reports on Progress in Physics*, vol. 54, no. 10, p. 1333, 1991. DOI: 10.1088/0034-4885/54/10/002. [Online]. Available: https://dx.doi.org/10.1088/0034-4885/54/10/002.

[72] L. Keldysh, "Ionization in the field of a strong electromagnetic wave," *Zh. Eksperim. i Teor. Fiz.*,

[73] H. R. Reiss, "Unsuitability of the keldysh parameter for laser fields," *Phys. Rev. A*, vol. 82, p. 023 418, 2 2010. DOI: 10.1103/PhysRevA.82.023418. [Online]. Available: https://link.aps.org/doi/10.1103/PhysRevA.82.023418.

[74] G. L. Yudin and M. Y. Ivanov, "Nonadiabatic tunnel ionization: Looking inside a laser cycle," *Physical Review A*, vol. 64, no. 1, p. 13 409, 2001.

[75] M. V. Ammosov, N. B. Delone, and V Krainov, "Tunnel ionization of complex atoms and of atomic ions in an alternating electric field," *Sov. Phys. JETP*, vol. 64, p. 1191, 1986.

[76] X. M. Tong and C. D. Lin, "Empirical formula for static field ionization rates of atoms and molecules by lasers in the barrier-suppression regime," *Journal of Physics B: Atomic, Molecular and Optical Physics*, vol. 38, no. 15, pp. 2593–2600, 2005, ISSN: 09534075. DOI: 10.1088/0953-4075/38/15/001.

[77] E. D. Courant and H. S. Snyder, "Theory of the alternating-gradient synchrotron," *Annals of Physics*, vol. 3, no. 1, pp. 1–48, 1958, ISSN: 0003-4916. DOI: http://dx.doi.org/10.1016/0003-4916(58)90012-5.

[78] P. Chen, J. M. Dawson, R. W. Huff, and T Katsouleas, "Acceleration of electrons by the interaction of a bunched electron beam with a plasma," *Physical review letters*, vol. 54, no. 7, p. 693, 1985.

[79] I. Blumenfeld, "Scaling of the longitudinal electric fields and transformer ratio in a non-linear Plasma Wakefield Accelerator," Ph.D. dissertation, Stanford University, Jan. 2009.

[80] W Lu, C Huang, M Zhou, *et al.*, "A nonlinear theory for multidimensional relativistic plasma wave wakefields," *Physics of Plasmas*, vol. 13, no. 5, pp. 056709+, 2006. DOI: 10.1063/1.2203364. [Online]. Available: http://dx.doi.org/10.1063/1.2203364.

[81] A. Martinez De La Ossa, J. Grebenyuk, T. Mehrling, L. Schaper, and J. Osterhoff, "High-quality electron beams from beam-driven plasma accelerators by wakefield-induced ionization injection," *Physical Review Letters*, 2013, ISSN: 00319007. DOI: 10.1103/PhysRevLett.111.245003.

[82] E. Oz, S. Deng, T. Katsouleas, *et al.*, "Ionization-induced electron trapping in ultrarelativistic plasma wakes," *Physical Review Letters*, 2007, ISSN: 00319007. DOI: 10.1103/PhysRevLett.98.084801.

[83] S Bulanov, N Naumova, F Pegoraro, and J Sakai, "Particle injection into the wave acceleration phase due to nonlinear wake wave breaking," *Phys. Rev. E*, vol. 58, no. 5, R5257–R5260, Nov. 1998. DOI: 10.1103/PhysRevE.58.R5257. [Online]. Available: http://link.aps.org/doi/10.1103/PhysRevE.58.R5257.

[84] H. Suk, N. Barov, J. B. Rosenzweig, and E Esarey, "Plasma electron trapping and acceleration in a plasma wake field using a density transition," *Physical review letters*, vol. 86, no. 6, p. 1011, 2001.

[85] J. L. Henares, P. Puyuelo-Valdes, F. Hannachi, *et al.*, "Development of gas jet targets for laser-plasma experiments at near-critical density," *Review of Scientific Instruments*, vol. 90, no. 6, p. 063 302, 2019. DOI: 10.1063/1.5093613. eprint: https://doi.org/10.1063/1.5093613. [Online]. Available: https://doi.org/10.1063/1.5093613.

[86] K. Schmid, A. Buck, C. M. S. Sears, *et al.*, "Density-transition based electron injector for laser driven wakefield accelerators," *Phys. Rev. ST Accel. Beams*, vol. 13, p. 091 301, 9 2010. DOI: 10.1103/PhysRevSTAB.13.091301. [Online]. Available: https://link.aps.org/doi/10.1103/PhysRevSTAB.13.091301.

[87] Z. Huang and K.-J. Kim, "Review of x-ray free-electron laser theory," *Phys. Rev. ST Accel. Beams*, vol. 10, p. 034 801, 3 2007. DOI: 10.1103/PhysRevSTAB.10.034801. [Online]. Available: https://link.aps.org/doi/10.1103/PhysRevSTAB.10.034801.

[88] D. A. Edwards, "TESLA Test Facility Linac: Design report. Version 1.0, March 1, 1995," 1995.

[89] J. Rossbach *et al.*, "A vuv free electron laser at the tesla test facility at desy," *Nuclear Instruments and Methods in Physics Research Section A: Accelerators, Spectrometers, Detectors and Associated Equipment*, vol. 375, no. 1, pp. 269 –273, 1996, Proceedings of the 17th International Free Electron Laser Conference, ISSN: 0168-9002. DOI: https://doi.org/10.1016/0168-9002(95)01332-6. [Online]. Available: http://www.sciencedirect.com/science/article/pii/0168900295013326.

[90] S. Schreiber and B. Faatz, "The free-electron laser flash," *High Power Laser Science and Engineering*, vol. 3, e20, 2015. DOI: 10.1017/hpl.2015.16.

[91] B. Faatz, M. Braune, O. Hensler, *et al.*, "The FLASH Facility: Advanced Options for FLASH2 and Future Perspectives," *Applied Sciences*, vol. 7, no. 11, p. 1114, 2017, ISSN: 2076-3417. DOI: 10.3390/app7111114. [Online]. Available: https://bib-pubdb1.desy.de/record/393961.

[92] S. Schröder, "External injection of electron beams into plasma-wakefield accelerators," Ph.D. dissertation, Hamburg U., Hamburg, 2021. DOI: 10.3204/PUBDB-2021-05396.

[93] S. Wesch, "Internal desy presentation," 2020.

[94] T. Auguste, P. Monot, L.-A. Lompré, G. Mainfray, and C. Manus, "Defocusing effects of a picosecond terawatt laser pulse in an underdense plasma," *Optics Communications*, vol. 89, no. 2, pp. 145 –148, 1992, ISSN: 0030-4018. DOI: https://doi.org/10.1016/0030-4018(92)90148-K. [Online]. Available: http://www.sciencedirect.com/science/article/pii/003040189290148K.

[95] A. Gómez-Vieyra, D. Malacara-Hernández, J. C. Hidalgo-González, and C. A. Vargas, "The wavefront aberrations in off-axis spherical mirror with object point or image point," in *Optical Systems Design 2012*, L. Mazuray, R. Wartmann, A. P. Wood, *et al.*, Eds., International Society for Optics and Photonics, vol. 8550, SPIE, 2012, pp. 498

–502. DOI: 10.1117/12.981208. [Online]. Available: https://doi.org/10.1117/12.981208.

[96] R. Adair, L. L. Chase, and S. A. Payne, "Nonlinear refractive index of optical crystals," *Phys. Rev. B*, vol. 39, no. 5, pp. 3337–3350, Feb. 1989. DOI: 10.1103/PhysRevB.39.3337. [Online]. Available: http://link.aps.org/doi/10.1103/PhysRevB.39.3337.

[97] J. Osterhoff, "Personal communication."

[98] P. O'Shea, M. Kimmel, X. Gu, and R. Trebino, "Highly simplified device for ultrashort-pulse measurement," *Opt. Lett.*, vol. 26, no. 12, pp. 932–934, 2001. DOI: 10.1364/OL.26.000932. [Online]. Available: http://ol.osa.org/abstract.cfm?URI=ol-26-12-932.

[99] B. R. Steffen, "Electro-Optic Methods for Longitudinal Bunch Diagnostics at FLASH," Ph.D. dissertation, University of Hamburg, 2007.

[100] Thorlabs.

[101] S. A. Akhmanov, A. P. Sukhorukov, and R. V. Khokhlov, "SELF-FOCUSING AND DIFFRACTION OF LIGHT IN a NONLINEAR MEDIUM," *Soviet Physics Uspekhi*, vol. 10, no. 5, pp. 609–636, 1968. DOI: 10.1070/pu1968v010n05abeh005849. [Online]. Available: https://doi.org/10.1070/pu1968v010n05abeh005849.

[102] R. Paschotta, *Article on self phase modulation in rp photonics encyclopedia*, https://www.rp-photonics.com/self_phase_modulation.html, Accessed: 2021-03-24.

[103] R. D'Arcy, A. Aschikhin, P. Gonzalez Caminal, V. Libov, and J. Osterhoff, "Longitudinal Phase Space Reconstruction at FLASHForward Using a Novel X-Band Transverse Decflection Cavity, PolariX," *International Particle Accelerator Conference 2018*, 2018. DOI: 10.18429/JACoW-IPAC2018-TUPML017.

[104] C. A. Lindstrøm *et al.*, "Matching small beta functions using centroid jitter and two beam position monitors," *Physical Review Accelerators and Beams*, vol. 23, no. 5, p. 52 802, 2020, ISSN: 2469-9888. DOI: 10.1103/PhysRevAccelBeams.23.052802. [Online]. Available: http://arxiv.org/abs/2002.06022.

[105] J. M. Garland, G. Tauscher, S. Bohlen, *et al.*, "Combining laser interferometry and plasma spectroscopy for spatially resolved high-sensitivity plasma density measurements in discharge capillaries," *Review of Scientific Instruments*, vol. 92, no. 1, p. 013 505, 2021. DOI: 10.1063/5.0021117. eprint: https://doi.org/10.1063/5.0021117. [Online]. Available: https://doi.org/10.1063/5.0021117.

[106] D. Ullmann *et al.*, *All-optical density downramp injection in electron-driven plasma wakefield accelerators*, 2020. arXiv: 2007.12634 [physics.plasm-ph].

[107] Z.-H. He, B Hou, V Lebailly, *et al.*, "Coherent control of plasma dynamics," *Nature Communications*, vol. 6, no. 1, p. 7156, 2015, ISSN: 2041-1723. DOI: 10.1038/ncomms8156. [Online]. Available: https://doi.org/10.1038/ncomms8156.

[108] M. Stephan and J. Docter, "Juqueen: Ibm blue gene/q® supercomputer system at the jülich supercomputing centre," *Journal of large-scale research facilities JLSRF*, vol. 1, Jun. 2015. DOI: 10.17815/jlsrf-1-18.

[109] W Lu, W An, M Zhou, *et al.*, "The optimum plasma density for plasma wakefield excitation in the blowout regime," *New Journal of Physics*, vol. 12, no. 8, p. 085 002, 2010. DOI: 10.1088/1367-2630/12/8/085002. [Online]. Available: https://doi.org/10.1088/1367-2630/12/8/085002.

[110] R. A. Fonseca, L. O. Silva, F. S. Tsung, *et al.*, "OSIRIS: A three-dimensional, fully relativistic particle in cell code for modeling plasma based accelerators," in *Lecture Notes in Computer Science (including subseries Lecture Notes in Artificial Intelligence and Lecture Notes in Bioinformatics)*, 2002, ISBN: 3540435948. DOI: 10.1007/3-540-47789-6{_}36.

[111] A. Knetsch, "Personal communication."

[112] E Esarey, C. B. Schroeder, and W. P. Leemans, "Physics of laser-driven plasma-based electron accelerators," *Rev. Mod. Phys.*, vol. 81, no. 3, pp. 1229–1285, Aug. 2009. DOI: 10.1103/RevModPhys.81.1229. [Online]. Available: http://link.aps.org/doi/10.1103/RevModPhys.81.1229.

[113] P. Scherkl *et al.*, *Plasma-photonic spatiotemporal synchronization of relativistic electron and laser beams*, 2019. arXiv: 1908.09263 [physics.plasm-ph].

[114] S. Schulz, I. Grguraš, C Behrens, *et al.*, "Femtosecond all-optical synchronization of an X-ray free-electron laser," *Nature communications*, vol. 6, 2015.

[115] C. Huang *et al.*, "Hosing instability in the blow-out regime for plasma-wakefield acceleration," *Phys. Rev. Lett.*, vol. 99, p. 255 001, 25 2007. DOI: 10.1103/PhysRevLett.99.255001. [Online]. Available: https://link.aps.org/doi/10.1103/PhysRevLett.99.255001.

[116] P. S. M. Claveria, E. Adli, L. D. Amorim, *et al.*, "Betatron radiation and emittance growth in plasma wakefield accelerators," *Philosophical Transactions of the Royal Society A: Mathematical, Physical and Engineering Sciences*, vol. 377, 2151 2019, ISSN: 1364503X. DOI: 10.1098/rsta.2018.0173.

[117] T. J. Mehrling, R. A. Fonseca, A. Martinez de la Ossa, and J. Vieira, "Mechanisms for the mitigation of the hose instability in plasma-wakefield accelerators," *Phys. Rev. Accel. Beams*, vol. 22, p. 031 302, 3 2019. DOI: 10.1103/PhysRevAccelBeams.22.031302. [Online]. Available: https://link.aps.org/doi/10.1103/PhysRevAccelBeams.22.031302.

[118] C. Lindstrøm *et al.*, "Energy-spread preservation and high efficiency in a plasma-wakefield accelerator," *Physical Review Letters*, 2020.

[119] G. Tauscher, "Ionisation of Hydrogen for Plasma Wakefield Accelerators," Masterarbeit, University of Hamburg, 2016, Masterarbeit, University of Hamburg, 2016, p. 117. [Online]. Available: https://bib-pubdb1.desy.de/record/316120.

[120] R. D'Arcy, V. Libov, and J. Osterhoff, "A transverse deflecting structure for the plasma wakefield accelerator experiment, flashforward," in *Proceedings of the 5th International Beam Instrumentation Conference, IBIC 2016*, 2016, ISBN: 9783954501779.

[121] S. Schreiber, B. Faatz, J. Feldhaus, K. Honkavaara, and R. Treusch, "FEL user facility FLASH," in *IPAC 2010 - 1st International Particle Accelerator Conference*, 2010, ISBN: 9789290833529.

[122] A. Meurer, C. P. Smith, M. Paprocki, *et al.*, "Sympy: Symbolic computing in python," *PeerJ Computer Science*, vol. 3, e103, Jan. 2017, ISSN: 2376-5992. DOI: 10.7717/peerj-cs.103. [Online]. Available: https://doi.org/10.7717/peerj-cs.103.

Acknowledgments

While a PhD thesis might only have one author, the completion of a PhD is not something that can be undertaken alone. Thus I would like to take the time to thank all the people who have helped me along the way, as such a feat would not be possible without the support of other people. First of all thanks to my supervisor Jens, who took a chance on a plucky summer student who was fascinated and desperate to learn more about plasma acceleration and offered me the opportunity to do just that. Thank you for opening that door and continuing to open more of them over the last few years. Next in-line is of course, everyone and anyone who worked to take FLASHForward from its initial inception as an idea through the development process and the construction phase(s) and then the commissioning and set-up of the experimental apparatus. To attempt to list everyone would ultimately leave many people out, so thank you!

Thanks to Lena and J-P who took me under their wing as a first year PhD student with almost no practical experience. Working in 28m with you was a lot of fun and, even though the work had almost nothing to do with my thesis topic, those initial months were of immense help to get my feet wet in the world of experimental plasma research. Special thanks also go to my X-1 co-conspirators Alex, Kris, Lucas, Jon, Lewis and Pardis, who helped bring this experiment to fruition and made long nights in the (FLASHForward) tunnel and the control room(s) bearable to the point of actual enjoyment. Here I will also thank Alex (again) who had the unenviable task of both steering the X-1 ship in the right direction alongside teaching his clueless crew-mates how to row the boat in the first place. His mentorship and continual encouragement was invaluable towards completing this thesis.

Although for some its existence is but a theoretical concept, learning to navigate the world outside of academia has played a significant role during my journey towards completing this PhD. To my now colleagues and especially my bosses at TrinamiX, Mohan and Felix, thank you for supporting me as I made my first foray into the big bad world beyond academia

and doing their best to quell my perfectionist traits in the world of engineering where ”good enough” is the name of the game.

I would also like to thank my revolving cast of flatmates and neighbours, with whom I shared many an evening or board game night and (almost) all of a pandemic. Marv, Sarah, Björn, Freya, Noel, Katja, Shrouk and everyone else who ever stepped across the threshold at Blücherstraße (Blüchi) thanks for all the good times! Despite my allergies, I also am incredibly grateful to have made the acquaintance of two adorable fuzzballs, Chi and Gizmo, who also happened to live at the same address and made it into a place to call home! After 5 years, my sense of smell is still somewhat lacking, but that's a small price to pay for having such fluffy company.

On a not quite so warm September day in 2018, I made the at the time seemingly reckless and irresponsible decision to buy a second hand road bike. I told myself at the time, that I would have to ride it in order to justify spending such a silly amount of money. I've now had that bike for over 4 years and have ridden it up literal mountains and over distances that would have made my jaw drop a few years ago. That is now one of the best decisions I ever made and I've discovered a passion that will, with any luck, be with me for decades to come. None of this would have been possible without the openness and acceptance of the cycling community who are, with very few exceptions, always happy to see new people and have helped me do more than I ever thought was possible.

Any PhD student who says they never thought about giving up is either a) lying or b) has a very poor memory. And so special thanks go out to all the people who have seen me through the hardest moments along this journey. Here I especially have to thank Pippa, who is never any further than a simple message away and always ready to hear me moan about anything and absolutely everything. Your friendship is a shining star in this word and over the last 10 years you've got me through countless difficult moments and been there to enjoy some of the best ones. Thanks also go out to my university friends Bekka and Char, without whom I'd never have got through undergrad or to the stage of completing a PhD thesis, I miss you both and hope we can see each other again soon.

At a fundamental level, exactly zero percent of this thesis would have been possible without the love and support of my parents, who always encouraged me to follow my own path in life. Their tales of childhoods spend in far-flung places meant that I knew from a young age the

options the world had to offer me and eventually gave me the courage to leave the nest of the UK for the no-so-far-flung and not-all-that-different wilds of Germany to take a chance on an interesting research project. While my Dad might not have got to see the completion of this work, I carry his love and encouragement with me to this day. Thank you for everything!